The Crystal Structures of Xenobiotic Reductase A and B from *Pseudomonas* putida II-B and *Pseudomonas* fluorescens I-C: Structural Insight into Regiospecific Reactions with Nitrocompounds.

A Thesis

Presented to

The Academic Faculty

by

Linda Manning

In Partial Fulfillment

of the Requirements for the Degree

Doctor of Philosophy in Chemistry

Georgia Institute of Technology

December 2005

The Crystal Structures of Xenobiotic Reductase A and B from *Pseudomonas* putida II-B and *Pseudomonas* fluorescens I-C: Structural Insight into Regiospecific Reactions with Nitrocompounds.

Approved by:

Dr. Allen M. Orville, Advisor
School of Chemistry and Biochemistry
Georgia Institute of Technology

Dr. Loren D. Williams
School of Chemistry and Biochemistry
Georgia Institute of Technology

Dr. Frank E. Löffler
School of Civil & Environmental Engineering
Georgia Institute of Technology

Dr. Nicholas V. Hud
School of Chemistry and Biochemistry
Georgia Institute of Technology

Dr. Dale E. Edmondson
Department of Biochemistry
Emory University

Date Approved: November 18th, 2005

‘’Love hides in molecular structures’’

Jim Morrison,

“*Love Hides”, The Doors, 1970*

Voor mijn ouders…..

ACKNOWLEDGMENTS

My gratitude and respect go to my advisor, Dr Allen Orville. He provided me with the opportunity to study protein crystallography and molecular structures of protein molecules. His extensive knowledge and guidance have been an inspiration to me during the past 5½ years. I am grateful for everything I have learned from him and for always asking me ‘Have you convinced yourself?’.

I would also like to thank the members of my PhD committee, Dr. Loren Williams, Dr. Nicholas Hud, Dr. Frank Löffler and Dr. Dale Edmondson for serving on my committee and providing valuable criticism, discussions and suggestions.

My sincere appreciation goes to Dr. George Lountos and Dr. Akansha Nagpal for the years we have spent together working in the Orville lab, for their knowledge and willingness to contribute, for the insightful conversations and for sharing all successes and failures over the last few years. In addition I would like to thank all members of the Williams group, past and present. Tatsuya Maehigashi (‘T’), Derrick Watkins, Dr. Seiji Komeda, Dr. Tinoush Moulai, Dr. Shelley Howerton, Dr. Kristen Woods and Dr. Ryan Burnett for all their advice and suggestions.

Special thanks goes to Dr. Brian Fox, Dr. Glenn Chambliss and Dr. Brian Blehert at the University of Wisconsin in Madison for providing purified XenA and XenB used for crystallization trials, for biochemical characterizations of these proteins and valuable critics and insights during the course of this research.

Furthermore, I would like to say thank you to Dr. Donald Doyle and Dr. Lauren Swimmer for helping me set up and perform docking calculations on XenA and XenB and for the kind use of their computer and software.

Special recognition goes to my parents who have always been my support system from the time I first expressed an interest in science to the completion of this thesis. Their frequent visits from the Netherlands and uncountable phone calls across the pond were more supportive than they probably realize. To my brother, Peter Manning, for always making me be his little sister, with all the benefits this comes with. To my better half, Peter Boezerooij, who has been there for me during times when frustrations and doubts were overwhelming. For never letting me give up and always keeping me grounded. Achter elke vrouw schuilt een veel grotere man.

A ‘thank you’ should also be extended to my two nieces, Lisette and Nienke, and my nephew, Joran, for the beautiful drawings you have made me and for always putting a smile on my face.

Last but certainly not least, I would like to thank all my friends in the United States, they have truly become my ‘american family’. Without them, the years I have spent here would have been much less enjoyable.

This research was supported by the American Chemical Society, Petroleum Research Fund (40310-G4), A.M.O. (PI) and an American Heart Association Grant in Aid (0555286B), A.M.O. (PI)

TABLE OF CONTENTS

LIST OF TABLES

LIST OF FIGURES AND SCHEMES

LIST OF SYMBOLS AND ABBREVIATIONS

α	Twinning fractions
Å	Angstrom (1 Å = 1.0×10^{-10} meters)
B	Temperature factor
Da	Dalton
DTT	dithiothreitol
f, f_0	atomic scattering contributions
F	Structure factor
h, k, l	Indices determining the crystal lattice
FMN	Flavin mononucleotide, oxidized or form
$FMNH_2$	Flavin mononucleotide, reduced form
$FMNH^-$	Flavin mononucleotide, anionic reduced form
I	Intensity
k	Scale factor for intensities
K	Kelvin
k_B	Boltzmann constant
K_m	Michaelis Menten constant
λ	Wavelength
MAD	Multiwavelength anomalous diffraction
MMC	Metropolis Monte Carlo
M_r	Moecular weight
NAD(P)H	Nicotinamide adenine dinucleotide (phosphate),
ncs	Non-crystallographic symmetry
PDB	Protein Data Bank
PEG	Polyethylene glycol

R_{sym}	$\frac{\sum_{hkl}\sum_{i}\left\|F_i(hkl)\right\| - \left\|\overline{F(hkl)}\right\|}{\sum_{hkl}\sum_{i}\left\|F_i(hkl)\right\|}$
R	$\frac{\sum_{hkl}\left\|\left\|F_{obs}\right\| - k\left\|F_{calc}\right\|\right\|}{\sum_{hkl}\left\|F_{obs}\right\|}$
R_{free}	$\frac{\sum_{hkl\subset T}\left\|\left\|F_{obs}\right\| - k\left\|F_{calc}\right\|\right\|}{\sum_{hkl\subset T}\left\|F_{obs}\right\|}$ T = test set
RMSD	Root mean square difference
SA	Simulated annealing
SeMet	Selenium methionine
θ	Scattering angle
T	Temperature
TNG	1,2,3-trinitroglycerin
DNG	Dinitroglycerin
MNG	Mononitroglycerin
TNT	2,4,6-trinitrotoluene
$\boldsymbol{u}$	Displacement parameter
$\boldsymbol{U}$	Anisotropic displacement parameter
V_M	Matthews coefficient
XenA	Xenobiotic reductase A
XenB	Xenobiotic reductase B

SUMMARY

Nitrochemicals are currently widely used as solvents, drugs, biocides, fuels and explosives and are consequently widely distributed in the environment. Explosive compounds such as 1,2,3-trinitroglycerin (TNG) and 2,4,6-trinitrotoluene (TNT) do not have any known naturally occurring counterparts and are present in the soil and groundwater of some EPA superfund sites. The reductive nitrite elimination from explosive compounds is catalyzed by two FMN-dependent, xenobiotic reductases (XenA or XenB). These genes for these regiospecific enzymes were cloned from *Pseudomonas putida* and *P. fluorescens* I-C respectively and isolated from the soil of a contaminated World War II munitions manufacturing plant. These enzymes enable the microbes to fulfill their nitrogen requirements from nitroglycerin by catalyzing the regiospecific, NADPH dependent, reductive denitration of nitroglycerin with differing selectivities toward nitro groups on nitroglycerin. The two enzymes also transform a number of additional nitrocompounds *in vitro,* e.g. TNT and metronidazole, a leading drug in the treatment of *Helicobacter pylori*, a causative agent of human ulcers.

Single crystals were obtained for XenA and XenB and complete X-ray diffraction datasets have been collected and analyzed to better understand these characteristics. The XenA crystals belong to space group $P2_12_12$ with unit cell dimensions a = 84 Å, b = 157 Å and c = 57 Å. The XenB crystals are in spacegroup $P4_12_12$ with a = b = 198 Å and c = 95 Å . Matthews coefficient analysis reveals two molecules in the asymmetric unit for XenA and four molecules in the asymmetric unit for XenB. Experimental phasing from MAD data analysis of Se-Met XenA reveal a local two-fold screw axis approximately

parallel to the c* axis that relates the two molecules in the asymmetric unit. The 1.6 Å resolution structure of XenA reveals a dimer of $(\beta/\alpha)_8$-TIM barrels, but the 2.3 Å resolution structure for XenB is a monomer. The $(\beta/\alpha)_8$-TIM barrel protein fold is the most common fold in the PDB. However, the XenA structure exhibits a unique, C-terminal domain-swapped topology. Thus a portion of each active site is comprised of residues from the neighboring monomer.

To probe the reaction cycle, crystal structures of ligand complexes and the reduced enzyme have been refined. For example, our structure of the XenA-metronidazole complex shows that ligands bind parallel to the FMN *si*-face. Our 1.5 Å resolution structure for reduced XenA reveals an FMN isoalloxazine ring with an angle of ~165° along the N5-N10 axis. We have also generated models of the reduced enzyme-nitroglycerin complexes by molecular dynamics. The results with both XenA and XenB reveal differences in enzyme-ligand hydrogen bonding. These differences correlate remarkably well with the regiospecific differences observed for nitrite elimination from nitroglycerin and reduction of TNT by the two enzymes.

1. A STRUCTURAL PERSPECTIVE ON NITRITE ELIMINATION OF ORGANIC NITROCHEMICALS BY FLAVOENZYMES

1.1 Abstract

Nitrochemicals from natural and anthropogenic sources are widely distributed throughout the environment. They are often mutagenic or toxic, in part because nitro group metabolism yields reactive nitrogen intermediates that modify DNA. Nevertheless, many microbes catabolize natural and xenobiotic nitrochemicals as sources of nitrogen. The crystal structures and functional analyses of the xenobiotic reductase from *Pseudomonas putida* (XenA) and the nitroalkane oxidase from *Fusarium oxysporum* (NAO) are discussed. XenA catalyzes the regiospecific, NADPH-dependent transformation of nitroglycerin to yield nitrite and 1,2-dinitroglycerin. It is a member of the $(\beta/\alpha)_8$-TIM barrel, FMN-dependent oxidoreductase family, but exhibits a unique, C-terminal domain-swapped topology. Thus a portion of each active site is comprised of residues from the neighboring monomer. Ligand complexes and redox perturbations are

Formatted from: Orville, A. M., Nagpal, A., **Manning, L.**, Blehert, D. S., Valley, M. P., Chambliss G. H., Fox B. G., and Fitzpatrick, P. F. "A Structural Perspective on Nitrite Elimination of Organic Nitrochemicals by Flavoenzymes" Proceedings of the 15th International Symposium on Flavins and Flavoproteins, April 17-22, 2005, Shonan Village Center, Japan

used to probe the reaction cycle of XenA. In contrast, NAO catalyzes the oxidation of naturally-occurring, neutral nitroalkanes to the corresponding aldehydes or ketones with production of H_2O_2 and nitrite. The structural analysis of active and inhibited NAO in the oxidized state are compared to NAO trapped during turnover as a covalent 5-(2-nitrobutyl)-1,5-dihydro-FAD adduct. The results highlight important mechanistic differences between NAO and the acyl-CoA dehydrogenases, which are structural but not functional homologs of NAO.

1.2 Introduction

Many organic nitrochemicals are widely used as drugs, herbicides, pesticides and explosives [1, 2]. They are also present in the exhaust of internal combustion engines and tobacco smoke. Consequently, they have been distributed throughout the environment from man-made sources in vast excess over naturally occurring examples. Some naturally occurring nitrochemicals include nitropropionic acid, chloramphenicol and azomycin (Figure 1.1). In addition, nitrated protein residues, such as 3-NO_2-Tyr, are now important post-translational markers for oxidative damage, septic shock, Alzheimer's disease as well as many cardiovascular, neurodegenerative and malignant conditions [3-8]. Explosive compounds, like nitroglycerin (TNG) and 2,4,6-trinitrotoluene (TNT), do not have any known naturally occurring counterparts; therefore, they are to be considered xenobiotics [2, 9, 10]. Nitroglycerin was first synthesized by Sobrero in 1846, whereas the more powerful explosives RDX (~1920) and CL-20 (>1975) are more recent. Nitroglycerin is also currently one of the 100 most frequently prescribed drugs;

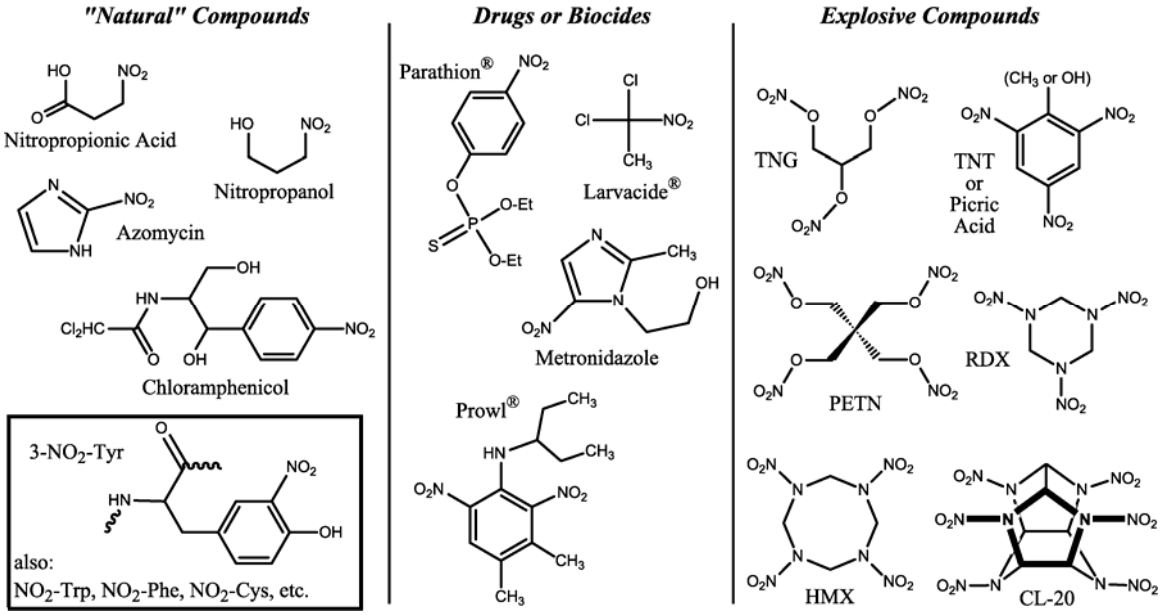

Figure 1.1: Chemical structures of some nitrochemicals dispersed throughout the environment.

principally for the treatment of angina pectoris [1]. Indeed, this was first reported in 1879 just 33 years after nitroglycerin was invented [11]. The biotransformation of nitroglycerin is a complex process, but in at least one pathway it is converted by vascular smooth muscle cells and yields 1,2-dinitroglycerol, nitrite, and eventually nitric oxide (•NO). Chen *et al*. demonstrated in 2002 that a novel activity of mammalian mitochondrial aldehyde dehydrogenase (mt-ALDH) catalyzes the regiospecific, reductive denitration of nitroglycerin to yield nitrite and 1,2-dinitroglycerin [12].

Many nitrochemicals are toxic at concentrations well below their solubility limit. For example, Prowl® and related nitroaromatic explosives and pesticides are proton-transporting ionophores, which uncouple oxidative phosphorylation. Metronidazole is now a leading drug in the treatment of *Helicobacter pylori*, a causative agent of human ulcers. The pathogen contains the *rdxA* gene, which encodes for an NADPH-dependent,

oxygen insensitive nitroreductase [13]. The enzyme reduces the nitro group of metronidazole to yield the cytotoxic derivatives that kill the pathogen [14-17]. Thus, the reductive biotransformation of nitro groups often yields reactive nitroso (R-NO) and hydroxylamino (R-NHOH) intermediates, which are capable of modifying DNA [18]. For example, ethylnitrosourea, a potential product of reduction of some nitramines, is a strong alkylating agent that causes genetic transversions. Nevertheless, studies of microbes isolated from environments containing natural or xenobiotic nitrochemicals have established that many are catabolized. In fact, nitroesters ($R\text{-}O\text{-}NO_2$), nitroaromatics ($Ar\text{-}NO_2$), nitroalkanes ($R\text{-}CH_2\text{-}NO_2$) and nitramines ($R_2\text{-}N\text{-}NO_2$) each serve as sources of nitrogen, carbon and/or energy to some microbes [2, 10, 19-21]. Reductive transformation of $R\text{-}O\text{-}NO_2$ typically yields an alcohol and eliminates nitrite. In contrast, reduction of $Ar\text{-}NO_2$ tends to yield nitroso and hydroxylamino derivatives, but does not liberate nitrite. Oxidation of $Ar\text{-}NO_2$ by some flavoenzymes eliminates nitrite commensurate with hydroxylation. Finally, oxidative nitrite elimination from nitroaliphatics occurs with incorporation of either solvent or molecular oxygen into the aldehyde or ketone products.

1.3. Nitrite Elimination by Xenobiotic Reductases

Prokaryotes continually evolve to exploit chemicals introduced into the environment by natural sources or by recent human activities [22, 23]. Indeed, they are responsible for most of the transformations and flux of the chemical cycles in the biosphere [23]. The xenobiotic reductase A from *Pseudomonas putida* II-B (XenA) or B

from *P. fluorescens I-C* (XenB) were purified from bacterial strains isolated from the same site at the contaminated, World War II era, Badger munitions manufacturing plant in Baraboo, WI [24, 25]. The plant produced propellants and nitroglycerin for small arms ammunition between 1942 and 1975. The bacterial strains were identified because they not only tolerate concentrations of nitroglycerin that are toxic to nearly all other microbes, but they can also obtain all their nitrogen for growth from the xenobiotic compound. The two homologs share 34% sequence identity and 51% sequence similarity. Both XenA and XenB catalyze NADPH-dependent reductive nitrite elimination from nitroglycerin. However, the main product of XenA is 1,2-dinitroglycerol, whereas that of XenB is 1,3-dinitroglycerol (Figure 1.2). The enzymes also exhibit differences in their NADPH-coupled reactions with 2,4,6-trinitrotoluene (TNT). XenB exhibits five times higher specific activity than XenA when TNT is the acceptor molecule in the oxidative half-reaction [26]. Approximately 50% of the reducing equivalents yield nitro group reduction and the other half yield aromatic ring reduction. Thus, TNT reduction by two and four electrons yields the hydride-Meisenheimer (H-TNT, λ_{max} = 477 nm) and tautomers of the dihydride-Meisenheimer (2H-TNT; λ_{max} = 449-492 nm) products, respectively [26]. The expression host, *E. coli* DH5α, transformed with the genes for either XenA or XenB can survive on nitroglycerin as the sole source of nitrogen, but only when expressing those genes. The expression host also becomes sensitive to metronidazole (Figure 1.1), a nitro-containing pro-drug commensurate with XenA or XenB gene expression. In contrast, the untransformed expression host can not utilize nitroglycerin as a source of nitrogen and it is not naturally sensitive to metronidazole since it lacks an endogenous nitroreductase activity [24].

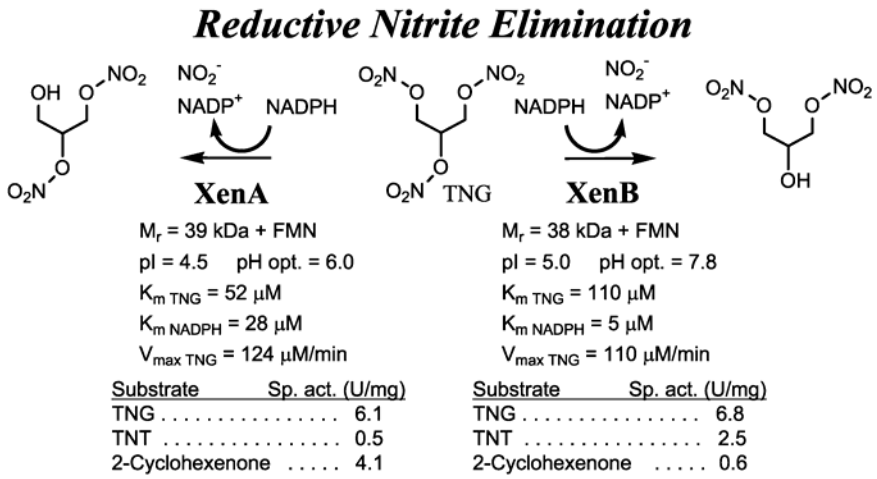

Figure 1.2: Some Characteristics of XenA and XenB [24-26].

To better understand the structural bases for these characteristics of XenA and XenB, we initiated their crystallographic analysis. The preliminary analysis of XenA and XenB has been reported [27, 28]. As illustrated in Figure 1.3, XenA has been refined to 1.65 Å resolution, although the refinement of XenB is still ongoing. The resulting structures for both enzymes are $(\beta/\alpha)_8$ TIM barrels with the FMN located at the N-terminal end of the barrel. This protein fold is the most common topology in the Protein Data Bank [29]. XenB is a monomeric structure, which is consistent with previous biochemical analysis [24, 25]. However, the XenA structure from *P. putida* II-B, exhibits a unique, C-terminal domain-swapped topology. Analysis of the refined XenA structure shows that approximately 3050 $Å^2$ of surface area is buried at the dimer interface located at the first α-helix of the eight-fold barrel topology. Moreover, one portion of the active site is comprised of the domain swapped, C-terminal region. Most importantly, tryptophan 357 (Trp357b in Figure 1.3), which is from the other subunit, packs against the dimethylbenzene portion of the FMN. This increases the solvent excluded surface area of the isoalloxazine ring by more than 20%. Several residues within the first α-helix

stabilize the dimer interaction and are not conserved in most of the XenA homologs. To our knowledge, this is the first example of such a domain-swapped topology in $(\beta/\alpha)_8$ barrels.

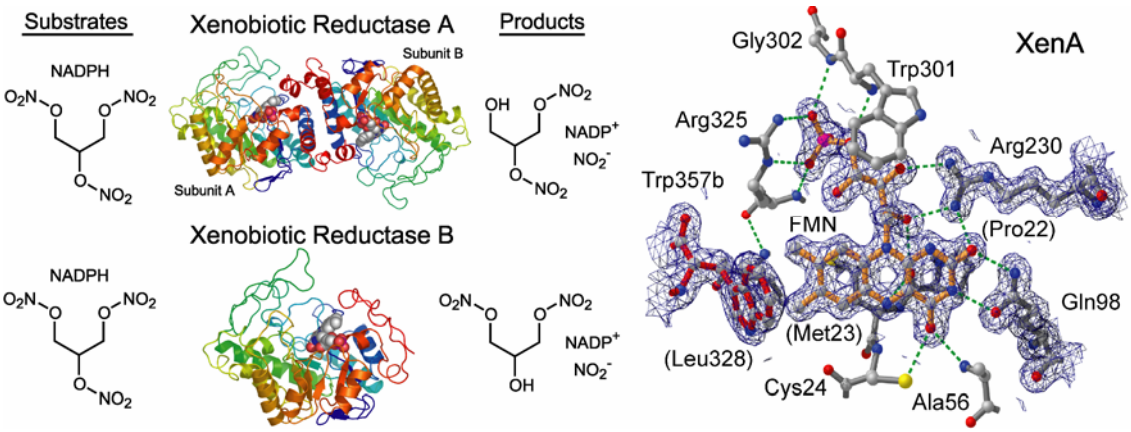

Figure 1.3: The crystal structure of XenA reveals a novel, domain-swapped dimer at the C-terminus (*top left*). In contrast, the structure of XenB is monomeric (*bottom left*). The $2mF_o - DF_c$ electron density (1.5σ) for XenA calculated to 1.6 Å resolution (*right*). Note that Trp357b is from the domain-swapped region.

We have recently completed the refinement for several crystal structures of XenA. This includes at least two, independent crystal structures each of oxidized XenA (1.65 Å resolution, R = 16.2 %, R_{free} = 18.7 %), oxidized XenA co-crystallized with 1.6 m*M* metronidazole (1.73 Å resolution, R = 17.5 %, R_{free} = 22.6 %) and aerobically reduced XenA (1.51 Å resolution, R = 17.6 %, R_{free} = 21.0 %). The structural analysis reveals that substrates bind parallel to the *si*-face of the FMN and the active-site residues that influence substrate binding. Most of the first-shell residues in XenA are shown or listed in Figures. 1.3 and 1.4 and includes Cys24, Tyr26, Ala56, Ile65, His177, His180, Tyr182, Trp301 and Trp357 from the other subunit. The structurally analogous residues in XenB and other homologs are shown in Figure 1.4. The crystal structures support proposed

reaction mechanisms involving hydride transfer to and from the N5 of FMN. Thus some of the potential contributions toward catalysis of these residues in XenA include: a) providing hydrogen bond donor and acceptor atoms that orient substrate molecules, b) establishing both hydrophobic and hydrophilic environments to enhance substrate and FMN binding and, c) serving as a proton donor for the oxidative half-reaction. Further studies are in progress to test some of these mechanistic hypotheses.

Protein	RMSΔ to XenA Å [a]	% Seq. id. (sim.)	Structurally Equivalent Active Site Residues in $(\beta/\alpha)_8$, FMN-Dependent Oxidoreductases [a]											
XenA [b]	---	100 (---)	C24	Y26	A56	I65	T66	Q98	**A100**	H177	H180	Y182	R325	W357 sub-B
YqjM [c]	---	37 (50)	C26	Y28	A60	I69	T70	Q102	A104	H164	H167	Y169	R308	G337
XenB [d]	1.33 (276 C_α)	33 (50)	T25	C27	A56	G65	Y66	Q98	**W100**	H173	N176	Y178	V309	F335, Y336
OPR-3 [e]	1.23 (269 C_α)	33 (47)	T33	C35	G64	G73	F74	Q106	W108	H186	H189	Y191	R344	F370, Y371
OPR-1 [f]	1.27 (268 C_α)	32 (48)	T37	Q39	A68	G77	Y78	Q110	W112	H187	H190	Y192	R331	F357, Y358
MorR [g]	1.23 (266 C_α)	30 (48)	T32	S34	A62	G71	Y72	Q104	W106	**H186**	**N189**	**C191**	R329	F355, Y356
OYE [h]	1.25 (258 C_α)	27 (45)	**T37**	M39	G72	G81	Y82	**Q114**	W116	**H191**	**N194**	**Y196**	R348	F374, Y375
PETNR [i]	1.20 (269 C_α)	27 (41)	T26	L28	A58	G67	Y68	Q100	**W102**	H181	H184	Y186	R324	F350, Y351
TMADH[j]	1.44 (242 C_α)	26 (40)	C30	G32	Y60	D69	T70	E103	W105	Y169	H172	Y174	R322	I352, W355
DCR [k]	1.24 (287 C_α)	24 (40)	H26	G28	G58	G67	M68	Q100	L102	M161	E164	Y166	R311	C341, L342, I345

[a]Based upon overlays of the given PDB entries and amino acid sequence alignments. Residues in shaded boxes have been mutated in various studies. [b]*P. putida* II-B xenobiotic reductase A, based on the crystal structure. [c]*B. subtilus* probable NADH-dependent flavin oxidoreductase YqjM. [d]*P. fluorescens* I-C xenobiotic reductase B based upon sequence analysis and molecular replacement structural model (unpublished data). [e]*Arabidopsis thaliana* 12-oxophytodienoate reductase isoform 3, PDB code 1q45. [f]*L. esculentum* 12-oxophytodienoate reductase isoform 1, PDB code 1icq. [g]*P. putida* morphinone reductase, PDB code 1gwj. [h]*S. Carlsbergensis* old yellow enzyme, PDB code 1oyb. [i]*E. cloacae* pentaerythritol tetranitrate reductase, PDB code 1h61. [j]TIM barrel domain (residues 1-380) of Methylotrophic bacterium trimethylamine dehydrogenase, PDB code 2tmd. [k]TIM barrel domain (residues 1-368) of E. *coli* 2,4-dienoyl-CoA-reductase, PDB code 1ps9.

Figure 1.4: Similarity between XenA, XenB and several homologs.

Our primary sequence analyses, catalytic studies, and structural results indicate that XenA and XenB are members of the FMN-dependent oxidoreductase subfamily of the $(\beta/\alpha)_8$ TIM-barrel superfamily [24, 29]. XenA shares 27% identity and 45% similarity with old yellow enzyme (OYE) [30, 31], the prototypical member of the subfamily, but whose physiological role has been difficult to unambiguously determine.

Several additional homologs include: a) many putative oxidoreductases from genomic sequencing of humans and other organisms, b) additional nitroester reductases isolated from other bacterial sources obtained at different contaminated munitions sites, c) morphinone reductase and d) N-ethylmaleimide reductase [32-39]. The other crystallographically characterized members of this subfamily (Figure 1.4) include pentaerythritol tetranitrate reductase [33, 40], morphinone reductase [32], the 12-oxophytodienoate reductase isoforms 1 [41] and 3 [42], 2,4-dienoyl-CoA reductase [39] and the isoforms of trimethylamine dehydrogenase [43, 44]. A significant body of work on these enzymes from several laboratories has established a hydride transfer mechanism for both the reductive and oxidative half reactions [19, 21, 45, 46].

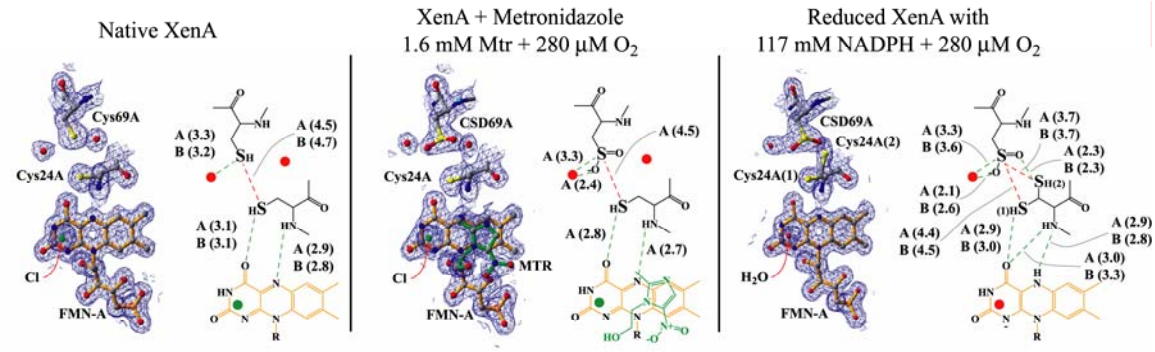

Figure 1.5: Reactivity of Cys24 and Cys69 in some crystal structures of XenA.

In addition to those resides shown in Figures 1.3 and 1.4, the active site of XenA also contains Cys69, a second-shell residue that is adjacent to Cys24. The structures of XenA exhibit interesting features in the high resolution $2mF_o - DF_c$ electron density maps (1σ contour), which are illustrated in Figure 1.5. For example, the native structure clearly shows that the two cysteine residues are present as thiols. In contrast, the co-

crystal complexes between XenA and metronidazole suggest that Cys69 is oxidized to at least the sulfenic acid (Cys-SOH), and possibly the sulfinic acid (Cys-SOOH) state. In addition, our 1.5 Å resolution structures for aerobic XenA crystals soaked in 117 m*M* NADPH and ~280 μ*M* O_2 from the atmosphere are consistent with Cys24 in two conformations, both of which are common rotomers. In one orientation, the maps suggest that a disulfide bond between Cys24 and Cys69 is present in a fraction of the enzymes within the crystal. Moreover, the maps also suggest that another fraction of enzymes contain Cys69 in an oxidized state. The NADPH soaked XenA crystals are bleached and the structures also show that the isoalloxazine ring system is bent by an angle of ~165° along the FMN N5-N10 axis. These conformations resemble gas-phase, theoretical and crystallographic studies of reduced flavins and flavin analogs. Those studies show that the two electron reduced isoalloxazine ring is "bent" by up to 30°, primarily along the N5-N10 axis. Therefore, we hypothesize that the alterations observed at Cys24 and Cys69 result from reduced FMN, produced by either x-ray irradiation, photoreduction or by excess NADPH, that reacts with O_2 to yield H_2O_2. Some of the H_2O_2 is proposed to react with the active site cysteine residues to yield the oxidation products illustrated in Figure 1.5. Further experiments are in progress to test this hypothesis. However, it is worth noting that the homolog, YqjM from *B. subtilis* is induced by H_2O_2 and is thought to alleviate oxidative stress in that organism [47]. It is also tempting to speculate about the potential for a NADPH peroxidase reaction similar to that of other flavin-dependent NAD(P)H oxidases and peroxidases [48-51]. For example, a sulfenic acid intermediate at either Cys24 or Cys69 residue could be reduced by formation of a disulfide bond between the two residues. The FMN *si*-face remains accessible and presumably NADPH could

reduce the FMN. In the next step, the reduced FMN could reduce the disulfide bond to yield resting enzyme containing oxidized FMN and Cys24 and Cys69 in their thiol states. Thus it is possible that XenA may exhibit an NADPH peroxidase activity, which could play a role in managing oxidative stress for the *P. putida* strain.

1.4. Nitrite Elimination by Nitroalkane Oxidase and 2-Nitropropane Dioxygenase

The nitroalkane oxidase (NAO) from *Fusarium oxysporum* and 2-nitropropane dioxygenase (2NPD) from either *Hansenula mrakii* or *Neurospora crassa* are induced by naturally occurring nitroaliphatic compounds [52-60]. This suggests that the oxidation of a nitroaliphatic species is the physiological role of the enzymes. Moreover, these enzymes enable these lower eukaryotes to obtain all their nitrogen from various nitrocompounds. This is remarkable because nitroalkanes are toxic to most organisms since they are very potent inhibitors of the citric acid cycle. Thus NAO and 2NPD are also hypothesized to protect the host from nitroalkanes produced as defensive toxins by many plants. The enzymes use either FMN or FAD to eliminate the nitrite from primary and secondary nitroalkanes such as nitroethane and 2-nitropropane and longer chain nitrocompounds (Figure 1.6). NAO and 2NPD do not share any significant amino acid sequence similarity, but they do turnover the same types of nitro substrates. However, they exhibit different preferences for either the neutral or anionic forms of the nitro substrates [57, 58, 61, 62]. NAO is active exclusively with neutral nitroalkanes. An active site base (Asp402) in NAO abstracts an α proton to generate the carbanion in the rate

limiting step of the reaction. Thus, NAO is unique in being the only flavoprotein to date for which a carbanion is definitively established as an intermediate in catalysis [63]. In contrast, the 2-nitropropane dioxygenases (2NPDs) are more active with the anionic form of similar substrates. Moreover, $^{18}O_2$ tracing experiments demonstrate that both O_2 atoms are incorporated into two acetone molecules [64]. Thus the chemistry catalyzed by 2NPDs is also unique; they are currently the only known examples of flavoprotein dioxygenases and incorporate one atom of O_2 into two different substrate molecules.

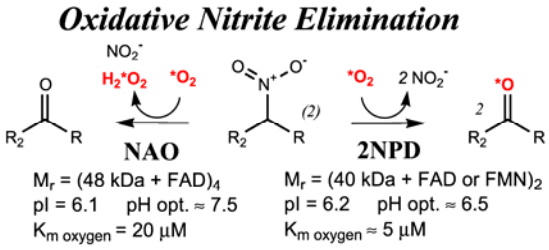

Enzyme	NAO			2NPD (*N. crassa*)		
Substrate	k_{cat} (s^{-1})	K_m (mM)	k_{cat}/K_m ($M^{-1}s^{-1}$)	k_{cat} (s^{-1})	K_m (mM)	k_{cat}/K_m ($M^{-1}s^{-1}$)
NO_2-ethane	3.35	2.9	4.84	14	29	480
NO_2-ethyl-anion	0	n.d.	0	51	3.1	16500
1-NO_2-propane	2.07	0.12	17300	1300	8.3	156
1-NO_2-propyl-anion	0	n.d.	0	n.d.	n.d.	n.d
2-NO_2-propane	1.33	3.5	380	4.0	16	250
2-NO_2-propyl-anion	0	n.d.	0	15	4.9	3100
1-NO_2-butane	1.65	0.009	183000	6.2	17.9	350
1-NO_2-butyl-anion	0	n.d.	0	55	10	5600
1-NO_2-pentane	2.05	0.015	137000	4.3	7.1	610
1-NO_2-pentyl-anion	0	n.d.	0	n.d.	n.d.	1200
1-NO_2-hexane	1.25	0.006	208000	1.5	1.4	1100
1-NO_2-hexyl-anion	0	n.d.	0	22	1.4	16000

Figure 1.6: Some characteristics of NAO and 2NPD [58, 61, 62].

1.5. The Crystal Structure of NAO-*E**, a Trapped Covalent Intermediate

We have crystallized NAO in several space groups and published the preliminary analysis of the active form of the enzyme [65]. Oxidized NAO readily crystallizes in a trigonal space group, diffracts to beyond 1.6 Å, but with a c unit cell edge of 485 Å. These characteristics push data collection facilities to the limit. Indeed, as of January 2005 only 158 x-ray structures (out of 29,040) deposited in the PDB contain a *c*-axis unit cell edge greater than 450 Å. Moreover, only 16 of these structures were to at least 2.5 Å resolution. However, we have observed diffraction data to at least 1.6 Å resolution at

several synchrotron x-ray sources. Therefore, to solve the structure of NAO, we used the covalent adduct form of NAO described by Gadda and Fitzpatrick [66] and termed NAO-*E**. In this state, the FAD is covalently modified as a 5-(2-nitrobutyl)-1,5-dihydro-FAD adduct (see Figure 1.8). The Se-Met enriched NAO-*E** was trapped during turnover of nitroethane in the presence of nitroethane anion, stabilized at low temperature and crystallized. This form of the enzyme crystallized in a smaller, orthorhombic unit cell compared to oxidized NAO. A three wavelength MAD dataset data from Se-Met enriched NAO-*E** was used to solve the structure via anomalous Se scattering. The initial analysis (*SOLVE*) to 3.0 Å resolution in space group $P2_12_12_1$ located 30 Se sites of an expected 52 (13 Se-Met residues per chain). Further analysis using all three wavelengths of data to 2.2 Å resolution with *SHARP* revealed the location of the remaining 22 Se sites. The 52 sites were refined and the electron density map was solvent flattened to

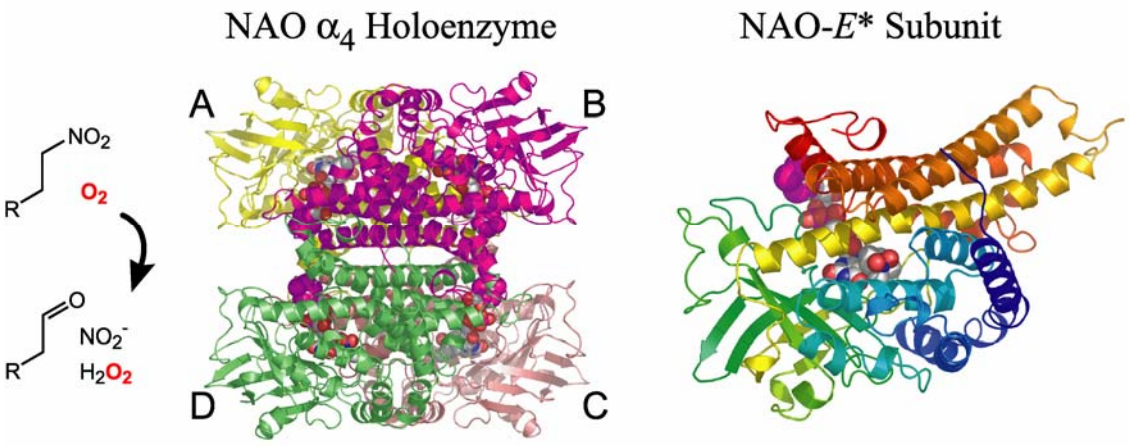

Figure 1.7: The NAO holoenzyme crystal structure and one subunit colored from N-terminal (blue) to C-terminal (red) with the N5-FAD adduct in space filled atoms.

produce superb 2.2 Å resolution $2mF_o - DF_c$ maps and an overall figure of merit of 0.95. The experimental maps were used to fit nearly the entire amino acid sequence and the

flavin moiety in each of four chains for the holoenzyme (Figure 1.7). The structure of NAO-*E** has been refined to 2.2 Å resolution and an *R* and R_{free} of 20.2% and 23.2%, respectively.

The crystal structure of NAO-*E** is a homotetramer with 222 symmetry relating the four subunits (Figure 1.7). Because two subunits interact much more extensively (e.g. chains A:B), the structure can be described as a dimer of dimers (A:B-C:D). Consistent with this, analytical ultracentrifugation results of NAO show a homotetramer-homodimer equilibrium with a K_a for tetramerization of 8×10^6 M^{-1} for identical subunits of molecular weight 47,955 [58]. Each subunit is comprised of two α-helical domains (approximately residues 1-125 and 260-438) and a β-sheet domain between them (approximately residues 125-260). The FAD is bound in an extended conformation within a crevice between the three domains of the subunit. Although the isoalloxazine ring is deeply buried, the adenine moiety projects out of the FAD binding crevice in each subunit. However, several additional interactions from the 2-fold related subunits pack around the FAD. Consequently very little surface area of the FAD in NAO-*E** is exposed to solvent.

1.6. Comparison of the Crystal Structures of Active NAO with NAO-*E**

We used the structure of NAO-*E** to solve the structure of oxidized NAO by molecular replacement in the trigonal space group ($P3_221$, $a = b = 103.4$ Å, $c = 485.7$ Å). The asymmetric unit contains 1½ holoenzymes (six subunits) and the structure has been refined to 2.07 Å resolution to an R and R_{free} of 18.8% and 22.7%, respectively. The NAO and NAO-*E** holoenzyme structures overlap with an average RMS difference of 0.33 Å for 1720 C_α atoms from throughout all four subunits. Interestingly, spermine $(HCl)_4$ is present in four of the six chains in the structure of oxidized NAO. It was added to the crystallization conditions and is a weak competitive inhibitor of NAO (K_i ~ 250 m*M*). Thus we have three examples of active site conformations, a) the resting state, b) an inhibited state, and c) the trapped intermediate. A comparison of theses active sites is shown in figure 1.8 with the refined $2mF_o - DF_c$ electron density maps contoured at 1 σ. The electron density for the N5-FAD adduct of NAO-*E** clearly shows it nestled between Asp402 and Phe401 and above the *re*-face of FAD cofactor. The isoalloxazine ring is bent by approximately 15° to greater than 25° in NAO and NAO-*E**, respectively.

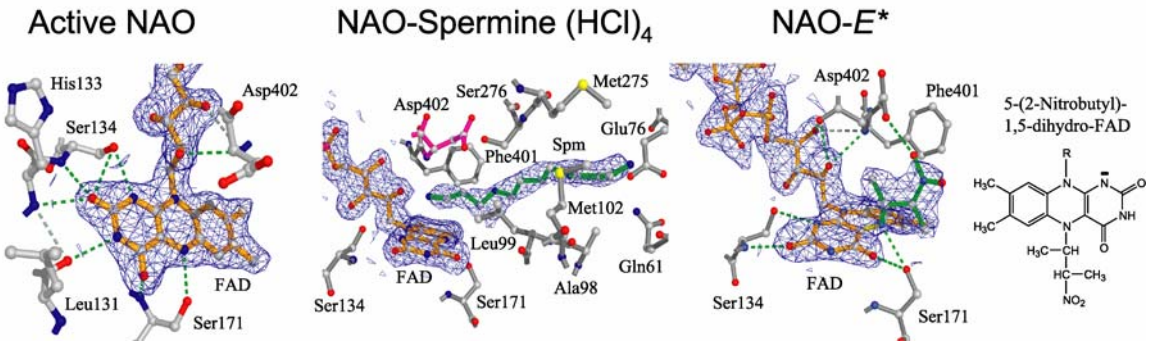

Figure 1.8: Examples of the electron density in the active sites in NAO and NAO-*E**

The distortion is more pronounced in the NAO-*E** adduct complex, which is consistent with a reduced, N5-adduct FAD species. There is also a shift in the hydrogen bonding pattern between the FAD and Ser171 in the two crystal structures. Similar distortions to the isoalloxazine ring systems have also been observed recently for N5 and C4a covalent adducts of monoamine and polyamine oxidases, which have structures that are otherwise completely unrelated to NAO [66-70]. Our NAO structures also correlate well with previous biochemical studies, which identified several active site residues that are important to function. This includes the location of Asp402 as the critical active site base [59, 71-73], which is poised directly above the *re*-face of the FAD. An active site tyrosine residue has been identified by tetranitromethane modification [74] and our structures shows that Tyr398 is located on one side of the active site cavity [75] . The Cys397 residue that was identified by chemical modification experiments is also in the active site cavity. The 2-nitrobutyl moiety in NAO-*E** and the spermine molecules in NAO each occupy a pocket above the *re*-face of the FAD, which is bordered by Ile92, Val95, Ala96, Leu99, Ser171, Phe273, Ser276, Val280, Met283, Phe401 and Asp402. Thus, the nitroalkane substrate binding cavity is formed almost exclusively with hydrophobic residues. This correlates with the preference for hydrophobic nitroalkane substrates (Figure 1.6) and the observation that each methylene group contributes ~2.6 kcal mol^{-1} binding energy [58, 61]. Moreover, the binding of spermine in this cavity also suggests that substrates likely access the FAD from a solvent channel that extends from the exterior of the protein to the N5 side of the flavin. This is in direct contrast to the substrate access channels observed in several crystal structures of the acyl-CoA dehydrogenases (reviewed in [76, 77]), which are homologous to NAO. Together, our

structural studies strongly support the carbanion-based reaction mechanism discussed by Fitzpatrick *et al.*, in an earlier chapter of this volume.

1.7. Structural, But Not Functional Homologs of NAO

The structural homologs of NAO include the acyl-CoA dehydrogenases (ACAD) ([76] and references therein), acyl-CoA oxidases (ACO) from rat liver peroxisomes or *Arabidopsis thaliana* [78, 79] and the Acyl-ACP dehydrogenases from polyketide biosynthetic pathways [80]. The structures for NAO clearly establish the homology with other members of the superfamily. Moreover, at least one crystal structure is available from each branch of the family of homologs. These provide structural-functional insights into NAO and the whole family and we have reported some of these observations in a recent review article [63]. Fore example, the medium chain acyl-CoA dehydrogenases (MCAD) is 25% identical (45% similarity) to NAO [59, 76, 81-83], but nevertheless, failed to yield a molecular replacement solution for the structure of NAO-*E**. Remarkably, the structure of the 661 residue, α_2 holoenzyme of ACO is also similar to NAO, despite only 9% sequence identity. Overlays of NAO with the different MCAD and ACO family members yield RMS differences that range from 1.6 to 2.1 Å at C_α positions of the homologous core. The homology between NAO and the ACADs extends throughout the entire subunit chain length. In contrast, the homologous region in the ACOs is between residues 21 to 440, which adopts a similar topological fold as the other members of the superfamily [78, 79].

Despite the structural similarity, the homologs have divergent amino acid sequences and also catalyze quite different reactions. Mechanistic studies of the ACAD enzymes were pioneered by Helmut Beinert almost five decades ago (reviewed in [76, 77]) and the research area is still very active. Indeed, the structural, mechanistic, mutagenic and spectroscopic analysis of the medium chain ACAD (MCAD) provides exquisitely detailed proposals for the structural contributions to catalysis. However, to our knowledge none of the ACAD or ACO enzymes will transform nitroalkanes, nor will NAO transform acyl-CoA substrates [59]. The structures of MCAD bound to transition-state analogs, substrates or products clearly shows that the acyl-CoA moiety binds adjacent to the ribitol portion of FAD (Figure 1.9) [76, 84]. In contrast, our structures of NAO show that spermine occupies a binding site that projects in the opposite direction. Moreover, several residues pack closer to the ribityl group of FAD in the NAO structures, suggesting that steric occlusion prevents acyl-CoA substrate access. Comparisons of these structures also highlight differences in the hydrogen bonding associated with the active site base, FAD and substrates, all of which are important determinants in guiding each particular reaction coordinate.

The active site bases in NAO and MCAD are Asp402 and Glu376, respectively (Figure 1.9). Sequestration of Glu376 in MCAD has been proposed to be at least partially responsible for matching the pK_a of the substrate and the active site base [76, 77]. Binding of substrate to MCAD results in lowering the pK_a of the α-proton by approximately 12 units (from ~20 to ~8-9). The same event also raises the pK_a of the active site Glu376 by approximately 6 units (from ~3.5 to ~9.2). Both events are thought to derive from exclusion of solvent by substrate binding and the formation of several

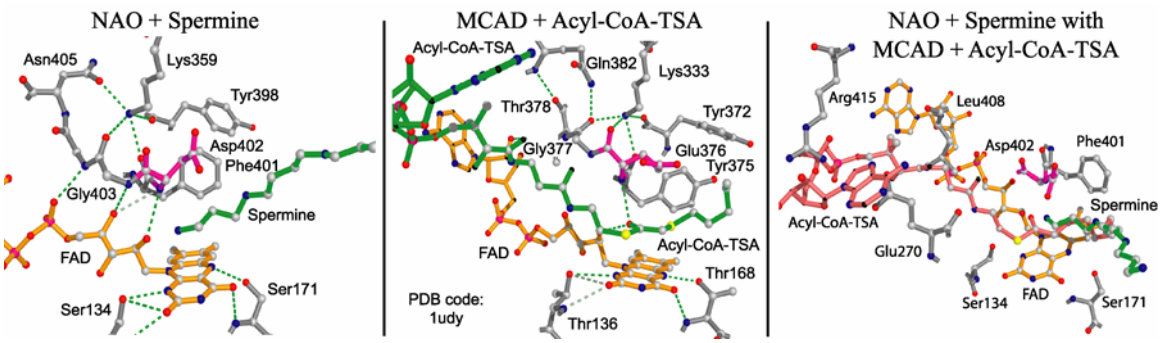

Figure 1.9: Active site comparison of NAO and MCAD + Acyl-CoA-TSA.

critical hydrogen bonds. The atoms analogous to the substrate α–β carbons of the transition state analog 3-thio-octanoyl-Co (Acyl-CoA-TSA) and the Glu376 side chain in MCAD complex are completely shielded from solvent, supporting the hypothesis [76, 77]. However, the pK_a for the nitroalkane α proton of NAO substrates is much closer to neutrality and thus solvent shielding of substrate and Asp402 may not be as critical in the NAO reaction. Consistent with these mechanistic considerations, we observe different hydrogen bonding patterns within the NAO active site compared to the MCAD homologs. For example, Asp402 hydrogen bonds with Arg409 in NAO, but Gln382 is the analogous residue in MCAD. However, Arg256 in MCAD occupies a structurally analogous location as NAO-Arg409, but it does not form hydrogen bonds with Glu376 in MCAD. In addition, Ser171 in NAO is also analogous to Thr168 in MCAD. This residue contributes a hydrogen bond to the N5-FAD which is thought to withdraw electron density and consequently make the flavin more electrophilic [76, 77]. A similar interaction is clearly possible in NAO. However, the consequences of all these interactions yield different outcomes; in MCAD a hydride is transferred, whereas in NAO an adduct forms. Further analysis will be required to understand the structural bases for

the different activities, as well as potential ancestral links to the MCAD, ACO and other superfamily members.

1.8. Conclusion

Structural studies of XenA and XenB support a hydride transfer reaction mechanism. However, XenA also exhibits evidence for redox activity between Cys24 and Cys69. Structural studies of NAO strongly support the carbanion-based reaction mechanism as discussed by Fitzpatrick et al. in an earlier chapter of this volume.

1.9. Acknowledgments

We thank Professors Dale E. Edmondson and Giovanni Gadda for many valuable discussions. This work was supported in part by the Georgia Tech Research Corporation and the Office of the Vice Provost for Research, Georgia Institute of Technology and an American Chemical Society Petroleum Research Fund type G grant (40310-G4) (A.M.O.), NSF grant MCB-9733734 (B.G.F), and the NIH grant GM58698 (P.F.F.).

1.10. References

1. Ahlner, J., R.G. Andersson, K. Torfgard, and K.L. Axelsson, *Organic nitrate esters: clinical use and mechanisms of actions.* Pharmacol. Rev., 1991. **43**(3): p. 351-423.

2. Spain, J.C., *Biodegradation of nitroaromatic compounds.* Annu. Rev. Microbiol., 1995. **49**: p. 523-555.

3. Aulak, K.S., T. Koeck, J.W. Crabb, and D.J. Stuehr, *Dynamics of protein nitration in cells and mitochondria.* Am. J. Physiol. Heart Circ. Physiol., 2004. **286**(1): p. H30-38.

4. Aulak, K.S., M. Miyagi, L. Yan, K.A. West, D. Massillon, J.W. Crabb, and D.J. Stuehr, *Proteomic method identifies proteins nitrated in vivo during inflammatory challenge.* Proc. Natl. Acad. Sci. U.S.A., 2001. **98**(21): p. 12056-12061.

5. Irie, Y., M. Saeki, Y. Kamisaki, E. Martin, and F. Murad, *Histone H1.2 is a substrate for denitrase, an activity that reduces nitrotyrosine immunoreactivity in proteins.* Proc. Natl. Acad. Sci. U.S.A., 2003. **100**(10): p. 5634-5639.

6. Kamisaki, Y., K. Wada, K. Bian, B. Balabanli, K. Davis, E. Martin, F. Behbod, Y.C. Lee, and F. Murad, *An activity in rat tissues that modifies nitrotyrosine-containing proteins.* Proc. Natl. Acad. Sci. U.S.A., 1998. **95**(20): p. 11584-11589.

7. Schopfer, F.J., P.R. Baker, and B.A. Freeman, *NO-dependent protein nitration: a cell signaling event or an oxidative inflammatory response?* Trends. Biochem. Sci., 2003. **28**(12): p. 646-654.

8. Turko, I.V., L. Li, K.S. Aulak, D.J. Stuehr, J.Y. Chang, and F. Murad, *Protein tyrosine nitration in the mitochondria from diabetic mouse heart. Implications to dysfunctional mitochondria in diabetes.* J. Biol. Chem., 2003. **278**(36): p. 33972-33977.

9. Rosser, S.J., A. Basran, E.R. Travis, C.E. French, and N.C. Bruce, *Microbial transformations of explosives.* Adv. Appl. Microbiol., 2001. **49**: p. 1-35.

10. Spain, J.C., J.B. Hughes, and H.J. Knackmuss, *Biodegradation of Nitroaromatic Compounds and Explosives*, ed. J.C. Spain, J.B. Hughes, and H.J. Knackmuss. 2000, Boca Raton: CRC Press LLC.

11. Murrell, W., *Nitroglycerin as a remedy for angina pectoris.* Lancet, 1879. **1**: p. 80-81.

12. Chen, Z., J. Zhang, and J.S. Stamler, *Identification of the enzymatic mechanism of nitroglycerin bioactivation.* Proc. Natl. Acad. Sci. U.S.A., 2002. **99**(12): p. 8306-8311.

13. Jeong, J.Y., A.K. Mukhopadhyay, D. Dailidiene, Y. Wang, B. Velapatino, R.H. Gilman, A.J. Parkinson, G.B. Nair, B.C. Wong, S.K. Lam, R. Mistry, I. Segal, Y. Yuan, H. Gao, T. Alarcon, M.L. Brea, Y. Ito, D. Kersulyte, H.K. Lee, Y. Gong, A. Goodwin, P.S. Hoffman, and D.E. Berg, *Sequential inactivation of rdxA (HP0954) and frxA (HP0642) nitroreductase genes causes moderate and high-level metronidazole resistance in Helicobacter pylori.* J. Bacteriol., 2000. **182**(18): p. 5082-5090.

14. Sisson, G., A. Goodwin, A. Raudonikiene, N.J. Hughes, A.K. Mukhopadhyay, D.E. Berg, and P.S. Hoffman, *Enzymes associated with reductive activation and action of nitazoxanide, nitrofurans, and metronidazole in Helicobacter pylori.* Antimicrob. Agents Chemother., 2002. **46**(7): p. 2116-2123.

15. Sisson, G., J.Y. Jeong, A. Goodwin, L. Bryden, N. Rossler, S. Lim-Morrison, A. Raudonikiene, D.E. Berg, and P.S. Hoffman, *Metronidazole activation is mutagenic and causes DNA fragmentation in Helicobacter pylori and in Escherichia coli containing a cloned H. pylori RdxA(+) (Nitroreductase) gene.* J. Bacteriol., 2000. **182**(18): p. 5091-5096.

16. Samuelson, J., *Why metronidazole is active against both bacteria and parasites.* Antimicrob. Agents Chemother., 1999. **43**(7): p. 1533-1541.

17. Trinh, S. and G. Reysset, *Mutagenic action of 5-nitroimidazoles: in vivo induction of GC-->CG transversion in two Bacteroides fragilis reporter genes.* Mutat. Res., 1998. **398**(1-2): p. 55-65.

18. Nathan, C. and M.U. Shiloh, *Reactive oxygen and nitrogen intermediates in the relationship between mammalian hosts and microbial pathogens.* Proc. Natl. Acad. Sci. U.S.A., 2000. **97**(16): p. 8841-8848.

19. Williams, R.E. and N.C. Bruce, *'New uses for an Old Enzyme'--the Old Yellow Enzyme family of flavoenzymes.* Microbiology, 2002. **148**(Pt 6): p. 1607-1614.

20. Williams, R.E., D.A. Rathbone, P.C. Moody, N.S. Scrutton, and N.C. Bruce, *Degradation of explosives by nitrate ester reductases.* Biochem. Soc. Symp., 2001. **68**: p. 143-153.

21. Williams, R.E., D.A. Rathbone, N.S. Scrutton, and N.C. Bruce, *Biotransformation of explosives by the old yellow enzyme family of flavoproteins.* Appl. Environ. Microbiol., 2004. **70**(6): p. 3566-3574.

22. Davies, J., *Inactivation of antibiotics and the dissemination of resistance genes.* Science, 1994. **264**(5157): p. 375-382.

23. Falkowski, P., R.J. Scholes, E. Boyle, J. Canadell, D. Canfield, J. Elser, N. Gruber, K. Hibbard, P. Hogberg, S. Linder, F.T. Mackenzie, B. Moore, 3rd, T. Pedersen, Y. Rosenthal, S. Seitzinger, V. Smetacek, and W. Steffen, *The global carbon cycle: a test of our knowledge of earth as a system.* Science, 2000. **290**(5490): p. 291-296.

24. Blehert, D.S., B.G. Fox, and G.H. Chambliss, *Cloning and sequence analysis of two Pseudomonas flavoprotein xenobiotic reductases.* J. Bacteriol., 1999. **181**(20): p. 6254-6263.

25. Blehert, D.S., K.L. Knoke, B.G. Fox, and G.H. Chambliss, *Regioselectivity of nitroglycerin denitration by flavoprotein nitroester reductases purified from two Pseudomonas species.* J. Bacteriol., 1997. **179**(22): p. 6912-6920.

26. Pak, J.W., K.L. Knoke, D.R. Noguera, B.G. Fox, and G.H. Chambliss, *Transformation of 2,4,6-trinitrotoluene by purified xenobiotic reductase B from Pseudomonas fluorescens I-C.* Appl. Environ. Microbiol., 2000. **66**(11): p. 4742-4750.

27. Orville, A.M., L. Manning, D.S. Blehert, B.G. Fox, and G.H. Chambliss, *Crystallization and preliminary analysis of xenobiotic reductase B from Pseudomonas fluorescens I-C.* Acta Cryst., 2004. **D60**(Pt 7): p. 1289-1291.

28. Orville, A.M., L. Manning, D.S. Blehert, J.M. Studts, B.G. Fox, and G.H. Chambliss, *Crystallization and preliminary analysis of xenobiotic reductase A and ligand complexes from Pseudomonas putida II-B.* Acta Cryst., 2004. **D60**(Pt 5): p. 957-961.

29. Nagano, N., C.A. Orengo, and J.M. Thornton, *One fold with many functions: the evolutionary relationships between TIM barrel families based on their sequences, structures and functions.* J. Mol. Biol., 2002. **321**(5): p. 741-765.

30. Fox, K.M. and P.A. Karplus, *Old yellow enzyme at 2 Å resolution: overall structure, ligand binding, and comparison with related flavoproteins.* Structure, 1994. **2**(11): p. 1089-1105.

31. Karplus, P.A., K.M. Fox, and V. Massey, *Flavoprotein structure and mechanism. 8. Structure-function relations for old yellow enzyme.* Faseb J., 1995. **9**(15): p. 1518-1526.

32. Barna, T., H.L. Messiha, C. Petosa, N.C. Bruce, N.S. Scrutton, and P.C. Moody, *Crystal structure of bacterial morphinone reductase and properties of the C191A mutant enzyme.* J. Biol. Chem., 2002. **277**(34): p. 30976-30983.

33. Barna, T.M., H. Khan, N.C. Bruce, I. Barsukov, N.S. Scrutton, and P.C. Moody, *Crystal structure of pentaerythritol tetranitrate reductase: "flipped" binding geometries for steroid substrates in different redox states of the enzyme.* J. Mol. Biol., 2001. **310**(2): p. 433-447.

34. French, C.E. and N.C. Bruce, *Bacterial morphinone reductase is related to Old Yellow Enzyme.* Biochem. J., 1995. **312**(Pt 3): p. 671-678.

35. Binks, P.R., C.E. French, S. Nicklin, and N.C. Bruce, *Degradation of pentaerythritol tetranitrate by Enterobacter cloacae PB2.* Appl. Environ. Microbiol., 1996. **62**(4): p. 1214-1219.

36. French, C.E., A.M. Hailes, D.A. Rathbone, and N.C. Bruce, *Morphinone reductase. Characterization, cloning, and application to biocatalytic hydromorphone production.* Ann. N. Y. Acad. Sci., 1996. **799**: p. 97-101.

37. French, C.E., S. Nicklin, and N.C. Bruce, *Sequence and properties of pentaerythritol tetranitrate reductase from Enterobacter cloacae PB2.* J. Bacteriol., 1996. **178**(22): p. 6623-6627.

38. Bruce, N.C., D.L. Willey, A.F. Coulson, and J. Jeffery, *Bacterial morphine dehydrogenase further defines a distinct superfamily of oxidoreductases with diverse functional activities.* Biochem. J., 1994. **299**(Pt 3): p. 805-811.

39. Hubbard, P.A., X. Liang, H. Schulz, and J.J. Kim, *The crystal structure and reaction mechanism of Escherichia coli 2,4-dienoyl-CoA reductase.* J. Biol. Chem., 2003. **278**(39): p. 37553-37560.

40. Khan, H., R.J. Harris, T. Barna, D.H. Craig, N.C. Bruce, A.W. Munro, P.C. Moody, and N.S. Scrutton, *Kinetic and structural basis of reactivity of pentaerythritol tetranitrate reductase with NADPH, 2-cyclohexenone, nitroesters, and nitroaromatic explosives.* J. Biol. Chem., 2002. **277**(24): p. 21906-21912.

41. Breithaupt, C., J. Strassner, U. Breitinger, R. Huber, P. Macheroux, A. Schaller, and T. Clausen, *X-ray structure of 12-oxophytodienoate reductase 1 provides structural insight into substrate binding and specificity within the family of OYE.* Structure, 2001. **9**(5): p. 419-429.

42. Malone, T.E., S.E. Madson, R.L. Wrobel, W.B. Jeon, N.S. Rosenberg, K.A. Johnson, C.A. Bingman, D.W. Smith, G.N. Phillips, Jr., J.L. Markley, and B.G. Fox, *X-ray structure of Arabidopsis At2g06050, 12-oxophytodienoate reductase isoform 3.* Proteins, 2005.

43. Barber, M.J., P.J. Neame, L.W. Lim, S. White, and F.S. Matthews, *Correlation of x-ray deduced and experimental amino acid sequences of trimethylamine dehydrogenase.* J. Biol. Chem., 1992. **267**(10): p. 6611-6619.

44. Trickey, P., J. Basran, L.Y. Lian, Z. Chen, J.D. Barton, M.J. Sutcliffe, N.S. Scrutton, and F.S. Mathews, *Structural and biochemical characterization of recombinant wild type and a C30A mutant of trimethylamine dehydrogenase from methylophilus methylotrophus (sp. W(3)A(1)).* Biochemistry, 2000. **39**(26): p. 7678-7688.

45. Fraaije, M.W. and A. Mattevi, *Flavoenzymes: diverse catalysts with recurrent features.* Trends. Biochem. Sci., 2000. **25**(3): p. 126-132.

46. Massey, V., *The chemical and biological versatility of riboflavin.* Biochem. Soc. Trans., 2000. **28**(4): p. 283-296.

47. Fitzpatrick, T.B., N. Amrhein, and P. Macheroux, *Characterization of YqjM, an Old Yellow Enzyme homolog from Bacillus subtilis involved in the oxidative stress response.* J. Biol. Chem., 2003. **278**(22): p. 19891-19897.

48. Lountos, G.T., B.R. Riebel, W.B. Wellborn, A.S. Bommarius, and A.M. Orville, *Crystallization and preliminary analysis of a water-forming NADH oxidase from Lactobacillus sanfranciscensis.* Acta Cryst., 2004. **D60**(Pt 11): p. 2044-2047.

49. Jacob, C., A.L. Holme, and F.H. Fry, *The sulfinic acid switch in proteins.* Org. Biomol. Chem., 2004. **2**(14): p. 1953-1956.

50. Claiborne, A., J.I. Yeh, T.C. Mallett, J. Luba, E.J. Crane, 3rd, V. Charrier, and D. Parsonage, *Protein-sulfenic acids: diverse roles for an unlikely player in enzyme catalysis and redox regulation.* Biochemistry, 1999. **38**(47): p. 15407-15416.

51. Poole, L.B., *Bacterial defenses against oxidants: mechanistic features of cysteine-based peroxidases and their flavoprotein reductases.* Arch. Biochem. Biophys., 2005. **433**(1): p. 240-54.

52. Kido, T., K. Hashizume, and K. Soda, *Purification and properties of nitroalkane oxidase from Fusarium oxysporum.* J. Bacteriol., 1978. **133**(1): p. 53-58.

53. Kido, T. and K. Soda, *Properties of 2-nitropropane dioxygenase of Hansenula mrakii. Formation and participation of superoxide.* J. Biol. Chem., 1978. **253**(1): p. 226-232.

54. Kido, T., K. Soda, T. Suzuki, and K. Asada, *A new oxygenase, 2-nitropropane dioxygenase of Hansenula mrakii. Enzymologic and spectrophotometric properties.* J. Biol. Chem., 1976. **251**(22): p. 6994-7000.

55. Kido, T., T. Yamamoto, and K. Soda, *Purification and properties of nitroalkane-oxidizing enzyme from Hansenula mrakii.* J. Bacteriol., 1976. **126**(3): p. 1261-1265.

56. Tchorzewski, M., T. Kurihara, N. Esaki, and K. Soda, *Unique primary structure of 2-nitropropane dioxygenase from Hansenula mrakii.* Eur. J. Biochem., 1994. **226**(3): p. 841-846.

57. Gadda, G., R.D. Edmondson, D.H. Russell, and P.F. Fitzpatrick, *Identification of the naturally occurring flavin of nitroalkane oxidase from Fusarium oxysporum as a 5-nitrobutyl-FAD and conversion of the enzyme to the active FAD-containing form.* J. Biol. Chem., 1997. **272**(9): p. 5563-5570.

58. Gadda, G. and P.F. Fitzpatrick, *Biochemical and physical characterization of the active FAD-containing form of nitroalkane oxidase from Fusarium oxysporum.* Biochemistry, 1998. **37**(17): p. 6154-6164.

59. Daubner, S.C., G. Gadda, M.P. Valley, and P.F. Fitzpatrick, *Cloning of nitroalkane oxidase from Fusarium oxysporum identifies a new member of the acyl-CoA dehydrogenase superfamily.* Proc. Natl. Acad. Sci. U.S.A., 2002. **99**(5): p. 2702-2707.

60. Zhang, J. and H. Tan, *Cloning, expression and characterization of a gene encoding nitroalkane- oxidizing enzyme from Streptomyces ansochromogenes.* Eur. J. Biochem., 2002. **269**(24): p. 6302-6307.

61. Gadda, G. and P.F. Fitzpatrick, *Substrate specificity of a nitroalkane oxidizing enzyme.* Arch. Biochem. Biophys., 1999. **363**(2): p. 309-313.

62. Francis, K., B. Russell, and G. Gadda, *Involvement of a Flavosemiquinone in the Enzymatic Oxidation of Nitroalkanes Catalyzed by 2-Nitropropane Dioxygenase.* J. Biol. Chem., 2005. **280**: p. 5195-5204.

63. Fitzpatrick, P.F., A.M. Orville, A. Nagpal, and M.P. Valley, *Nitroalkane oxidase, a carbanion-forming flavoprotein homologous to acyl-CoA dehydrogenase.* Arch. Biochem. Biophys., 2005. **433**(1): p. 157-165.

64. Gorlatova, N., M. Tchorzewski, T. Kurihara, K. Soda, and N. Esaki, *Purification, characterization, and mechanism of a flavin mononucleotide-dependent 2-nitropropane dioxygenase from Neurospora crassa.* Appl. Environ. Microbiol., 1998. **64**(3): p. 1029-1033.

65. Nagpal, A., M.P. Valley, P.F. Fitzpatrick, and A.M. Orville, *Crystallization and preliminary analysis of active nitroalkane oxidase in three crystal forms.* Acta Cryst., 2004. **D60**(Pt 8): p. 1456-1460.

66. Edmondson, D.E. and P. Newton-Vinson, *The covalent FAD of monoamine oxidase: structural and functional role and mechanism of the flavinylation reaction.* Antioxid. Redox. Signal., 2001. **3**(5): p. 789-806.

67. Binda, C., M. Li, F. Hubalek, N. Restelli, D.E. Edmondson, and A. Mattevi, *Insights into the mode of inhibition of human mitochondrial monoamine oxidase B from high-resolution crystal structures.* Proc. Natl. Acad. Sci. U.S.A., 2003. **100**(17): p. 9750-9755.

68. Binda, C., P. Newton-Vinson, F. Hubalek, D.E. Edmondson, and A. Mattevi, *Structure of human monoamine oxidase B, a drug target for the treatment of neurological disorders.* Nat. Struct. Biol., 2002. **9**(1): p. 22-26.

69. Binda, C., A. Mattevi, and D.E. Edmondson, *Structure-function relationships in flavoenzyme-dependent amine oxidations: a comparison of polyamine oxidase and monoamine oxidase.* J. Biol. Chem., 2002. **277**(27): p. 23973-23976.

70. Binda, C., R. Angelini, R. Federico, P. Ascenzi, and A. Mattevi, *Structural bases for inhibitor binding and catalysis in polyamine oxidase.* Biochemistry, 2001. **40**(9): p. 2766-2776.

71. Valley, M.P. and P.F. Fitzpatrick, *Inactivation of nitroalkane oxidase upon mutation of the active site base and rescue with a deprotonated substrate.* J. Am. Chem. Soc., 2003. **125**(29): p. 8738-8739.

72. Valley, M.P. and P.F. Fitzpatrick, *Reductive half-reaction of nitroalkane oxidase: effect of mutation of the active site aspartate to glutamate.* Biochemistry, 2003. **42**(19): p. 5850-5856.

73. Valley, M.P. and P.F. Fitzpatrick, *Comparison of enzymatic and non-enzymatic nitroethane anion formation: thermodynamics and contribution of tunneling.* J. Am. Chem. Soc., 2004. **126**(20): p. 6244-6245.

74. Gadda, G., A. Banerjee, and P.F. Fitzpatrick, *Identification of an essential tyrosine residue in nitroalkane oxidase by modification with tetranitromethane.* Biochemistry, 2000. **39**(5): p. 1162-1168.

75. Gadda, G., A. Banerjee, L.J. Dangott, and P.F. Fitzpatrick, *Identification of a cysteine residue in the active site of nitroalkane oxidase by modification with N-ethylmaleimide.* J. Biol. Chem., 2000. **275**(41): p. 31891-31895.

76. Kim, J.J. and R. Miura, *Acyl-CoA dehydrogenases and acyl-CoA oxidases. Structural basis for mechanistic similarities and differences.* Eur. J. Biochem., 2004. **271**(3): p. 483-493.

77. Ghisla, S. and C. Thorpe, *Acyl-CoA dehydrogenases. A mechanistic overview.* Eur. J. Biochem., 2004. **271**(3): p. 494-508.

78. Pedersen, L. and A. Henriksen, *Acyl-CoA Oxidase 1 from Arabidopsis thaliana. Structure of a Key Enzyme in Plant Lipid Metabolism.* J. Mol. Biol., 2005. **345**(3): p. 487–500.

79. Nakajima, Y., I. Miyahara, K. Hirotsu, Y. Nishina, K. Shiga, C. Setoyama, H. Tamaoki, and R. Miura, *Three-dimensional structure of the flavoenzyme acyl-CoA oxidase-II from rat liver, the peroxisomal counterpart of mitochondrial acyl-CoA dehydrogenase.* J. Biochem. (Tokyo), 2002. **131**(3): p. 365-374.

80. Watanabe, K., C. Khosla, R.M. Stroud, and S.C. Tsai, *Crystal structure of an Acyl-ACP dehydrogenase from the FK520 polyketide biosynthetic pathway: insights into extender unit biosynthesis.* J. Mol. Biol., 2003. **334**(3): p. 435-444.

81. Battaile, K.P., J. Molin-Case, R. Paschke, M. Wang, D. Bennett, J. Vockley, and J.J. Kim, *Crystal structure of rat short chain acyl-CoA dehydrogenase complexed with acetoacetyl-CoA: comparison with other acyl-CoA dehydrogenases.* J. Biol. Chem., 2002. **277**(14): p. 12200-12207.

82. Kim, J.J., M. Wang, and R. Paschke, *Crystal structures of medium-chain acyl-CoA dehydrogenase from pig liver mitochondria with and without substrate.* Proc. Natl. Acad. Sci. U.S.A., 1993. **90**(16): p. 7523-7527.

83. Lee, H.J., M. Wang, R. Paschke, A. Nandy, S. Ghisla, and J.J. Kim, *Crystal structures of the wild type and the Glu376Gly/Thr255Glu mutant of human medium-chain acyl-CoA dehydrogenase: influence of the location of the catalytic base on substrate specificity.* Biochemistry, 1996. **35**(38): p. 12412-12420.

84. Satoh, A., Y. Nakajima, I. Miyahara, K. Hirotsu, T. Tanaka, Y. Nishina, K. Shiga, H. Tamaoki, C. Setoyama, and R. Miura, *Structure of the transition state analog of medium-chain acyl-CoA dehydrogenase. Crystallographic and molecular orbital studies on the charge-transfer complex of medium-chain acyl-CoA dehydrogenase with 3-thiaoctanoyl-CoA.* J. Biochem. (Tokyo), 2003. **134**(2): p. 297-304.

2. CRYSTALLIZATION AND PRELIMINARY ANALYSIS OF XENOBIOTIC REDUCTASE A AND LIGAND COMPLEXES FROM PSEUDOMONAS PUTIDA II-B

2.1. Abstract

Diffraction-quality crystals have been obtained of the xenobiotic reductase A (XenA) from *Pseudomonas* II-B, which was originally cultured from the contaminated soil of aWorldWar II era munitions-manufacturing plant. Several complete X-ray diffraction data sets have been collected and analyzed. The native XenA data set includes reflections between 35 and 1.65 Å. Four-wavelength MAD data sets from selenomethionine-enriched XenA and from three different ligand complexes are also reported. The XenA crystals belong to space group $P2_12_12$, with unit-cell parameters a = 84 Å, b = 158 Å, c= 57 Å. Experimental phasing from analysis of the MAD data from selenomethionine-enriched XenA reveals the presence of two molecules in the asymmetric unit. They are related by a non-crystallographic 2_1 screw axis nearly parallel to the *c* axis, but offset by a quarter unit-cell translation. Thus, the local symmetry produces approximate systematic absences along the (00*l*) principal axis and complicates the space-group determination.

Reformatted form: Orville, A.M., **Manning, L.**, Blehert, D.S., Studts, J.M., Fox, B.G. & Chambliss, G.H. "Crystallization and preliminary analysis of xenobiotic reductase A and ligand complexes from *Pseudomonas putida* II-B" *Acta Cryst.* ***D*60**, 957-961 (2004)

2.2. Introduction

Microbes have evolved over billions of years to the point where they are now responsible for most of the transformations and flux of the chemical cycles in the biosphere [1-4]. The success and ubiquity of bacteria arises from their ability to metabolize diverse compounds in response to changes in environmental conditions [5]. Thus, virtually all compounds represent potential sources of carbon, nitrogen and/or energy upon transformation into central metabolic intermediates [6]. The ability to use novel chemicals, such as those recently produced by human activity, is thought to derive from unusual activities of pre-existing enzymes, from the altered reactivity of naturally arising enzyme isoforms or from horizontal gene transfer [7-13]. The structures, ancestry and regulation of enzymes that participate in newly emerged catabolic pathways have only infrequently been documented. However, these results are of interest because they impact diverse areas, including microbial drug resistance, bioremediation of priority pollutants and the evolution of enzyme structure and function [14-16].

Nitrochemicals are an important class of chemicals that are used as drugs, biocides, fuels, explosives and solvents. Since nitro group reduction can yield reactive nitrogen intermediates capable of modifying DNA, these compounds are considered to be mutagenic and toxic [17-21]. Consequently, the US Environmental Protection Agency regulates many sites contaminated with these molecules. The nitro-containing explosives nitroglycerin and 2,4,6-trinitrotoluene (TNT) were first synthesized in 1846 and 1863, respectively, and have since become widely distributed in the environment. Their relatively recent introduction and unique chemical properties relative to naturally occurring compounds make them attractive examples for the study of the processes

leading to xenobiotic transformation. Although no pathways for the complete aerobic catabolism of nitroglycerin or TNT are currently known, recent studies have established that these compounds are indeed transformed by a variety of enzymes to diverse products [22-24]. A documentation of the mechanisms by which these catabolic activities have emerged and continue to evolve would be of great interest. Toward this goal, the present work originated with the isolation of *Pseudomonas putida* II-B from nitrocontaminated soil at the Badger Army Ammunition Plant in Wisconsin, USA. This bacterium was enriched by the ability to obtain all nitrogen required for growth from nitroglycerin through the reductive elimination of nitrite. This reaction is catalyzed by a monomeric 39 kDa flavin mononucleotide-containing enzyme called xenobiotic reductase A (XenA). It catalyzes the successive NADPH-dependent nitrite elimination of nitroglycerin, with an apparent preference for the removal of a terminal nitro group. XenA will also reduce the nitro groups of TNT and metronidazole and the double bond of 2-cyclohexenone to yield cyclohexanone [25, 26].

Here, we report the initial crystallization and analysis of X-ray diffraction data from the native XenA, selenomethionine-enriched (SeMet) XenA and ligand complexes formed by co-crystallization with nitroglycerin, TNT and metronidazole. The data are of sufficient quality to permit structural characterization.

2.3. Material and Methods

2.3.1. Protein Expression and Purification

P. putida II-B was isolated as reported previously [27]. XenA was cloned and expressed in *Escherichia coli* and purified as reported previously [25, 27]. The enzymes isolated from *P. putida* II-B and *E. coli* were indistinguishable. SeMet XenA was produced in *E. coli* B834 (DE3) using fed-batch fermentation [28] and purified as previously reported except that 5 m*M* DTT was added to all buffers [25, 27]. Mass-spectral analysis of the purified SeMet XenA showed that the N-terminal methionine was completely removed and that the average SeMet enrichment was approximately 95%.

2.3.2. Crystallization and X-ray Data Collection

The initial crystallization conditions for XenA were determined from a sparse-matrix approach and optimized using additive screens from Hampton Research (Laguna Nigel, CA, USA). Hanging drops were equilibrated by vapor diffusion in Linbro 24-well plates at room temperature in Styrofoam insulated boxes. Typically, 2 ml protein solution (5-10 mg ml^{-1} in 20 m*M* HEPES buffer pH 7.0) was mixed with either 2 ml reservoir solution or 2 ml reservoir solution plus 1 ml ligand solution on a silanized cover slip. XenA crystals (Figure 2.1) were obtained from 0.1 *M* HEPES pH 7.4, 20 m*M* spermine tetrahydrochloride, 5% polyethylene glycol (PEG) 400 or PEG 8000 and 1.4-1.6 *M* ammonium sulfate. The ligand complexes of XenA were obtained by mixing SeMet XenA with nitroglycerin (1.1 m*M* final concentration from a 4.4 *M* stock solution dissolved in ethanol; VWR Inc.), TNT (2.2 m*M* final concentration from a 4.4 m*M* stock solution dissolved in acetonitrile; VWR Inc.) or metronidazole (1.6 m*M* final

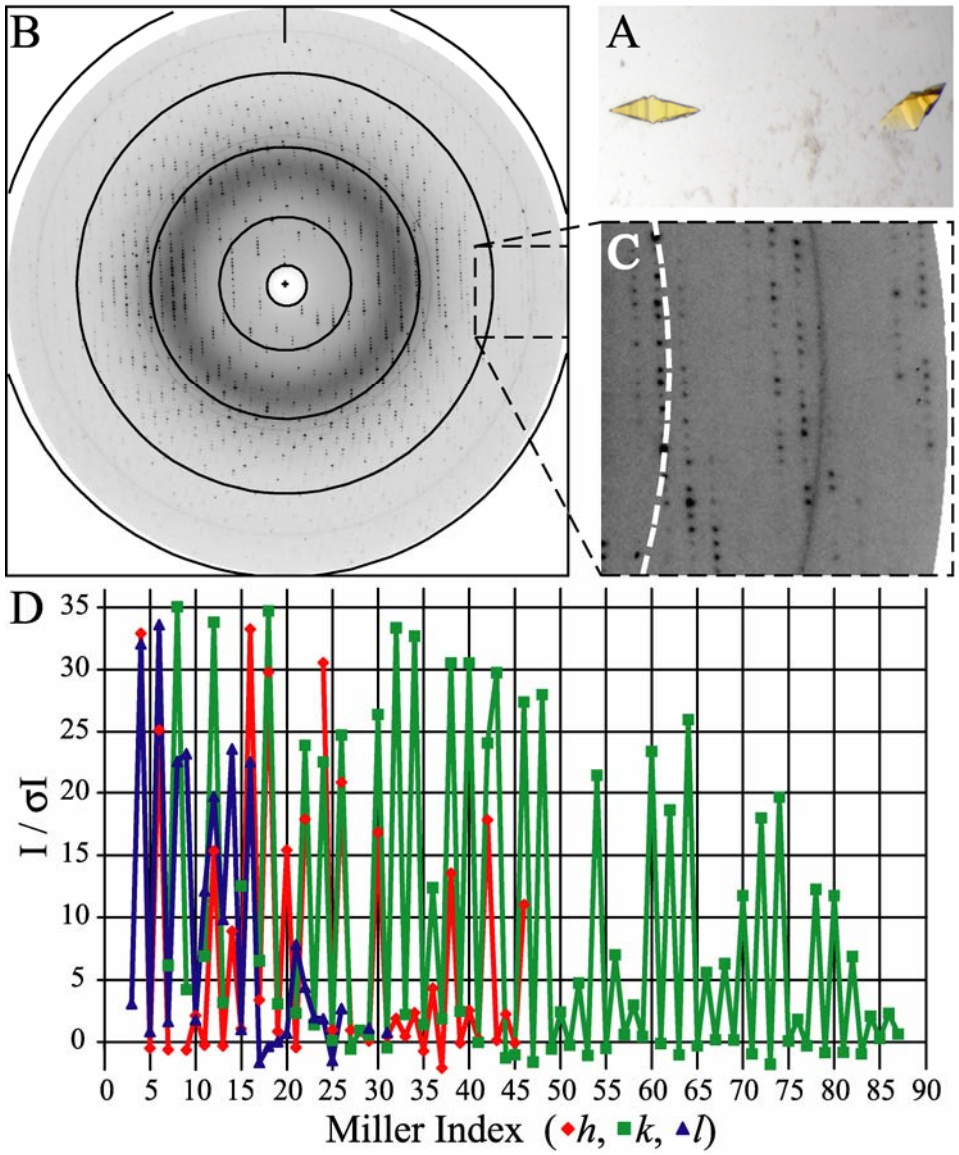

Figure 2.1: **A,** Crystals (~0.3 × 0.1 mm) of SeMet XenA grown in the presence of 1.1 m*M* nitroglycerin photographed without polarization. **B,** The X-ray diffraction pattern obtained at 100 K from SER-CAT beamline 22-ID, 1 s exposure, 1° rotation about the vertical axis (vertical line), 150 mm crystal-to-detector distance, MAR CCD 165 detector. The arcs indicate 2.0, 2.7, 4.0, 8.0 and 28 Å resolution, respectively. **C,** An expanded and contrast adjusted view of the high-resolution diffraction perpendicular to the rotation axis. The dashed arc indicates 2.7 Å resolution. **D,** Intensities of principal axis reflections for the XenA-metronidazole complex, which are typical of all data sets. Systematic absences along (*h*00) (red diamonds) and (0*k*0) (green squares) and pseudo-systematic absences along (00*l*) (blue triangles) are indicated by periodic $I/\sigma(I)$ values, which are the root-mean-square value of the intensity divided by the estimated standard deviation. The lines connecting the points are included solely to help illustrate the relationship between reflections along the each principal axis.

concentration from a 6.5 m*M* stock solution in water; ICN Biomedical Inc.) prior to setting up the hanging-drop experiment as above. Large single crystals required ~3 d of undisturbed equilibration time. The crystals were harvested from the drop with nylon loops and transferred into a cryoprotectant, which was Paratone-N most often (Hampton Research). The crystals were centered in the loop and the excess mother liquor was removed by briskly pulling the viscous cryoprotectant away from the crystal along the long axis of the crystal habit. The crystals were flash-frozen by either plunging the loop into liquid N_2 or by using the cold stream at the X-ray source. Several data sets were also collected at ~283 K with a crystal mounted and sealed in a 0.3 mm glass capillary.

The X-ray diffraction data sets (Table 2.1) were collected at either the Stanford Synchrotron Radiation Laboratory or the Advanced Photon Source beamline 22-ID operated by the South East Regional Collaborative Access Team. The 283 K native data set was collected in one continuous 80° wedge of φ rotation with a MAR 345 image-plate detector and a 225 mm crystal-to-film distance. All other data sets were collected using CCD-based area detectors. Fluorescence scans of the SeMet XenA crystals were analyzed to select the peak, inflection point and high- and low-energy remote wavelengths. The MAD data set for Se-Met XenA was collected using the inverse-beam method; two wedges of φ rotation that covered all the unique area of reciprocal space and two complementary wedges of φ + 180° were collected at each wavelength. The diffraction images were typically integrated with *MOSFLM* [29] and merged and scaled with *SCALA* from the *CCP4* suite of programs [30]. Occasionally, a data set was integrated with *HKL2000* and scaled with *SCALEPACK* [31]. The data sets were further analyzed and merged with *FHSCAL* or *SCALEIT*. The SeMet XenA MAD data were analyzed with

SOLVE [32] to locate the Se sites using the theoretical X-ray scattering factors calculated for each wavelength (*CROSSEC*). The resulting sites were refined with respect to all four wavelengths of the MAD data set with *SHARP* [33]. The solvent-flattened experimental maps revealed clearly interpretable density for two monomers in the asymmetric unit.

2.4. Results and Discussion

Crystals of XenA exhibited an elongated bipyramidal habit (Figure 2.1) that was easily oriented with the long axis parallel to the long axis of the cryoloop and consequently also with the goniometer φ-rotation axis. As indicated by the diffraction pattern for XenA aligned in this manner, the longest reciprocal cell axis was also aligned with the longest feature of the crystal habit. The X-ray diffraction data sets from XenA were all consistent with a primitive orthorhombic unit cell with approximate parameters 57 Å, 84 Å and 158 Å (Table 2.1). Cryopreservation and co-crystallization of three potential ligand complexes did not significantly perturb the unit-cell parameters (Table 2.1). Upon assumption of a reasonable molecular weight per unit volume (V_M = 2.47 $Å^3$ Da^{-1} and 50% solvent content; [34], two XenA molecules were assigned per asymmetric unit. Analysis of self-rotation functions with *GLRF* v.1.1 [35] did not reveal any significant peaks in the κ = 90 or 120° sections and revealed three peaks (~21σ) centered at (0, 0, 180°), (0, 90, 180°) and (90, 90, 180°) in the κ = 180° section. Therefore, the two molecules were likely to be related by at least twofold symmetry, which was also nearly parallel to a crystal unit-cell axis.

Table 2.1: Typical data-collection statistics for XenA. Values for the highest resolution shell of data are given in parentheses.

		SeMet XenA						
	XenA	Inflection	Peak	Low-energy remote	High-energy remote	SeMet XenA, peak	SeMet, remote	XenA
Ligand	---	---	---	---	---	1 mM nitroglycerin	1 mM TNT	1.6 mM metronidazole
X-ray source	SSRL	SSRL	SSRL	SSRL	SSRL	SER-CAT	SER-CAT	SER-CAT
Beamline	9-1	1-5	1-5	1-5	1-5	22-ID	22-ID	22-ID
Wavelength (Å)	0.98	0.979764	0.979609	1.06883	0.925256	0.979324	1.0332	1.0
Detector	MAR 345	Quantum 4R	Quantum 4R	Quantum 4R	Quantum 4R	MAR-CCD 165	MAR-CCD 165	MAR-CCD 165
Temperature (K)	283	100	100	100	100	100	100	100
Resolution range (Å)	35.6-1.65	33.0-2.5	35.1-2.5	37.0-2.5	31.1-3.0	28.2-2.0	32.8-2.3	27.1-1.8
Mosaic spread (°)	~0.2	~0.6	~0.6	~0.6	~0.6	~0.9	~1	~0.9
Unit-cell parameters (Å)								
a	84.7	83.9	83.9	83.9	83.9	84.1	83.8	84.3
b	157.9	157.5	157.5	157.5	157.5	157.8	158.1	158.2
c	58.7	57.0	57.0	57.0	57.0	57.2	57.0	57.3
Total reflections	312545	171463	208342	194373	89489	318610	221776	347467
Unique reflections	94132	24191	24297	23455	13929	43335	32984	70825
Multiplicity	3.3 (3.3)	7.1 (7.0)	8.6 (8.5)	8.3 (6.7)	6.4 (6.4)	7.2 (4.9)	6.6 (5.6)	4.9 (5.4)
Completeness (%)	98.9 (98.9)	91.1 (91.1)	91.5 (91.5)	88.4 (88.4)	89.8 (89.8)	87.2 (70.0)	97.8 (95.9)	99.6 (99.2)
Anomalous completeness(%)	---	89.9 (90.0)	90.5 (91.2)	86.8 (64.0)	81.4 (84.5)	86.2 (56.9)	---	---
R_{sym}†	0.051 (0.39)	0.128 (0.497)	0.121 (0.442)	0.105 (0.369)	0.173 (0.478)	0.027 (0.138)	0.097 (0.325)	0.052 (0.316)
$I/\sigma(I)$ ‡	17.5 (4.5)	5.4 (1.5)	5.7 (1.7)	6.5 (2.0)	4.1 (1.6)	21.8 (4.1)	6.6 (2.3)	11.1 (2.5)

† $R_{sym}(I)$ gives the average agreement between the independently measured intensities such as $\sum_h\sum_i|I_i - I|/\sum_h\sum_i I_i$, where I is the mean intensity of the i observations of reflection h. ‡ $I/\sigma(I)$ is the root-mean-square value of the intensity measurements divided by their estimated standard deviation.

Primitive orthorhombic space groups are differentiated by the presence of crystallographic twofold screw axes. If present, 2_1 symmetry requires that odd reflections are systematically absent along the principal axis. Consequently, the observed $I/\sigma(I)$ of the principal axis reflections (when scaled in space group $P222$) strongly suggested that XenA crystallized in space group $P2_12_12_1$ (Figure 2.1D). Indeed, the average $I/\sigma(I)$ for reflections along the three principal axes for the XenA-metronidazole complex are (even, 0, 0) = 14.55, (odd, 0, 0) = 0.14, (0, even, 0) = 17.35, (0, odd, 0) = 1.79, (0, 0, even) = 13.77 and (0, 0, odd) = 4.30. However, a few reflections along each principal axis in each data set violated the systematic absence condition; for example, in the XenA-metronidazole complex the reflection (17, 0, 0) has $I/\sigma(I)$ = 3.4, (0, 15, 0) = 15.4, (0, 43, 0) = 29.7, (0, 0, 9) = 23.2, (0, 0, 11) = 12.1 and (0, 0, 13) = 9.8. Therefore, an unambiguous determination of the space group was not possible using only the observed reflections along the three principal axes.

Furthermore, analysis of the SeMet XenA MAD data with *SOLVE* v.1.16 did not yield reasonable solutions in space group $P2_12_12_1$. In the best case, only three Se sites (of an expected ten sites) were located with a figure of merit of 0.32, a Z score of 38.2 and an average peak height/σ of 11.6. Consequently, the data were systematically re-indexed into the other orthorhombic space groups with permutations of the unit-cell parameters. Reproducible results with *SOLVE* were only obtained in space group $P2_12_12$, with a = 84 Å, b = 158 Å, c = 57 Å. For example, using a subset of the MAD data comprised of the inflection, peak and low-energy remote wavelengths and reflections between 3.0 and 35 Å resolution, nine Se sites were located with a maximum and minimum peak height/σ of 20.3 and 11.1, respectively, and an average of 14.9. The figure of merit for this solution

was 0.39 and the Z score was 27.8. The nine original Se sites refined to convergence with the four-wavelength data set in *SHARP*. A greater than +5σ difference peak clearly indicated the tenth Se site, which superimposed with the tenth Se site determined by analysis with *SOLVE*. The phasing statistics included a phasing power of 2.78 for centric reflections between 2.5 and 30 Å resolution using the peak wavelength (0.979609 Å). The overall figure of merit was 0.471 for 2437 centric reflections and 0.493 for 22 091 acentric reflections, which improved to 0.808 (22,966 reflections) after solvent flattening. The resulting electron-density maps were clearly interpretable and of sufficient quality for complete model building.

Table 2.2: Relationship between the five Selenium sites in each XenA molecule in the asymmetric unit.

Se Site	Observed Se coordinates (molecule *A*) †	Observed Se coordinates (molecule *B*) †	Molecule *A* sites after 2_1 transformation‡ ($A2_1$)	*B*-$A2_1$§ (Å)	*B*-$A2_1$§ (% of unit cell)
1	x = 35.38	x = 8.43	x = 6.59	Δx = 1.84	$\lvert\Delta x\rvert$ = 2.19a
	y = 58.27	y = 19.86	y = 20.47	Δy = -0.61	$\lvert\Delta y\rvert$ = 0.39b
	z = 12.07	z = 40.12	z = 40.56	Δz = -0.44	$\lvert\Delta z\rvert$ = 0.78c
2	x = 31.73	x = 11.82	x = 10.23	Δx = 1.59	$\lvert\Delta x\rvert$ = 1.90a
	y = 60.67	y = 17.26	y = 18.07	Δy = -0.81	$\lvert\Delta y\rvert$ = 0.51b
	z = 7.74	z = 35.54	z = 36.23	Δz = -0.69	$\lvert\Delta z\rvert$ = 1.20c
3	x = 18.23	x = 24.44	x = 23.73	Δx = 0.71	$\lvert\Delta x\rvert$ = 0.85a
	y = 69.25	y = 7.41	y = 9.49	Δy = -2.08	$\lvert\Delta y\rvert$ = 1.32b
	z = 5.71	z = 33.66	z = 34.20	Δz = -0.54	$\lvert\Delta z\rvert$ = 0.95c
4	x = 40.12	x = 4.18	x = 1.84	Δx = 2.34	$\lvert\Delta x\rvert$ = 2.79a
	y = 51.09	y = 27.59	y = 27.65	Δy = -0.06	$\lvert\Delta y\rvert$ = 0.04b
	z = 0.78	z = 28.40	z = 29.27	Δz = -0.87	$\lvert\Delta z\rvert$ = 1.53c
5	x = 12.55	x = 32.27	x = 29.41	Δx = 2.86	$\lvert\Delta x\rvert$ = 3.40a
	y = 46.26	y = 29.83	y = 32.48	Δy = -2.65	$\lvert\Delta y\rvert$ = 1.69b
	z = 52.01	z = 23.01	z = 23.52	Δz = -0.51	$\lvert\Delta z\rvert$ = 0.88c

† The position of the Se atoms in the asymmetric unit after refinement by *SHARP*. ‡ Location of the Se atoms after a 2_1 symmetry transformation of the molecule *A* sites. § Distance between the Se sites of molecule *B* and the 2_1 symmetry transformed Se sites of molecule *A*. ¶ The same distance between sites, but normalized to a percentage of the given unit-cell parameter.

The ten refined Se sites in the asymmetric unit were also used to determine the non-crystallographic symmetry between the two XenA molecules in the asymmetric unit. Application of a 2_1 symmetry operator to chain A yielded sites that could be compared with the observed locations of Se atoms in chain B. As illustrated in Table 2.2, only small differences were identified between crystallographic 2_1 symmetry and the observed local symmetry. Therefore, the local symmetry can be described as a 2_1 screw axis which is displaced approximately one quarter off and nearly parallel to the c axis (Table 2.2). Consequently, the resulting local symmetry yields intensities along (00*l*) that can be described as pseudo-systematic absences.

Primary sequence analyses, catalytic studies and the emerging structural results indicate that XenA is a member of the FMN-dependent oxidoreductase subfamily of the $(\beta/\alpha)_8$ TIM-barrel superfamily [25-27, 36]. XenA shares 27% identity and 44% similarity with old yellow enzyme (OYE), the prototypical member of the subfamily [37-39], while other structurally characterized members of this subfamily include pentaerythritol tetranitrate reductase [40], 2,4-dienoyl-CoA reductase [41], morphinone reductase [42] and the 12-oxophytodienoate reductase isoforms 1 [43] and 3 (PDB code 1q45). Several unsuccessful molecular replacement attempts were made with search models comprised of OYE and other homologs. All of these enzymes are capable of the reduction of unsaturated carbonyl compounds. Thus, it appears that XenA may have evolved from an ancestral enzyme that catalyzed a similar reaction, but structural differences are also likely to be present. More detailed comparisons between the structure, function and evolution of these enzymes will be presented elsewhere. The phases from the refined

XenA structure have been used to calculate electron-density maps that are consistent with ligands such as metronidazole in the active site.

2.5. Acknowledgments

Diffraction data were collected at the Stanford Synchrotron Radiation Laboratory (Stanford University, supported by the Department of Energy, Office of Biological and Environmental Research, the National Institutes of Health, National Center for Research Resources, Biomedical Technology Program and the National Institute of General Medical Sciences) and beamline 22-ID of the SER-CAT facility at the Advanced Photon Source, Argonne National Laboratory (supported by the US Department of Energy, Basic Energy Sciences, Office of Science under Contract No. W-31-109-Eng-38). Support was provided to AMO by the Georgia Tech Research Corporation, the Office of the Vice Provost for Research and the Howard Hughes Medical Institutes (from Dr B. W. Matthews, Institute of Molecular Biology, Howard Hughes Medical Institute and Department of Physics, 1229 University of Oregon, Eugene, Oregon). Support was provided to BGF from NSF MCB-9733734.

2.6. References

1. Mojzsis, S.J., G. Arrhenius, K.D. McKeegan, T.M. Harrison, A.P. Nutman, and C.R. Friend, *Evidence for life on Earth before 3,800 million years ago.* Nature (London), 1996. **384**(6604): p. 55-59.

2. Falkowski, P., R.J. Scholes, E. Boyle, J. Canadell, D. Canfield, J. Elser, N. Gruber, K. Hibbard, P. Hogberg, S. Linder, F.T. Mackenzie, B. Moore, 3rd, T. Pedersen, Y. Rosenthal, S. Seitzinger, V. Smetacek, and W. Steffen, *The global carbon cycle: a test of our knowledge of earth as a system.* Science, 2000. **290**(5490): p. 291-296.

3. Watanabe, Y., J.E. Martini, and H. Ohmoto, *Geochemical evidence for terrestrial ecosystems 2.6 billion years ago.* Nature (London), 2000. **408**(6812): p. 574-578.

4. Nisbet, E.G. and N.H. Sleep, *The habitat and nature of early life.* Nature (London), 2001. **409**(6823): p. 1083-1091.

5. Nelson, K.E., C. Weinel, I.T. Paulsen, R.J. Dodson, H. Hilbert, V.A. Martins dos Santos, D.E. Fouts, S.R. Gill, M. Pop, M. Holmes, L. Brinkac, M. Beanan, R.T. DeBoy, S. Daugherty, J. Kolonay, R. Madupu, W. Nelson, O. White, J. Peterson, H. Khouri, I. Hance, P. Chris Lee, E. Holtzapple, D. Scanlan, K. Tran, A. Moazzez, T. Utterback, M. Rizzo, K. Lee, D. Kosack, D. Moestl, H. Wedler, J. Lauber, D. Stjepandic, J. Hoheisel, M. Straetz, S. Heim, C. Kiewitz, J. Eisen, K.N. Timmis, A. Dusterhoft, B. Tummler, and C.M. Fraser, *Complete genome sequence and comparative analysis of the metabolically versatile Pseudomonas putida KT2440.* Environ. Microbiol., 2002. **4**(12): p. 799-808.

6. Hou, B.K., L.P. Wackett, and L.B. Ellis, *Microbial pathway prediction: a functional group approach.* J. Chem. Inf. Comput. Sci., 2003. **43**(3): p. 1051-1057.

7. Mandelbaum, R.T., L.P. Wackett, and D.L. Allan, *Mineralization of the s-triazine ring of atrazine by stable bacterial mixed cultures.* Appl. Environ. Microbiol., 1993. **59**(6): p. 1695-1701.

8. Souza, M.L.d., J. Seffernick, B. Martinez, M.J. Sadowsky, and L.P. Wackett, *The atrazine catabolism genes atzABC are widespread and highly conserved.* J. Bacteriol., 1998. **180**(7): p. 1951-1954.

9. Wackett, L.P. and L.B. Ellis, *Predicting biodegradation.* Environ. Microbiol., 1999. **1**(2): p. 119-124.

10. Ochman, H., J.G. Lawrence, and E.A. Groisman, *Lateral gene transfer and the nature of bacterial innovation.* Nature (London), 2000. **405**(6784): p. 299-304.

11. Seffernick, J.L. and L.P. Wackett, *Rapid evolution of bacterial catabolic enzymes: a case study with atrazine chlorohydrolase.* Biochemistry, 2001. **40**(43): p. 12747-12753.

12. Wackett, L.P. and C.D. Hershberger, *Biocatalysis and Biodegradation: Microbial Transformation of Organic Compounds*. 2001, Washington, D.C.: USA: ASM Press.

13. Johnson, G.R., R.K. Jain, and J.C. Spain, *Origins of the 2,4-dinitrotoluene pathway.* J. Bacteriol., 2002. **184**(15): p. 4219-4232.

14. Davies, J., *Inactivation of antibiotics and the dissemination of resistance genes.* Science, 1994. **264**(5157): p. 375-382.

15. Mazel, D. and J. Davies, *Antibiotic resistance in microbes.* Cell. Mol. Life Sci., 1999. **56**(9-10): p. 742-754.

16. Rieger, P.G., H.M. Meier, M. Gerle, U. Vogt, T. Groth, and H.J. Knackmuss, *Xenobiotics in the environment: present and future strategies to obviate the problem of biological persistence.* J. Biotechnol., 2002. **94**(1): p. 101-123.

17. Goldstein, B.P., E. Nielsen, M. Berti, G. Bolzoni, and L.G. Silvestri, *The mechanism of action of nitro-heterocyclic antimicrobial drugs. Primary target of 1-methyl-2-nitro-5-vinylimidazole is DNA.* J. Gen. Microbiol., 1977. **100**(2): p. 271-281.

18. Sisson, G., J.Y. Jeong, A. Goodwin, L. Bryden, N. Rossler, S. Lim-Morrison, A. Raudonikiene, D.E. Berg, and P.S. Hoffman, *Metronidazole activation is mutagenic and causes DNA fragmentation in Helicobacter pylori and in Escherichia coli containing a cloned H. pylori RdxA(+) (Nitroreductase) gene.* J. Bacteriol., 2000. **182**(18): p. 5091-5096.

19. Sisson, G., A. Goodwin, A. Raudonikiene, N.J. Hughes, A.K. Mukhopadhyay, D.E. Berg, and P.S. Hoffman, *Enzymes associated with reductive activation and action of nitazoxanide, nitrofurans, and metronidazole in Helicobacter pylori.* Antimicrob. Agents Chemother., 2002. **46**(7): p. 2116-2123.

20. Sakano, K., S. Oikawa, M. Murata, Y. Hiraku, N. Kojima, and S. Kawanishi, *Mechanism of metal-mediated DNA damage induced by metabolites of carcinogenic 2-nitropropane.* Mutat. Res., 2001. **479**(1-2): p. 101-111.

21. Homma-Takeda, S., Y. Hiraku, Y. Ohkuma, S. Oikawa, M. Murata, K. Ogawa, T. Iwamuro, S. Li, G.F. Sun, Y. Kumagai, N. Shimojo, and S. Kawanishi, *2,4,6-trinitrotoluene-induced reproductive toxicity via oxidative DNA damage by its metabolite.* Free Radic. Res., 2002. **36**(5): p. 555-566.

22. Spain, J.C., *Biodegradation of nitroaromatic compounds.* Annu. Rev. Microbiol., 1995. **49**: p. 523-555.

23. Spain, J.C., J.B. Hughes, and H.J. Knackmuss, *Biodegradation of Nitroaromatic Compounds and Explosives*, ed. J.C. Spain, J.B. Hughes, and H.J. Knackmuss. 2000, Boca Raton, FL.: USA: CRC Press.

24. Rosser, S.J., A. Basran, E.R. Travis, C.E. French, and N.C. Bruce, *Microbial transformations of explosives.* Adv. Appl. Microbiol., 2001. **49**: p. 1-35.

25. Blehert, D.S., B.G. Fox, and G.H. Chambliss, *Cloning and sequence analysis of two Pseudomonas flavoprotein xenobiotic reductases.* J. Bacteriol., 1999. **181**(20): p. 6254-6263.

26. Pak, J.W., K.L. Knoke, D.R. Noguera, B.G. Fox, and G.H. Chambliss, *Transformation of 2,4,6-trinitrotoluene by purified xenobiotic reductase B from Pseudomonas fluorescens I-C.* Appl. Environ. Microbiol., 2000. **66**(11): p. 4742-4750.

27. Blehert, D.S., K.L. Knoke, B.G. Fox, and G.H. Chambliss, *Regioselectivity of nitroglycerin denitration by flavoprotein nitroester reductases purified from two Pseudomonas species.* J. Bacteriol., 1997. **179**(22): p. 6912-6920.

28. Studts, J.M. and B.G. Fox, *Application of fed-batch fermentation to the preparation of isotopically labeled or selenomethionyl-labeled proteins.* Protein Expr. Purif., 1999. **16**(1): p. 109-119.

29. Powell, H.R., *The Rossmann Fourier autoindexing algorithm in MOSFLM.* Acta Cryst., 1999. **D55**(Pt 10): p. 1690-1695.

30. Collaborative Computational Project, N., *The CCP4 Suite: Programs for Protein Crystallography. Acta Cryst.*, 1994. **D50**(Pt 5): p. 760-763.

31. Otwinowski, Z. and W. Minor, *Processing of X-ray diffraction data collected in oscillation mode.* Methods Enzymol., 1997. **276**: p. 307-326.

32. Terwilliger, T.C. and J. Berendzen, *Automated MAD and MIR structure solution.* Acta Cryst., 1999. **D55**(Pt 4): p. 849-861.

33. La Fortelle, E. de. and G. Bricogne, *Maximum-likelihood heavy-atom parameter refinement for multiple isomorphous replacement and multiwavelength anomalous diffraction methods.* Methods Enzymol., 1997. **276**(Pt A): p. 472-494.

34. Matthews, B.W., *Solvent content of protein crystals.* J. Mol. Biol., 1968. **33**(2): p. 491-497.

35. Tong, L. and M.G. Rossmann, *Rotation function calculations with GLRF program.* Methods Enzymol., 1997. **276**: p. 594-611.

36. Nagano, N., C.A. Orengo, and J.M. Thornton, *One fold with many functions: the evolutionary relationships between TIM barrel families based on their sequences, structures and functions.* J. Mol. Biol., 2002. **321**(5): p. 741-765.

37. Fox, K.M. and P.A. Karplus, *Old yellow enzyme at 2 Å resolution: overall structure, ligand binding, and comparison with related flavoproteins.* Structure, 1994. **2**(11): p. 1089-1105.

38. Fox, K.M. and P.A. Karplus, *The flavin environment in old yellow enzyme. An evaluation of insights from spectroscopic and artificial flavin studies.* J. Biol. Chem., 1999. **274**(14): p. 9357-9362.

39. Massey, V., *The chemical and biological versatility of riboflavin.* Biochem. Soc. Trans., 2000. **28**(4): p. 283-296.

40. Khan, H., R.J. Harris, T. Barna, D.H. Craig, N.C. Bruce, A.W. Munro, P.C. Moody, and N.S. Scrutton, *Kinetic and structural basis of reactivity of pentaerythritol tetranitrate reductase with NADPH, 2-cyclohexenone, nitroesters, and nitroaromatic explosives.* J. Biol. Chem., 2002. **277**(24): p. 21906-21912.

41. Hubbard, P.A., X. Liang, H. Schulz, and J.J. Kim, *The crystal structure and reaction mechanism of Escherichia coli 2,4-dienoyl-CoA reductase.* J. Biol. Chem., 2003. **278**(39): p. 37553-37560.

42. Barna, T., H.L. Messiha, C. Petosa, N.C. Bruce, N.S. Scrutton, and P.C. Moody, *Crystal structure of bacterial morphinone reductase and properties of the C191A mutant enzyme.* J. Biol. Chem., 2002. **277**(34): p. 30976-30983.

43. Breithaupt, C., J. Strassner, U. Breitinger, R. Huber, P. Macheroux, A. Schaller, and T. Clausen, *X-ray structure of 12-oxophytodienoate reductase 1 provides structural insight into substrate binding and specificity within the family of OYE.* Structure, 2001. **9**(5): p. 419-429.

3. CRYSTALLIZATION AND PRELIMINARY ANALYSIS OF XENOBIOTIC REDUCTASE B FROM *PSEUDOMONAS FLUORESCENS* I-C

3.1 Abstract

Single crystals have been obtained of xenobiotic reductase B (XenB), a flavoenzyme isolated and cloned from *Pseudomonas fluorescens* I-C. The enzyme catalyzes the NADPH-dependent elimination of nitrite from nitroglycerin with an approximately fivefold kinetic preference for the middle nitro group, primarily yielding 1,3-dinitroglycerol. X-ray diffraction data sets have been collected from native crystals to 2.3 Å resolution. The space group is $P4_12_12$, with unit-cell parameters a = b = 140 Å, c = 95.6 Å. The asymmetric unit is likely to contain at least two XenB molecules (V_M = 3.2 $Å^3$ Da^{-1}, 61% solvent) and a molecular-replacement solution has been determined in order to solve the structure.

Formatted from: Orville, A.M., **Manning, L.**, Blehert, D.S., Fox, B.G. & Chambliss, G.H. "Crystallization and preliminary analysis of xenobiotic reductase B and ligand complexes from *Pseudomonas fluorescens* I-C" *Acta Cryst.* ***D*60**, 1289-1291 (2004)

3.2 Introduction

Organic nitrochemicals have been distributed throughout the environment from man-made sources in vast excess over naturally occurring sources. Many of these compounds do not have any known naturally occurring counterpart and present metabolic challenges to many organisms. Moreover, because nitro group metabolism can create reactive nitrogen intermediates [1], the US Environmental Protection Agency often regulates sites contaminated with nitrochemicals.

Elimination of nitrite from an organic nitrochemical is an effective method to initiate catabolism that avoids some of the most reactive nitrogen intermediates. Recent studies have shown that flavoenzymes can utilize at least two mechanistic strategies to catalyze nitrate elimination and permit the organism to obtain all the nitrogen required for growth from the nitrochemical [2]. One strategy, utilized by some lower eukaryotes, exploits enzymes that catalyze the oxidative elimination of nitrite from naturally occurring organic nitrochemicals. The best characterized examples include nitroalkane oxidase (NAO) and 2-nitropropane dioxygenase (NPD) [3-6]. Another strategy, utilized by several prokaryotes, employs enzymes that catalyze reductive nitrite elimination. Indeed, several microbes that utilize nitroglycerin or other organic nitrochemicals as a sole nitrogen source have recently been isolated from the contaminated soil of World War II-era munitions-manufacturing sites [2, 7-9]. In particular, two nutritionally distinct *Pseudomonas* strains isolated from the same munitions-manufacturing site expressed similar flavoenzymes termed xenobiotic reductases A and B (XenA and XenB). While both catalyze NADPH-dependent reductive elimination of nitrite from nitroglycerin, the main product of XenA was 1,2-dinitroglycerol, whereas that of XenB was 1,3-

dinitroglycerol [8]. These two enzymes also exhibited differences in their reactions with 2,4,6-trinitrotoluene, with XenB giving ~50% yield of aromatic ring reduction products at pH 7 [10]. XenA and XenB are members of a class of FMN-dependent old yellow enzyme (OYE) oxidoreductases [11, 12], several of which transform xenobiotic explosive compounds [2, 7-9, 13-25]. The XenA and XenB enzymes have between 27 and 50% sequence identity with these homologs [13].

Clearly, the correct interactions between the enzyme active site residues, the nitro substrate and flavin cofactor are all essential to achieve catalytic nitrite elimination. However, the structural and mechanistic elements that control these interactions, the partition between oxidative and reductive nitrite-elimination reactions and the regiospecificity of catalysis have not been well established. To that end, we have recently reported the crystallization and preliminary characterization of XenA cloned from *Pseudomonas putida* II-B [25]. The focus of this report is the crystallization of XenB cloned from *P. fluorescens* I-C [8, 10, 13].

3.3 Material and Methods

3.3.1. Protein Expression and Purification

P. fluorescens I-C was isolated as previously reported [8] from nitro-contaminated soil at the Badger Army Ammunition Plant, Wisconsin, USA. This bacterium was enriched by its ability to obtain all nitrogen required for growth from concentrations of nitroglycerin that are toxic to nearly all other species. XenB (37 441 Da monomer) was cloned, expressed and purified as previously reported [8, 13] The enzyme

was indistinguishable when isolated from either *P. fluorescens* I-C or the *Escherichia coli* expression host, including the presence of one oxidized FMN per protein monomer.

3.3.2. Crystallization

Crystallization conditions for XenB were determined from sparse-matrix screens and optimized using additive and detergent screens from Hampton Research (Laguna Nigel, CA, USA). Typically, 2 ml protein (5-10 mg ml^{-1} in 20 m*M* HEPES buffer pH 7.0) was mixed with an equal volume of reservoir solution on a silanized cover slip and equilibrated at 277 K or room temperature by vapor diffusion in 24-well Linbro plates. XenB crystals typically required more than three weeks to grow when the drops were suspended over well solutions containing 100 m*M* PIPES buffer pH 5.5-6.5 with approximately 24% polyethylene glycol (PEG 4000, 6000 or 8000) and 200 m*M* MgSO4. The crystals first appeared as long needles at the border of a phase-separated region of the drops. The addition of 1 ml detergent (e.g. 0.7 m*M* HEGA-10, 0.25 m*M* n-decanoylsucrose or 0.2 m*M* Zwittergent 3-12; Anatrace Inc., Maumee, OH, USA) to the drop reduced phase separation and increased the reproducibility of crystal formation.

3.3.3. X-ray Diffraction Data Collection and Analysis

Crystals were harvested with a nylon loop and transferred to cryoconditions, which included either briefly passing the crystals through mother liquor augmented with at least 17% glycerol or transferring the crystals to Paratone-N (Hampton Research). The crystals were flash-frozen by either rapidly plunging them into liquid N_2 or by exposing

Table 3.1: Data-collection statistics for XenB. Data were collected at SSRL beamline 9-1 with 0.9778 Å X-rays and a Quantum 4R detector. Values for the highest resolution shell of data are given in parentheses.

Dataset		Native 1	Native 2
Distance (mm)		225	250
Exposure time (s)		20	10
Oscillation per image (°)		0.75	1.0
No. images		132	90
Resolution range (Å)		28-2.3	30-2.3
Space group		$P4_12_12$	$P4_12_12$
Unit-cell parameters	$a = b$ (Å)	140.4	139.9
	c (Å)	95.6	94.8
Total reflections		305018	225745
Unique reflections		40812	35056
Multiplicity		7.4 (4.9)	6.2 (3.7)
Completeness (%)		92.1 (97.1)	87.2 (87.2)
R_{sym}†		0.126 (0.41)	0.095 (0.34)
$I/\sigma(I)$‡		4.7 (1.8)	6.2 (2.2)
Mosaic spread (°)		~0.8	~0.6

† R_{sym}(I) gives the average agreement between the independently measured intensities such as $\sum_h\sum_i|I_i - I|/\sum_h\sum_i I$, where I is the mean intensity of the i observations of reflection h. ‡ $I/\sigma(I)$ is the root-mean-square value of the intensity measurements divided by their estimated standard deviation.

them to the cold-stream of the X-ray source. All diffraction data were collected at beamline 9-2 of the Stanford Synchrotron Radiation Laboratory from crystals held at approximately 100 K. The detector was an ADSC Quantum 4R CCD detector (Poway, CA, USA). Various exposure times, crystal-to-detector distances and oscillation ranges per frame were used (table 3.1). The data were integrated with *MOSFLM* [26] and internally scaled with *SCALA* from the *CCP4* suite of programs [27]. Molecular replacement was carried out with the *MOLREP* routine in *CCP4* by searching for two or three molecules in the asymmetric unit with an input search molecule derived from morphinone reductase (PDB code 1gwj; [28]) and the resolution range 28-3.0 Å. Rigid-body refinement of the potential solutions took place using *REFMAC5* from *CCP4*.

3.4 Results and Discussion

Crystals of XenB were birefringent elongated needles (Figure 3.1) that were intensely yellow when viewed with unpolarized light. They took much longer to appear than the equilibration of the hanging drops suspended over various well solutions. The enzyme did not precipitate in the drops during the incubation period; the drops often remained clear for several months, especially when incubated at 277 K. If detergents were omitted from the drops, they often separated into clear and yellow phases. The addition of various detergents reduced the tendency for phase separation and increased the reproducibility of obtaining crystals, but did not significantly reduce the time required for crystallization. Thus, it appears that crystal nucleation may be the rate-limiting step in the crystallization of XenB.

X-ray diffraction data-collection statistics for the two data sets are presented in Table 3.1. Analysis of the data suggested that the crystals belong to a primitive tetragonal space group. Both data sets included reflections along the (*h*00) principal axis that exhibited systematic absences. For example, the native 1 and native 2 data sets had average values for $I/\sigma(I)$ for (even, 0, 0) reflections of 26.4 and 17.2, respectively, whereas the (odd, 0, 0) reflections yielded average values of 0.09 and 0.18, respectively. However, there were no reflections observed for the principal axis (00*l*) for any of the data sets. Therefore, the space-group determination remained ambiguous based upon reflection-intensity data, but they were all consistent with space groups $P42_12$, $P4_12_12$, $P4_22_12$ or $P4_32_12$. A reasonable assumption of the weight per unit volume suggested that two XenB molecules were present in the asymmetric unit (V_M = 3.2 or 2.1 Å^3 Da^{-1}, 61 or 41% solvent content, respectively; [29]).

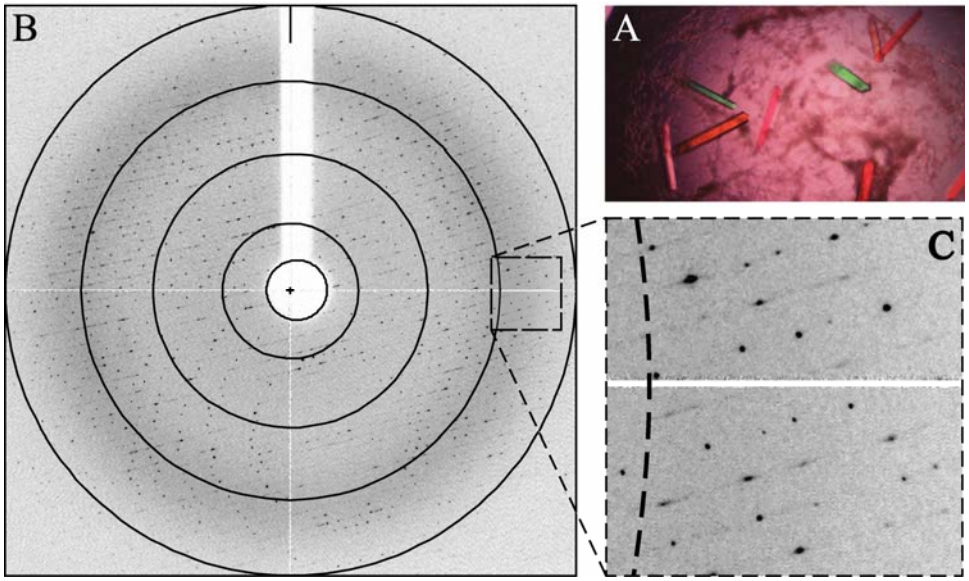

Figure 3.1: A, Crystals of XenB measuring ~0.3 × 0.05 mm photographed with polarization. **B,** The X-ray diffraction pattern for native 1 with a 20 s exposure and 0.75° oscillation about the vertical axis. The arcs indicate 2.7, 3.6, 5.5, 10.9 and 28 Å resolution, respectively. **C,** An expanded view of the high-resolution diffraction perpendicular to the oscillation axis.

Morphinone reductase (PDB code 1gwj; [28]) has 50% sequence identity to XenB and was used to prepare a monomeric molecular-replacement search model comprised of 276 residues out of the 349 residues in full-length XenB. All four space groups and both native data sets were analyzed for molecular-replacement solutions. For each data set the best solutions were for two molecules in the asymmetric unit in space group $P4_12_12$. These yielded correlation coefficients of 0.58 and 0.57, which were significantly better than analogous trials in the other space groups (the correlation coefficients ranged between 0.45 and 0.49). Moreover, the crystal packing, solvent content and interpretable electron density maps are all consistent with two XenB molecules in space group $P4_12_12$. Refinement of the atomic models to the high-resolution limit for each data set are in progress.

Widely divergent flavoenzymes catalyze a remarkable range of reactions in biology [30, 31]. The results from XenB, in comparison to our emerging results for XenA [25], will help define the structural basis of regiospecific reductive nitrite elimination by flavoenzymes [13, 16, 24]. Moreover, by extending the comparisons to enzymes such as NAO and NPD, which catalyze oxidative nitrite-elimination reactions, broader mechanistic insights can be achieved.

3.5. Acknowledgments

Support was provided to AMO by the Howard Hughes Medical Institutes (from Dr B. W. Matthews, Institute of Molecular Biology, Howard Hughes Medical Institute and Department of Physics, 1229 University of Oregon, Eugene, Oregon), the Georgia Tech Research Corporation and the Office of the Vice Provost for Research, Georgia Institute of Technology and an American Chemical Society Petroleum Research Fund type G grant (40310-G4). Support was provided to BGF by the NSF, MCB-9733734. We thank D. Anstrom for assistance with initial crystallization trials and Dr M. Sagermann for assistance with data collection. Portions of this research were carried out at the Stanford Synchrotron Radiation Laboratory (Stanford University, supported by the Department of Energy, Office of Biological and Environmental Research, the National Institutes of Health, National Center for Research Resources, Biomedical Technology Program and the National Institute of General Medical Sciences).

3.6. References

1. Nathan, C. and M.U. Shiloh, *Reactive oxygen and nitrogen intermediates in the relationship between mammalian hosts and microbial pathogens.* Proc. Natl. Acad. Sci. U.S.A., 2000. **97**(16): p. 8841-8848.

2. Spain, J.C., *Biodegradation of nitroaromatic compounds.* Annu. Rev. Microbiol., 1995. **49**: p. 523-555.

3. Tchorzewski, M., T. Kurihara, N. Esaki, and K. Soda, *Unique primary structure of 2-nitropropane dioxygenase from Hansenula mrakii.* Eur. J. Biochem., 1994. **226**(3): p. 841-846.

4. Gadda, G. and P.F. Fitzpatrick, *Biochemical and physical characterization of the active FAD-containing form of nitroalkane oxidase from Fusarium oxysporum.* Biochemistry, 1998. **37**(17): p. 6154-6164.

5. Gorlatova, N., M. Tchorzewski, T. Kurihara, K. Soda, and N. Esaki, *Purification, characterization, and mechanism of a flavin mononucleotide-dependent 2-nitropropane dioxygenase from Neurospora crassa.* Appl. Environ. Microbiol., 1998. **64**(3): p. 1029-1033.

6. Zhang, J. and H. Tan, *Cloning, expression and characterization of a gene encoding nitroalkane- oxidizing enzyme from Streptomyces ansochromogenes.* Eur. J. Biochem., 2002. **269**(24): p. 6302-6307.

7. Binks, P.R., C.E. French, S. Nicklin, and N.C. Bruce, *Degradation of pentaerythritol tetranitrate by Enterobacter cloacae PB2.* Appl. Environ. Microbiol., 1996. **62**(4): p. 1214-1219.

8. Blehert, D.S., K.L. Knoke, B.G. Fox, and G.H. Chambliss, *Regioselectivity of nitroglycerin denitration by flavoprotein nitroester reductases purified from two Pseudomonas species.* J. Bacteriol., 1997. **179**(22): p. 6912-6920.

9. French, C.E., S. Nicklin, and N.C. Bruce, *Aerobic degradation of 2,4,6-trinitrotoluene by Enterobacter cloacae PB2 and by pentaerythritol tetranitrate reductase.* Appl. Environ. Microbiol., 1998. **64**(8): p. 2864-2868.

10. Pak, J.W., K.L. Knoke, D.R. Noguera, B.G. Fox, and G.H. Chambliss, *Transformation of 2,4,6-trinitrotoluene by purified xenobiotic reductase B from Pseudomonas fluorescens I-C.* Appl. Environ. Microbiol., 2000. **66**(11): p. 4742-4750.

11. Åkeson, Å., A. Ehrenberg, and H. Theorell, *Old Yellow Enzyme*, in *The Enzymes*, P.D. Boyer, Editor. 1963, Academic Press: New York:. p. 477-494.

12. Fox, K.M. and P.A. Karplus, *Old yellow enzyme at 2 Å resolution: overall structure, ligand binding, and comparison with related flavoproteins.* Structure, 1994. **2**(11): p. 1089-1105.

13. Blehert, D.S., B.G. Fox, and G.H. Chambliss, *Cloning and sequence analysis of two Pseudomonas flavoprotein xenobiotic reductases.* J. Bacteriol., 1999. **181**(20): p. 6254-6263.

14. Nivinskas, H., R.L. Koder, Z. Anusevicius, J. Sarlauskas, A.F. Miller, and N. Cenas, *Two-electron reduction of nitroaromatic compounds by Enterobacter cloacae NAD(P)H nitroreductase: description of quantitative structure- activity relationships.* Acta Biochim. Pol., 2000. **47**(4): p. 941-949.

15. Riefler, R.G. and B.F. Smets, *Enzymatic Reduction of 2,4,6-trinitrotoluene and related nitroarenes: kinetics linked to one-electron redox potentials.* Environ. Sci. Technol., 2000. **34**(18): p. 3900-3906.

16. Williams, R.E. and N.C. Bruce, *The role of nitrate ester reductase enzymes in the biodegradation of explosives*, in *Biodegradation of nitroaromatic compounds and explosives*, J.C. Spain, J.B. Hughes, and H.J. Knackmuss, Editors. 2000, Lewis Publishers: Boca Raton:. p. 161-184.

17. Barna, T.M., H. Khan, N.C. Bruce, I. Barsukov, N.S. Scrutton, and P.C. Moody, *Crystal structure of pentaerythritol tetranitrate reductase: "flipped" binding geometries for steroid substrates in different redox states of the enzyme.* J. Mol. Biol., 2001. **310**(2): p. 433-447.

18. Ebert, S., P. Fischer, and H.J. Knackmuss, *Converging catabolism of 2,4,6-trinitrophenol (picric acid) and 2,4- dinitrophenol by Nocardioides simplex FJ2-1A.* Biodegradation, 2001. **12**(5): p. 367-376.

19. Meah, Y., B.J. Brown, S. Chakraborty, and V. Massey, *Old yellow enzyme: reduction of nitrate esters, glycerin trinitrate, and propylene 1,2-dinitrate.* Proc. Natl. Acad. Sci. U.S.A., 2001. **98**(15): p. 8560-8565.

20. Haynes, C.A., R.L. Koder, A.F. Miller, and D.W. Rodgers, *Structures of nitroreductase in three states: effects of inhibitor binding and reduction.* J. Biol. Chem., 2002. **277**(13): p. 11513-11520.

21. Johnson, G.R., R.K. Jain, and J.C. Spain, *Origins of the 2,4-dinitrotoluene pathway.* J. Bacteriol., 2002. **184**(15): p. 4219-4232.

22. Khan, H., R.J. Harris, T. Barna, D.H. Craig, N.C. Bruce, A.W. Munro, P.C. Moody, and N.S. Scrutton, *Kinetic and structural basis of reactivity of pentaerythritol tetranitrate reductase with NADPH, 2-cyclohexenone, nitroesters, and nitroaromatic explosives.* J. Biol. Chem., 2002. **277**(24): p. 21906-21912.

23. Koder, R.L., C.A. Haynes, M.E. Rodgers, D.W. Rodgers, and A.F. Miller, *Flavin thermodynamics explain the oxygen insensitivity of enteric nitroreductases.* Biochemistry, 2002. **41**(48): p. 14197-14205.

24. Williams, R.E. and N.C. Bruce, *New uses for an Old Enzyme'--the Old Yellow Enzyme family of flavoenzymes.* Microbiology, 2002. **148**(Pt 6): p. 1607-1614.

25. Orville, A.M., L. Manning, D.S. Blehert, J.M. Studts, B.G. Fox, and G.H. Chambliss, *Crystallization and preliminary analysis of xenobiotic reductase A and ligand complexes from Pseudomonas putida II-B.* Acta Crystallog., 2004. **D60**(Pt 5): p. 957-961.

26. Powell, H.R., *The Rossmann Fourier autoindexing algorithm in MOSFLM.* Acta Cryst., 1999. **D55**(Pt 10): p. 1690-1695.

27. Collaborative Computational Project, N., *The CCP4 Suite: Programs for Protein Crystallography. Acta Cryst.*, 1994. **D50**(Pt 5): p. 760-763.

28. Barna, T., H.L. Messiha, C. Petosa, N.C. Bruce, N.S. Scrutton, and P.C. Moody, *Crystal structure of bacterial morphinone reductase and properties of the C191A mutant enzyme.* J. Biol. Chem., 2002. **277**(34): p. 30976-30983.

29. Matthews, B.W., *Solvent content of protein crystals.* J. Mol. Biol., 1968. **33**(2): p. 491-497.

30. Fraaije, M.W. and A. Mattevi, *Flavoenzymes: diverse catalysts with recurrent features.* Trends Biochem. Sci., 2000. **25**(3): p. 126-132.

31. Massey, V., *The chemical and biological versatility of riboflavin.* Biochem. Soc. Trans., 2000. **28**(4): p. 283-296.

4. CRYSTALLOGRAPHIC ANALYSIS AND STRUCTURE DETERMINATION OF XENOBIOTIC REDUCTASE B FROM *PSEUDOMONAS FLUORESCENS* I-C

4.1 Abstract

The crystallization and preliminary analysis of xenobiotic reductase B (XenB) from *Pseudomonas fluorescens* I-C [1] reports the initial crystal characterization for XenB. Native XenB was originally indexed in space group $P4_12_12$ with unit cell parameters $a = b = 140.4$ Å and $c = 95.6$ Å with two molecules present in the asymmetric unit and 61% solvent content. However, refinement of this solution never reached satisfactory statistics (R = 32.9 % and R_{free} = 42.6 %) and large areas with mystery density were observed in the $2mF_o - DF_c$ electron density maps that could be interpreted as protein density and appeared to be 'shadow' images of XenB molecules overlapping with the original chains. These crystals for XenB were shown to exhibit pseudo-symmetry where the initial space group is too small. The actual space group in which XenB crystallized was also primitive tetragonal $P4_12_12$ but had unit cell dimensions of $a = b = 197.8$ Å and $c = 94.8$ Å where crystal packing for both space groups was nearly identical but differences in the asymmetric unit content and orientation resulted in the

formation of these 'shadows' in the smaller unit cell due solely to the space group symmetry of the actual, larger cell.

4.2 Introduction

The crystallization and preliminary analysis of xenobiotic reductase B (XenB) from *Pseudomonas fluorescens* I-C [1] reports the initial crystal characterization for XenB. The X-ray diffraction sets that were collected had a resolution limit to 2.3 Å. Both datasets were indexed and integrated in space group $P4_12_12$ with unit cell parameters a = b = 140.4 Å and c = 95.6 Å. Based on a reasonable assumption of the weight per unit volume, two XenB molecules were present in the asymmetric unit (V_M = 3.2 or 2.1 $Å^3$ Da^{-1}, 61 or 41% solvent content, respectively [2, 3], Figure 4.1). Table 3.1 lists the data collection and integration statistics for both native datasets. A molecular replacement solution based on the structure of morphinone reductase (PDB code 1gwj; [4]) was attempted to solve the three dimensional structure of XenB. Morphinone reductase has 50% sequence identity to XenB and was used to prepare a monomeric molecular replacement search model comprised of 276 residues out of the 349 residues in full-length XenB. At this stage in the structure determination of XenB, the exact tetragonal space group was ambiguous due to the absence of nearly all principle axes reflections, therefore, all eight space groups and both native data sets were analyzed for molecular replacement solutions (Table 4.1) using the same molecular replacement search model. For each data set the best solutions were found using two molecules in the asymmetric unit in space group $P4_12_12$ and yielded a correlation coefficient of 0.77 for native data set

1, which is significantly better than analogous trials in the other space groups (the correlation coefficients ranged between 0.14 and 0.71). Moreover, the crystal packing, solvent content and interpretable electron density maps were all consistent with two XenB molecules in the asymmetric unit of a space group $P4_12_12$.

Table 4.1 also lists the refinement statistics for the atomic models of XenB both native datasets to the resolution limit of 2.3 Å. Although the two chains for XenB fit the density very well (Figure 4.2A), the resulting R and R_{free} values are troublesome. More accurately, an R_{free} value deviating by more than 10 % from the accompanying R value is troublesome and indicative of a serious mistake. The traditional R-factor is defined as:

$$R = \frac{\sum \| F_O | - | F_C \|}{\sum | F_O |}$$

where R represents the quality of the fit of a model to the diffraction data by measuring the discrepancy between the observed (F_o) and calculated (F_c) structure factor amplitudes. However, this R value is easily corrupted by increasing the parameter to observation ratio. Several examples of models with acceptable R values are known that had serious errors [5-7]. This problem was overcome by the introduction of an R_{free} [7-9], a factor that is the same as the conventional R-factor but is calculated from a small percentage (usually ~5-10 %) of reflections that were excluded from the refinement. The R_{free} then measures the agreement between observed and calculated structure factor amplitudes for a test set of reflections that is omitted in the modeling and refinement process and therefore cannot decrease during wrong refinements of a model but only during the course of successful model refinement. In practice, this means that a very high R_{free} value (> 0.40) is indicative of a model with serious errors and becomes unrelated to the value for the conventional R, which can be very low (~ 0.20). Ideally, the difference

between R and R_{free} should be as small as possible and depends on multiple factors [8]: a) the quality of the data (R_{sym}, $I/\sigma(I)$, completeness and multiplicity), b) the global correctness of the model, c) the completeness of the model and d) the degree of over-fitting which is reflected by a high parameter to observation ratio. Tickle *et al*. (1998) describes how to calculate an estimate for the ratio of R_{free} and R [10]. As a general rule, a large difference between R and R_{free} can be defined as more than 0.1 at 3 Å resolution or 0.05 at 2 Å resolution. A survey conducted by Kleywegt & Brünger (1996) lists an average value for R of 0.20 and an average value for R_{free} of 0.26 for some of the major journals in which macromolecular X–ray structures were published during January 1st and June 30th of 1996, totaling 179 structures for which an R_{free} was published [6]. Table 4.2 shows acceptable values for R and R_{free} with respect to resolution.

Table 4.1: Refinement statistics for two native datasets of XenB.

Space group	No. molecules expected/found	Molecular replacement (R, Corr.)	Refinement statistics for dataset indexed in $P4_12_12$ (*bold*)	Native 1	Native 2
$P4$	4/4	R=0.92, Corr.=0.17	Resolution range (Å)	28-2.3	30-2.3
$P4_1$	4/4	R=0.54, Corr.=0.71	Number of reflections	37311	33031
$P4_2$	4/3	R=0.92, Corr.=0.15	R (%)	32.9	32.1
$P4_3$	4/3	R=0.89, Corr.=0.18	R_{free} (%) (10 % data)	42.6	41.4
$P422$	2/1	R=0.93, Corr.=0.15	Number of non-H atoms	5340	5344
$P42_12$	2/2	R=0.71, Corr.=0.49	Number of protein residues	699	699
$P4_122$	2/1	R=0.81, Corr.=0.38	Number of water molecules	---	---
$P4_12_12$	**2/2**	***R*=0.50, Corr.=0.77**	Average B values (Å^2)	16.4	12.1
$P4_222$	2/1	R=0.94, Corr.=0.14	Protein	12.2	16.4
$P4_22_12$	2/2	R=0.68, Corr.=0.53	FMN	7.6	16.5
$P4_322$	2/1	R=0.90, Corr.=0.21	R.m.s.d from ideal geometry		
$P4_32_12$	2/1	R=0.90, Corr.=0.20	Bond lengths (Å)	0.05	0.06
			Bond angles (°)	4.1	4.3

Table 4.2: Generally acceptable values for R and R_{free} with respect to resolution range.

Resolution (Å)	R range	R_{free} range
3.5	~ 0.25 - 0.3	~ 0.3 - 0.35
2.5	~ 0.17 - 0.25	~ 0.23 - 0.3
2.0	~ 0.15 - 0.22	~ 0.2 - 0.25

4.3 The Electron Density Maps for XenB

Electron density maps were calculated for both native datasets for XenB based on the models listed in Table 4.1. The quality of these σ_A-weighted $2mF_o - DF_c$ and $mF_o - DF_c$ electron density maps to 2.3 Å are reasonable (Figure 4.2A). However, upon closer examination, unusual features were observed (Figure 4.2B). Although two complete chains for XenB were built into the density with reasonable certainty, large portions of mystery density remained. Initially it was assumed that this mystery density could be explained with detergent molecules lining the protein monomers, but this strategy was quickly abandoned since no detergent molecules could be placed in this mystery density with any degree of certainty. In addition, it appeared that this mystery density was only present on one side of the protein monomer and was the same for each monomer in the asymmetric unit. Further inspection of this mystery density lead to the observation that it resembles actual protein density. Electron density that appeared α-helical in nature could be clearly seen. Since both monomers were built in completely with reasonable certainty, this α-helical mystery density could stem from additional monomers in the asymmetric unit. Although according to solvent content analysis [2], XenB was thought to have two monomers per asymmetric unit (V_M = 3.2 Å^3 Da^{-1}, 61% solvent), three molecules per asymmetric unit is a possibility as well (V_M = 2.1 Å^3 Da^{-1}, 41% solvent) (Figure 4.1).

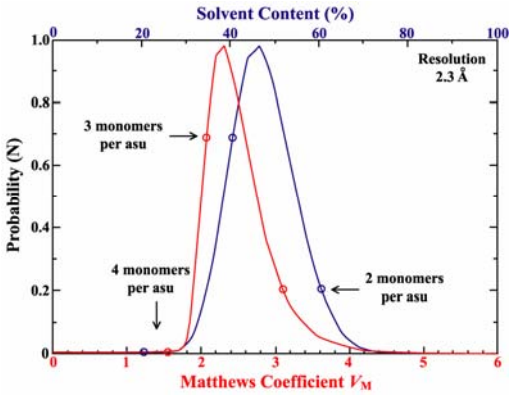

Figure 4.1: Matthew's probability curve for XenB to 2.3 Å resolution calculating the number of monomers per asymmetric unit possible based on solvent content (blue) and Matthew's coefficient (red) (http://ruppweb.dyndns.org, [3]).

The possibility for four molecules per asymmetric unit is virtually zero [3]. However, the mystery density observed in the electron density maps occurs near the active site on one side of the monomer, is the same for both monomers in the asymmetric unit and is supported by observed $mF_o - DF_c$ electron density (3σ). Since it is not possible to account for all observed mystery density with placement of one additional monomer (C) of XenB and placing two additional monomers (C and D) is excluded as a possibility by solvent content analysis, it is unlikely that a wrong number of monomers per asymmetric unit can account for the unusual features observed in the σ_A-weighted $2mF_o - DF_c$ and $mF_o - DF_c$ electron density maps.

If full length XenB chains (C and D) are built into the observed electron density, these additional chains perfectly account for all unexplained mystery density (Figure 4.2C). However, C and D would overlap with the two original monomers (A and B) from which the phases were calculated. More precisely, two-fold symmetry axes relate A with C and B with D and are located approximately at special positions (x , ½ , ¼) and (x , ½ , ¾) as is calculated from the three dimensional coordinates of all four monomers

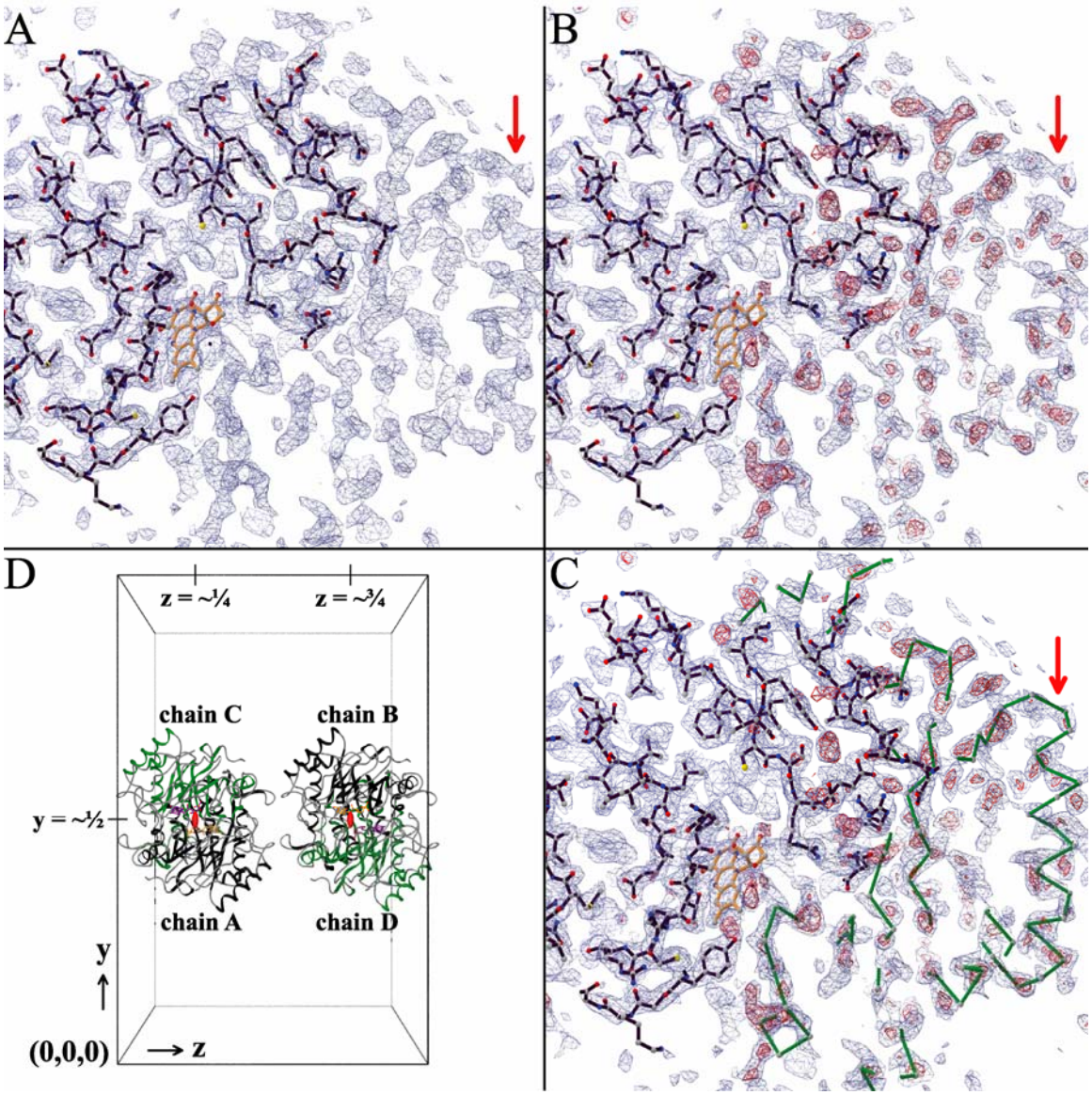

Figure 4.2: Unusual features observed in the σ_A-weighted electron density maps (1σ contours, 28 – 2.3 Å resolution) calculated for XenB (R = 32.1 %, R_{free} = 41.4 %). **A,** The $2mF_o - DF_c$ electron density is shown in blue with chain A and the FMN drawn in black and orange ball-and-sticks respectively. An example of α-helical mystery density is indicated by a red arrow. **B,** The same as (A) with added in red the σ_A-weighted $mF_o - DF_c$ electron density (3σ contours, 28 – 2.3 Å resolution). **C,** The same as (B) with added in green the C_α-trace for an additional monomer, C, accounting for all mystery density and satisfying the expected α-helical mystery density indicated by a red arrow. **D,** A representation of the unit cell of XenB (a = b = 139.9 Å and c = 94.8 Å) showing all four monomers (A, B, C and D) that can be placed in the electron density calculated using phases derived from chains A and B and the manner in which they overlap. Chains are drawn as black (A and B) or green (C and D) ribbons with the FMN represented by orange (A and B) or purple (C and D) ball-and-sticks. The 2-fold symmetry axes that relate these monomers are indicated by red ellipses.

now present (A, B, C and D). In case of the first pair of overlapping monomers (A and C), the difference between special position (*x* , ½ , ¼) and the actual position of the two-fold symmetry axis calculated from the three dimensional coordinates of A and C is negligible: (*x*, 69.93, 23.70) vs. (*x*, 69.95, 22.14) with percent errors of (*x*, 0.01%, 1.6%) and the difference between the special position (*x* , ½ , ¾) and the actual position of the two-fold symmetry axis relating B and D is (*x*, 69.93, 71.1) versus (*x*, 69.89, 69.55) with percent errors of (*x*, 0.03%, 1.6%). Constructing a 'CD'-dimer from their symmetry mates in the same orientation with respect to each other as initial 'AB' dimer results in an additional asymmetric unit that is translated with respect to the asymmetric unit of the 'AB' dimer by 53.6 Å in the *z*-direction (Figure 4.3). This is a translation of a little more than half a unit cell in the *z*-direction CD.

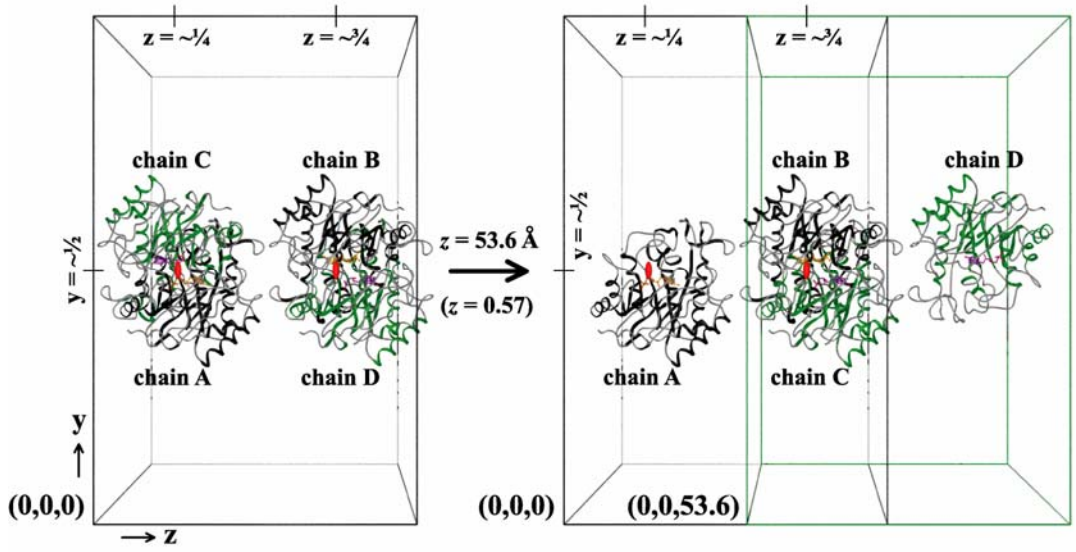

Figure 4.3: Schematic representation of the two possible 'dimers' in the asymmetric unit of XenB. Chains A and B are shown as black ribbon drawings with their FMNs drawn as orange ball-and-sticks. Chains C and D are shown as green ribbon drawings with their FMNs drawn as purple ball-and-sticks. The two-fold symmetry elements are indicated by red ellipses. The figure shows the relationship between the two possible unit cells and illustrates the translation in the *z*-direction between them

Several crystallographic phenomenon could potentially explain the behavior observed for both native data sets collected for XenB: a) twinning, b) anisotropy, c) pseudo-centering and d) pseudo-symmetry.

4.4 Crystallographic Phenomenon Potentially Occurring in XenB

4.4.1. Twinning

Twinning is an anomaly in crystal growth where the crystal is composed of separate domains that differ in their orientations with respect to each other in a distinct and well-defined manner [11]. Many different crystal growth anomalies are known, but twinning refers to very special cases where some or all of the lattice directions in the separate domains are parallell and leads to either partial or complete coincidence between the lattices of the distinct domains. Twinning was detected early on by crystallographers such as Bravais, Mallard and Friedel [12-14]. and can easily prevent successful structure determination and more often than not the problem is circumvented completely by searching for crystallization conditions that do not give twinned crystals or entirely different crystal forms.

Two important facts in twinning need to be considered: 1) in a twinned crystal composed of two or more domains, the orientations of these domains are related by one or more symmetry elements that are not part of the space group symmetry of the crystal, and 2) the additional symmetry elements must be encountered in crystal morphology, i.e. a center of symmetry, a mirror plane (parallel to a lattice plane) or a 2-, 3-, 4- or 6-fold rotation axis (parallel to a lattice row common to all domains) [15]. There are two

fundamentally different categories of twinning, non-merohedral or 'epitaxial' twinning and merohedral twinning.

4.4.1.1 Non-merohedral Twinning

Non-merohedral twinning (Figure 4.4A) can be recognized during data collection when difficulties with indexing are observed or the diffraction pattern shows signs of multiple sets of reciprocal lattices. This is an example of twinning where the overlap of the different domains occurs in fewer than three dimensions, their crystal lattices are not super-imposable. The reflections in the diffraction pattern can be integrated if an indexing routine can identify one lattice exclusively and ignoring the presence of the second lattice. No evidence of non-merohedral twinning was observed in diffraction images of XenB.

4.4.1.2 Merohedral Twinning

Merohedrally twinned crystals (Figure 4.4B) have twin symmetry elements that are not part of the space group symmetry but are part of the same Laue group. In this type of twinning, different domains have exactly overlapping lattice in three dimensions, direct and reciprocal. This way, the crystal appears to be a single crystal until near the end of refinements. The diffraction patters will not reveal obvious abnormalities, but each observed intensity will contain contributions from crystallographically unrelated reflections that are related by a twin operator (twin law). For proteins, domains that have crystallographically distinct orientations can have super-imposable lattices when the

rotational symmetry of the lattice exceeds the rotational symmetry of the crystal space group. This can only be true for space goups that are based on point symmetries 3, 32 (hexagonal but not rhombohedral), 4, 6 and 23. The only kind of merohedral twinning that has ever been reported in macromolecules is hemihedral twinning, where only two distinct orientations exist in the same crystal.

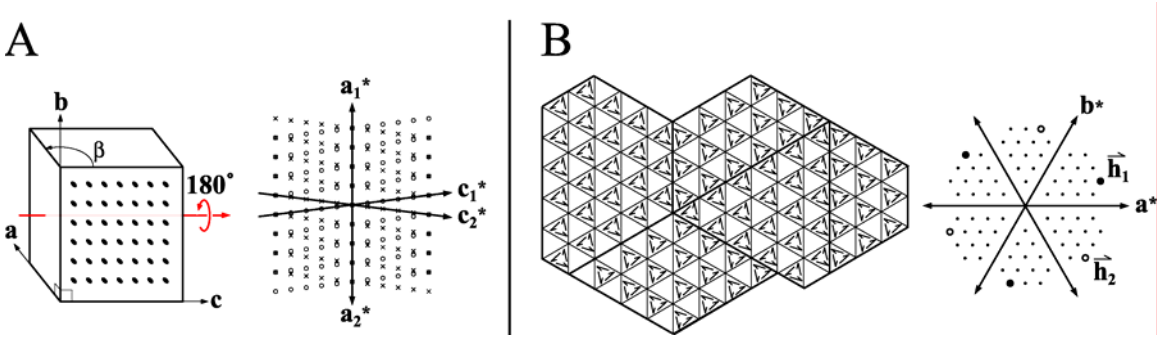

Figure 4.4: Hypothetical examples for non-merohedral and merohedral twinning. **A,** Non-merohedral twinning, *left*: a monoclinic crystal presents a rectangular arrangement of molecules at one of its faces. Rotation about the indicated axis produces a second twin domain with molecular spacings that match those of the first domain. *Right*: The diffraction pattern from the resulting twinned specimen consists of two distinct lattices that overlap exactly when l is zero and nearly overlap elsewhere (e.g., when l is 5). **B,** Merohedral twinning, *left*: Separate domains with $P3$ symmetry are related by a 180° rotation about an axis parallel to the three-fold crystallographic axis. The arrows represent individual molecules. The twinning is hemihedral, having two distinct domain orientations. The domain boundaries are indicated by bold lines. *Right*: The observed diffraction pattern appears to be normal. But each of the observed intensities contains contributions from two reflections, $\mathbf{h}_1$ and $\mathbf{h}_2$, which are related by the twinning operator but are crystallographically independent. (for $l \neq 0$). A set of related reflections is indicated. If the two distinct domain orientations are represented equally in the specimen (twin fraction of ½), the observed intensities of twin-related reflection (open and filled circles) are equal and the diffraction pattern gains additional symmetry. This figure was reproduced from Yeates, T.O., (1997), *Methods Enzymol.*, **276**:344-358 [11].

4.4.1.3 Hemihedral Twinning

Hemihedrally twinned crystals have two distinct domains that overlap exactly in their direct and reciprocal lattices, resulting in diffraction patterns where each observed intensity has contributions from two crystallographically unrelated reflections that are related to each other by a twin operator. They do so with weights determined by their fractional volumes called the twinning fraction α, where $\alpha = 0$ represents an untwinned crystal. Depending on this twin fraction, two different types can be distinguished. First, the case where $\alpha \approx ½$ is called perfect twinning, In this case, the symmetry of the twinning operation is imposed on top of the Laue symmetry leading to erroneously high symmetry. The true crystallographic intensities cannot be recovered directly, but require more elaborate measures. Secondly, partial twinning is defined by $\alpha < ½$, and does not obscure the true crystallographic symmetry. The observed intensity of any given reflection is equal to:

$$\alpha \times I_{(hkl)} + (1-\alpha) \times I_{(h'k'l')}$$

Where hkl and h'k'l' are twin-related indices. Statistical analysis can be used to estimate the twin fraction, after which the date can be corrected [11].

4.4.1.4 Is XenB Twinned?

XenB has been extensively analyzed for twinning. Common simple indicators for the presence of twinning in a crystal are; -the unit cell is too small to contain the known molecule(s) under the apparent space group symmetry, -the intensity distribution does not follow Wilson statistics [16], -the space group appears to be either tetragonal or trigonal,

-The structure will not solve from apparent good data and -irreducible *R* factor from apparently good diffraction data. The data sets collected for XenB showed some of these twin indicators, but others were not observed. Although XenB can be indexed and integrated in a number of space groups varying from tetragonal to orthorhombic, monoclinic and, of course, primitive, in neither of these space groups could a twin operator be found. In addition, a Wilson's statistical test can be performed by a web-server (http://nihserver.mbi.ucla.edu/Twinning) to inspect a data set for the presence of partial or perfect merohedral twinning [11]. This web-server uses normalized data or thin shells of data to calculate $\langle I^2 \rangle / \langle I \rangle^2$. The expected value is 1.5 for (acentric) perfectly twinned data and 2.0 for (acentric) untwinned data. The data sets collected for XenB both resulted in very different values calculated for $\langle I^2 \rangle / \langle I \rangle^2$, in the range of 2.5 – 5.1, which can be indicative of a crystal that diffracts highly anisotropically or pseudo-centering, both of which gives rise to weak and strong classes of reflections. This tends to have the opposite effect from twinning.

4.4.2. Anisotropy

The X-ray scattering power of an atom decreases as the scattering angle decreases, due to the finite size of an electron cloud. The larger the cloud, the more rapidly the scattering power falls off with scattering angle. The electron cloud of a vibrating atom, averaged over time, is larger than that of a similar atom at rest. The

individual atomic scattering contributions f should be corrected to account for this scattering behavior [17-19]:

$$f = f_0 \exp\left[-8\pi^2 \left\langle \boldsymbol{u}^2 \right\rangle \left(\frac{\sin^2 \theta}{\lambda^2}\right)\right]$$

where $\langle \boldsymbol{u}^2 \rangle$ is the mean-square amplitude of vibration of an atom, θ is the corresponding scattering angle and λ is the X-ray wavelength. The parameter $\boldsymbol{u}$ is called 'displacement' parameter and is usually reported in crystallography by $B = 8\pi^2 \left\langle \boldsymbol{u}^2 \right\rangle$ where B is the temperature factor and measures the displacement of an atom by thermal motion. This thermal vibration (in additional to conformational and lattice disorder) results in a falloff of scattering power by $\exp\left(-B\left(\sin\theta/\lambda\right)^2\right)$, leading to smearing of the electron density. When an electron cloud is uniformly smeared in all directions (inset Figure 4.5, center), $\boldsymbol{u}$ is isotropic. This parameter can be expanded into a 3 × 3 symmetric tensor to account for anisotropy in the smearing of an electron cloud [18, 19]:

$$\boldsymbol{U} = \begin{pmatrix} U^{11} & U^{12} & U^{13} \\ U^{12} & U^{22} & U^{23} \\ U^{13} & U^{23} & U^{33} \end{pmatrix}$$

The six independent components of the tensor are the anisotropic displacement parameters (ADPs) for an atom [18, 19]. The temperature factor B now becomes $B = 8\pi^2 \boldsymbol{U}$, thereby altering the falloff of the scattering power in an anisotropic manner.

If a crystal behaves isotropically, the same falloff will be expected in a plot of $\langle F \rangle$ vs. $2\sin\theta/\lambda$ in all three directions, where F is a structure factor and represents the total scattering form the unit cell and $2\sin\theta/\lambda$ equals (resolution (Å))$^{-1}$ [17]. Differences

in the falloff rate in these three directions will indicate anisotropy in the data. This plot was constructed for both native data sets collected for XenB [20] and shows no indication of high anisotropy in either dataset (Figure 4.5). The third dimension, c*, appears to deviate somewhat from dimensions 1 and 2 (a* and b*). This deviation is, on average, no larger than 83% with respect to a* and b*. Therefore, this dataset cannot be considered very anisotropic. In addition, anisotropy will introduce smearing in the electron density. This is also not observed in the maps for XenB. Instead, a defined 'shadow' of the electron density is observed at an approximate $z = 0.5$ translation

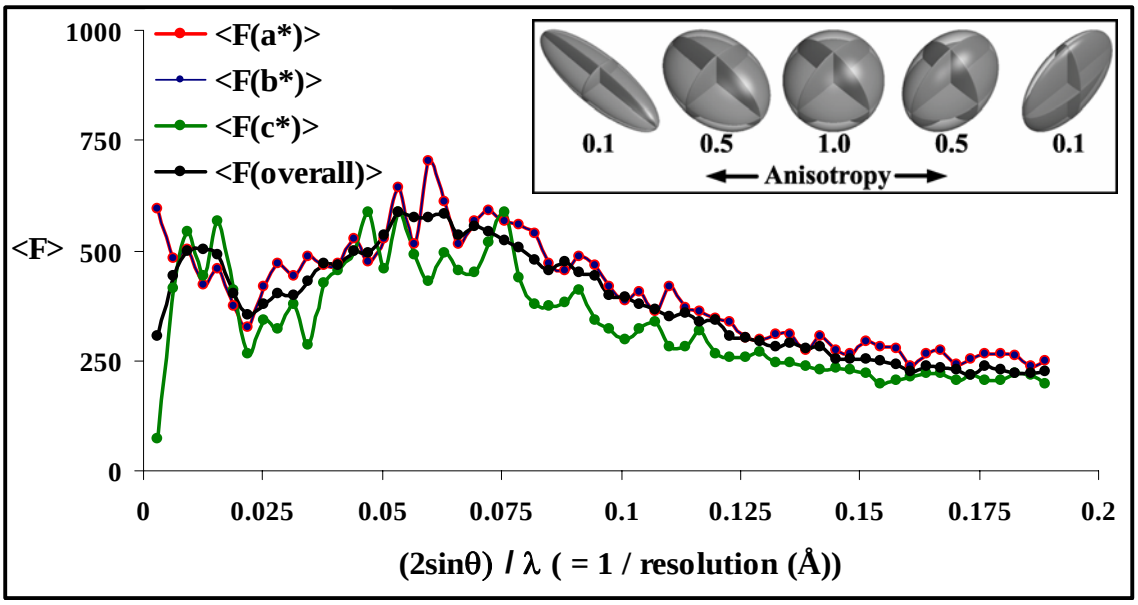

Figure 4.5: A plot of the $\langle F \rangle$ vs. $(2\sin\theta)/\lambda$ for all three dimension in the crystal of XenB [20]. The dimensions a*, b* and c* are drawn in red, blue and green resp. and the overall <*F*> values are drawn in black. The inset was reproduced from Merrit (1999) [19] and shows the effects of anisotropic displacement parameters (ADPs) on an electron cloud and represent shapes ranging from prolate 'cigar' (*left*) to oblate 'pancake' (*right*) with a perfect isotropic (sperical) example in the center.

4.4.3. Pseudo-centering

When non-crystallographic symmetry causes molecules to pack in the unit cell with an approximate crystallographic translation, the diffraction pattern may display pseudo-centering, with strong and weak reflections in an alternating arrangement. This can occur when a crystal starts out with true body centering that breaks down to pseudo centering due to radiation damage or if the crystal is pseudo centered all the time. In case of XenB, his could result in the true space group being body-centered ($I4_122$ or $I4_1$) instead of primitive ($P4_12_12$). Data can be inspected for pseudo-centering by calculating the average intensity ratios for reflections with $h+k$ odd/even, $h+l$ odd/even, $k+l$ odd/even and $h+k+l$ odd/even [21]. If, for instance, the $h+k$ odd/even ratio is small (< 0.5), this means that the $h+k$ odd reflections are 'systematically weak' and can indicate pseudo-C-face centering. This will also be true for $h+l$ (B face) and $k+l$ (A face). If all three ratios are low, this could indicate pseudo-F centering (all faces). If the ratio is low for $h+k+l$ odd/even, this could indicate pseudo-I centering (body) [21]. Ratios close to 1.0 indicate that there is no pseudo-centering.

Table 4.3 lists the average intensity for the odd and even reflections with $h+k$, $h+l$, $k+l$ and $h+k+l$ calculated for one native dataset of XenB [21] The odd to even ratios were calculated as for these sets of reflections. All ratios calculated for XenB were close to 1.0, meaning neither odd nor even reflections are systematically weak and leading to the conclusion that XenB shows no signs of pseudo-centering. The calculation was repeated for the second native data set collected for XenB with identical results. Neither native data set for XenB shows signs of pseudo-centering.

Table 4.3: The odd and even average intensities for reflections with $h+k$, $h+l$, $k+l$ and $h+k+l$ and their odd/even ratios [21].

		$\langle I \rangle$†	Ratio ($\langle I \rangle_{odd}/\langle I \rangle_{even}$) †
$\langle I_{(h+k)} \rangle$	odd	280693.562	1.008
	even	278538.969	
$\langle I_{(h+l)} \rangle$	odd	276385.125	0.977
	even	282847.781	
$\langle I_{(k+l)} \rangle$	odd	279387.031	0.998
	even	279842.406	
$\langle I_{(h+k+l)} \rangle$	odd	278023.656	0.989
	even	281204.562	

† All intensities were calculated using *xdlDATAMAN* from the Uppsala Software Factory (http://alpha2.bmc.uu.se/~gerard/manuals, [21])

4.4.4. Pseudo-symmetry

The existence of pseudo-symmetry in a crystal structure is indicative of a slightly distorted structure of higher symmetry [22]. Meaning, the apparent space group of a crystals as determined from autoindexing routines is a space group of higher symmetry than the actual space group of the crystal. When identical molecules are present in the asymmetric unit, they can be related to each other by some general transformation. This is referred to as non-crystallographic symmetry or local symmetry, since the symmetry operation relating the molecules is not defined by the space group. These non-crystallographic symmetry axes can occur at special positions in the unit cell, making them appear to be crystallographic. This can lead to confusion when trying to determine the actual space group (see chapter 2).

When a symmetry axis that exist in a crystal of a particular space group is actually non-crystallographic, it should not be considered by the space group and therefore a space group of lower symmetry should be selected that does not include this non-

crystallographic symmetry. This space group of lower symmetry is referred to as a maximal subgroup. A maximal non-isomorphic subgroup of a given space group is a space group of lower symmetry than the given group but contained within it and capable of separate existence as a space group. Consider now space group G and its subgroup H. It is always possible to represent their relationship by a chain of intermediate maximal subgroups Z [23]:

$$G > Z_1 > \ldots > Z_n > H$$

There are, in general, a number of space groups relating G to H. Figure 4.6A lists all possible maximal non-isomorphic subgroups for $P4_12_12$, the space group in which XenB is thought to have crystallized.

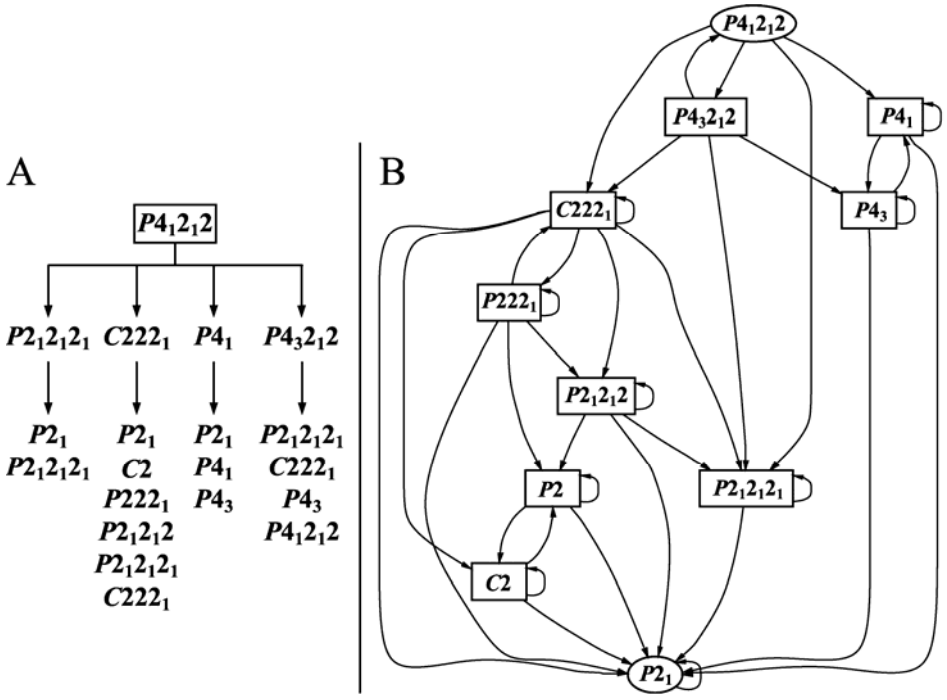

Figure 4.6: All possible subgroups for $P4_12_12$. **A,** The maximal non-isomorphic subgroups of $P4_12_12$ (*second row*) are listed along with their maximal non-isomorphic subgroups (*third row*). **B,** The relationships between all subgroups from $P4_12_12$ to $P2_1$ (http://www.cryst.ehu.es/cryst/subgroupgraph.html, [24].

Table 4.4 lists integrations statistics for one native dataset in various space groups along with some molecular replacement trials conducted in them. Re-integrating the data was necessary instead of reindexing the $P4_12_12$ solution obtained since space groups of lower symmetry are under investigation. Reindexing can only be used when a space group of higher symmetry is the objective.

Table 4.4: Integration statistics for XenB (*MOSFLM*, [25]) in various crystal systems and molecular replacement (*MOLREP*, [20]) and initial refinement statistics (*REFMAC*, [20]) for $P4_12_12$ and its subgroups.

	Primitive	Monoclinic		Orthorhombic		Tetragonal
	*P*1	*P*2	*C*2	*P*222	*C*222	*P*4 / *P*422
Resol. (Å)	28 – 2.3	28 – 2.3	27 – 2.3	28 – 2.3	28 – 2.3	28 – 2.3
Unit cell						
a (Å)	95.4	95.6	95.6	95.6	95.6	140.4
b (Å)	140.6	140.4	140.4	140.2	140.4	140.4
c (Å)	140.4	140.3	140.4	140.3	140.3	95.6
α (°)	89.9	90.0	90.0	90.0	90.0	90.0
β (°)	90.0	89.9	89.9	90.0	90.0	90.0
γ (°)	90.0	90.0	90.0	90.0	90.0	90.0
R_{sym} (%)†	0.072(0.266)	0.087(0.294)	0.088(0.306)	0.101(0.328)	0.101(0.323)	0.126(0.41)
$I/\sigma(I)$‡	7.0(2.7)	6.4(2.3)	4.7(2.3)	6.2(2.2)	6.3(2.2)	4.7(1.8)
Compl.(%)	59.4(40.7)	88.0(69.2)	84.6(63.3)	94.2(90.0)	94.5(91.0)	92.1(97.1)
Multiplicity	1.6(1.5)	2.1(1.7)	2.2(1.9)	3.9(2.6)	3.9(2.6)	7.4(4.9)

† R_{sym}(I) gives the average agreement between the independently measured intensities such as $\sum_h\sum_i|I_i - I|/\sum_h\sum_i I$, where I is the mean intensity of the i observations of reflection h. ‡ $I/\sigma(I)$ is the root-mean-square value of the intensity measurements divided by their estimated standard deviation.

Space group	No. molecules expected/found§	Molecular Replacement¶, 20–4.0Å, *R* (%) and corr. coefficient	Initial Refinements ₣, 28-2.3Å, *R* and R_{free} (%)
$P4_32_12$ (96)	2/1	*R* = 89.4, Corr. = 0.195	*R* = 54.3, R_{free} = 55.1
$P4_12_12$ (92)	2/2	*R* = 50.0, Corr. = 0.770	*R* = 32.1, R_{free} = 40.7
$P4_3$ (78)	4/4	*R* = 91.3, Corr. = 0.183	*R* = 65.2, R_{free} = 67.9
$P4_1$ (76)	4/4	*R* = 53.8, Corr. = 0.707	*R* = 36.9, R_{free} = 45.6
$C222_1$ (20)	4/4	*R* = 53.8, Corr. = 0.704	*R* = 35.8, R_{free} = 51.4
$P2_12_12_1$ (19)	4/4	*R* = 51.1, Corr. = 0.756	*R* = 31.4, R_{free} = 39.0
$P2_12_12$ (18)	4/2	*R* = 67.6, Corr. = 0.506	*R* = 45.9, R_{free} = 54.6
$P222_1$ (17)	4/2	*R* = 70.2, Corr. = 0.484	*R* = 48.3, R_{free} = 55.8
*C*2 (5)	8/3	*R* = 60.6, Corr. = 0.575	*R* = 63.0, R_{free} = 71.1
$P2_1$ (4)	8/3	*R* = 60.3, Corr. = 0.584	*R* = 63.9, R_{free} = 72.0
*P*1 (1)	16/4	*R* = 64.3, Corr. = 0.571	*R* = 45.8, R_{free} = 52.7

§ Number of molecules in the asymmetric unit was based on solvent content analysis [2]. ¶ Full length XenB (chain A) obtained from $P4_12_12$ analysis was used as the search model. ₣ Initial refinements included rigid body refinement to 3 Å where the full length chains were defined as domains and restrained refinement to 2.3 Å. No flavin molecules or water molecules had been included in these refinements.

During scaling routines of the data, multiple observations of reflections are scaled together and multiple observations are merged into an average intensity according to the requirements of the space group used. These requirements are not the same for different space groups, in particular, for space groups of lower symmetry where less requirements are present due to the lower symmetry. Reindexing from a spacegroup of higher symmetry to a spacegroup of lower symmetry will then result in output that wrongly reflects requirements of the higher symmetry. Although some molecular replacement solutions seem plausible, $P4_12_12$, $P4_1$ and $P2_12_12_1$, upon inspection of the resulting solution with its corresponding density maps, the 'shadows' are still present in the electron density maps and more often than not crystal packing violations occur. The same results were obtained for both native data sets of XenB. Therefore, it was concluded that the crystals of XenB do not show signs of pseudo symmetry.

4.5 Back to the Drawing Board to Solve the Crystal Structure of XenB

Solving the crystal structure of XenB resulted in an arduous task. Many crystallographic phenomena were explored (twinning, anisotropy, pseudo-centering and pseudo-symmetry) and many different space groups were tested (tetragonal, orthorhombic, monoclinic and primitive). No plausible answer for the crystal structure of XenB was found that refined to reasonable R and R_{free} values with no aberrant behavior in the electron density maps. It was decided to go back to the drawing board and investigate the autoindexing routine for XenB.

4.5.1. Autoindexing

Depending on the number of spots found and the particular diffraction images used, the autoindexing routing [25] will give differing results. Table 4.5 shows the results of the autoindexing that eventually led to the right answer for space group for solving the crystal structure of XenB. As can be observed from this table, the most logical selection in this list of options is the solution for a tetragonal space group (highlighted in blue) with $a = b$= ~139 Å and c = ~95 Å since this solution has the highest possible symmetry with the lowest possible penalty. Highlighted in red is the solution that has to be chosen to lead to the right answer for space group for XenB, face-centered orthorhombic (*C*222) with a = ~197 Å, b = ~198 Å and c = ~95 Å. After cell refinements and integration, the unit cell dimensions for this solutions remained $a = b$ = ~197 Å and c = ~95 Å (Table 4.6). In light of this result and past experience with these data sets, it was decided to also investigate primitive tetragonal space groups as well as primitive and face-centered orthorhombic, primitive and face-centered monoclinic and primitive space groups for this larger cell. Therefore, the solution for *C*222 obtained after integration was reindexed into $P4_12_12$.

For all possible space groups, primitive tetragonal space groups (*P*4/*P*422) as well as primitive and face-centered orthorhombic (*P*222 and *C*222), primitive and face-centered monoclinic (*P*2 and *C*2) and primitive (*P*1) molecular replacement calculations were carried out and are listed in Table 4.6. Also shown in this table are the integration statistics for these space groups.

Table 4.5: Autoindexing results for XenB using *MOSFLM* [25].

No.	Penalty	*a*	*b*	*c*	*α*	*β*	*γ*	Possible Space Group
28	406	139.51	312.30	95.24	89.9	90.1	116.3	$C222,C222_1$
27	406	139.51	312.30	95.24	90.1	90.1	63.7	$C2$
26	406	312.30	139.51	95.24	90.1	90.1	63.7	$C2$
25	381	95.24	197.26	219.49	89.8	64.4	89.9	$I222,I2_12_12_1$
24	379	294.60	95.24	197.26	89.9	131.8	71.3	$C2$
23	223	95.24	139.51	139.94	90.2	90.0	90.1	$P23,P2_13,P432,P4_232,P4_332,$ $P4_132$
22	223	169.12	169.25	218.91	106.4	73.8	108.4	$H3,H32$ (hexagonal settings $R3$ & $R32$)
21	222	168.72	169.25	219.84	106.5	73.6	108.6	$H3,H32$ (hexagonal settings $R3$ & $R32$)
20	220	168.72	169.12	139.94	90.2	90.2	68.6	$C222,C222_1$
19	220	95.24	139.51	139.94	90.2	90.0	90.1	$P4,P4_1,P4_2,P4_3,P422,P42_12,$ $P4_122,P4_12_12,P4_222,P4_22_12$ $P4_322,P4_32_12$
18	220	168.72	169.12	139.94	90.2	90.2	68.6	$C2$
17	219	169.12	168.72	139.94	89.8	90.2	111.4	$C2$
16	193	95.24	295.67	139.51	89.8	90.1	108.8	$C222,C222_1$
15	192	95.24	294.60	139.94	89.8	90.0	71.3	$C2$
14	192	95.24	295.62	139.51	89.9	90.1	71.2	$C2$
13	191	295.67	95.24	139.51	90.1	90.2	71.2	$C2$
12	190	95.24	294.60	139.94	89.8	90.0	108.7	$C222,C222_1$
11	189	294.60	95.24	139.94	90.0	90.2	71.3	$C2$
10	5	139.51	139.94	95.24	90.0	90.1	90.2	$P4,P4_1,P4_2,P4_3,P422,P42_12,$ $P4_122,P4_12_12,P4_222,P4_22_12$ $P4_322,P4_32_12$
9	3	197.94	197.26	95.24	90.1	90.1	90.2	$C2$
8	3	197.26	197.94	95.24	89.9	90.1	89.8	$C222,C222_1$
7	3	197.26	197.94	95.24	89.9	90.1	89.8	$C2$
6	2	95.24	139.94	139.51	90.2	90.1	90.0	$P2,P2_1$
5	2	95.24	139.51	139.94	90.2	90.0	90.1	$P2,P2_1$
4	2	95.24	139.51	139.94	90.2	90.0	90.1	$P222,P222_1,P2_12_12,P2_12_12_1$
3	1	139.51	95.24	139.94	90.0	90.2	90.1	$P2,P2_1$
2	0	95.24	139.51	139.94	89.8	90.0	89.9	$P1$
1	0	95.24	139.51	139.94	90.2	90.0	90.1	$P1$

4.5.2.Molecular Replacement

During data collection at the beamline, the smaller tetragonal cell was believed to be the space group of the XenB crystals and data was collected based on this choice. Since the actual unit cell of XenB turns out to be approximately 50 % larger in volume, with two dimensions of the unit cell increased by ~30%, the choices made for data collection were not optimal. During integration of the diffraction images in this larger

Table 4.6: Integration and molecular replacement statistics for various possible space groups for XenB in a larger unit cell with $a = b = \sim 198$ Å and $c = \sim 95$ Å.

	Primitive	Monoclinic		Orthorhombic		Tetragonal
	*P*1	*P*2	*C*2	*P*222	*C*222	*P*4 / *P*422
Resol. (Å)	28 – 2.3	28 – 2.3	27 – 2.3	28 – 2.3	28 – 2.3	28 – 2.3
Unit cell						
a (Å)	199.9	198.9	198.4	198.8	198.8	197.8
b (Å)	198.9	198.6	198.9	198.4	198.4	197.8
c (Å)	95.5	95.5	95.4	95.4	95.5	94.8
α (°)	89.9	90.0	90.0	90.0	90.0	90.0
β (°)	89.6	89.8	90.0	90.0	90.0	90.0
γ (°)	90.0	90.0	90.0	90.0	90.0	90.0
No. refl.	452482	456508	275420	577663	293145	305707
Unique refl.	402018	392496	94572	150815	62093	41716
R_{sym} (%)†	0.230(0.684)	0.140(0.552)	0.103(0.364)	0.214(0.774)	0.116(0.388)	0.128(0.442)
$I/\sigma(I)$‡	1.6(0.8)	3.7(1.0)	5.4(1.8)	2.9(0.9)	5.2(1.8)	4.8(1.6)
Compl.(%)	59.8(39.4)	58.1(38.4)	76.9(64.9)	89.2(82.7)	90.0(85.4)	48.6(47.6)
Multiplicity	1.6(1.5)	1.6(1.5)	2.4(1.8)	4.1(2.8)	4.1(2.8)	7.4(4.9)

† R_{sym}(I) gives the average agreement between the independently measured intensities such as $\sum_h\sum_i|I_i - I|/\sum_h\sum_i I$, where I is the mean intensity of the i observations of reflection h. ‡ $I/\sigma(I)$ is the root-mean-square value of the intensity measurements divided by their estimated standard deviation.

Space group	No. molecules expected/found§	Molecular Replacement¶ 20–4.0Å, *R* (%) and corr. coefficient	Initial Refinements ₣, 28-2.3Å, *R* and R_{free} (%)
$P4_32_12$ (96)	4/4	*R* = 56.2, Corr. = 0.614	
$P4_322$ (95)	4/2	*R* = 61.9, Corr. = 0.581	
$P4_22_12$ (94)	4/4	*R* = 65.3, Corr. = 0.556	
$P4_222$ (93)	4/4	*R* = 65.4, Corr. = 0.554	
$P4_12_12$ (92)	4/4	*R* = 37.3, Corr. = 0.849	*R* = 24.4, R_{free} = 29.5
$P4_122$ (91)	4/2	*R* = 67.3, Corr. = 0.511	
$P42_12$ (90)	4/2	*R* = 59.5, Corr. = 0.508	
*P*422 (89)	4/2	*R* = 66.6, Corr. = 0.512	
$P4_3$ (78)	8/6	*R* = 53.3, Corr. = 0.656	
$P4_2$ (77)	8/6	*R* = 58.8, Corr. = 0.595	
$P4_1$ (76)	8/8	*R* = 36.4, Corr. = 0.847	*R* = 24.4, R_{free} = 30.3
*P*4 (75)	8/6	*R* = 59.1, Corr. = 0.591	
*C*222 (21)	4/2	*R* = 91.8, Corr. = 0.147	
$C222_1$ (20)	4/4	*R* = 53.8, Corr. = 0.704	
$P2_12_12_1$ (19)	8/8	*R* = 36.4, Corr. = 0.849	*R* = 26.9, R_{free} = 34.0
$P2_12_12$ (18)	8/8	*R* = 85.5, Corr. = 0.267	
$P222_1$ (17)	8/8	*R* = 38.2, Corr. = 0.0.831	
*P*222 (16)	8/4	*R* = 89.6, Corr. = 0.406	
*C*2 (5)	8/3	*R* = 60.6, Corr. = 0.575	
$P2_1$ (4)	16/4	*R* = 59.3, Corr. = 0.560	
*P*2 (3)	16/4	*R* = 60.5, Corr. = 0.573	
*P*1 (1)	32/30	*R* = 40.4, Corr. = 0.827	

§ Number of molecules in the asymmetric unit was based on solvent content analysis [2]. ¶ Full length XenB (chain A) obtained from $P4_12_12$ analysis was used as the search model. ₣ Initial refinements included rigid body refinement to 3 Å where the full length chains were defined as domains and restrained refinement to 2.3 Å. No flavin molecules or water molecules had been included in these refinements.

cell, many reflections were now rejected due to overlaps. This resulted in much lower completeness for the integrations.

As can be judged based in the results in Table 4.6, a primitive tetragonal space group, $P4_12_12$ or $P4_1$ (highlighted in red and yellow respectively), or a primitive orthorhombic space group, $P2_12_12_1$ (highlighted in yellow), have the best molecular replacement results. This is the same result as obtained for XenB indexed in the smaller cell. However, upon inspection of the crystal packing and the electron density maps, no violations and no 'shadows' were observed. After initial rigid body and restrained refinement, the solutions obtained for $P4_12_12$, $P4_1$ and $P2_12_12_1$ were of similar quality in terms of their R and R_{free} values (Table 4.6).

Table 4.7: Final refinement statistics for both native data sets for XenB in $P4_12_12$.

Dataset indexed in $P4_12_12$	Native 1	Native 2
Resolution range (Å)	28-2.3	31-2.3
Unit cell parameters		
$a = b$ (Å)	198.6	197.8
c (Å)	95.5	94.8
Number of reflections	37.426	33153
R (%)	20.9	18.4
R_{free} (%) (10 % data)	28.6	27.1
Number of non-H atoms	11364	11603
Number of protein residues	1392	1392
Number of water molecules	640	879
Average B values (Å^2)		
Protein	25.2	23.0
FMN	21.7	20.2
water	23.9	22.6
R.m.s.d from ideal geometry		
Bond lengths (Å)	0.012	0.010
Bond angles (°)	1.5	1.3

Therefore, the right space group is $P4_12_12$ with $a = b = \sim198$ Å and $c = \sim95$ Å since this is the solution with the highest possible symmetry. The same results were obtained for both native data sets.

4.5.3.Refinement of XenB in a Larger Primitive Tetragonal Space Group $P4_12_12$

Table 4.7 shows the final refinement statistics for both native XenB data sets The final model for native XenB had an R of 18.4 % and an R_{free} of 27.1 % with data between 31 – 2.3 Å resolution. The final rounds of refinement using *REFMAC* [20] were done using non-crystallographic symmetry (ncs) averaging over the four chains present in the asymmetric unit. The main chain and side chain ncs-averaging constraints were set to medium and loose respectively. Since the resolution limit of either native data set does not exceed 2.3 Å, bulk solvent scaling was carried out using the Babinet principle [26] where bulk solvent correction is based on a more reasonable and constant value (B = 50 Å^2). In Babinet's principle it is assumed that the structure factors of the bulk solvent electron density are directly proportional to the structure factors of the protein electron density with strictly opposite phases and is only true at resolutions lower than ~15 Å, using observed protein phases to estimate phase differences.

4.5.4.Comparison of the Two Tetragonal Space Groups of XenB

XenB has been 'solved' in two different space groups, a 'right' or 'large' one and a 'wrong' or 'small' one. The large space group for XenB is primitive tetragonal $P4_12_12$ with $a = b = 197.8$ Å and $c = 94.8$ Å and the small space group is also primitive

tetragonal $P4_12_12$ with $a = b = 139.9$ Å and $c = 94.8$ Å. When comparing the overall crystal packing of both primitive tetragonal unit cells found for XenB they seem identical at first sight (Figure 4.7A). There are, however, differences in the *z*-coordinate of some molecules (Figure 4.7B). The unit cell and therefore the asymmetric unit is different for these space groups not only in size, but also orientation (Figure 4.8).

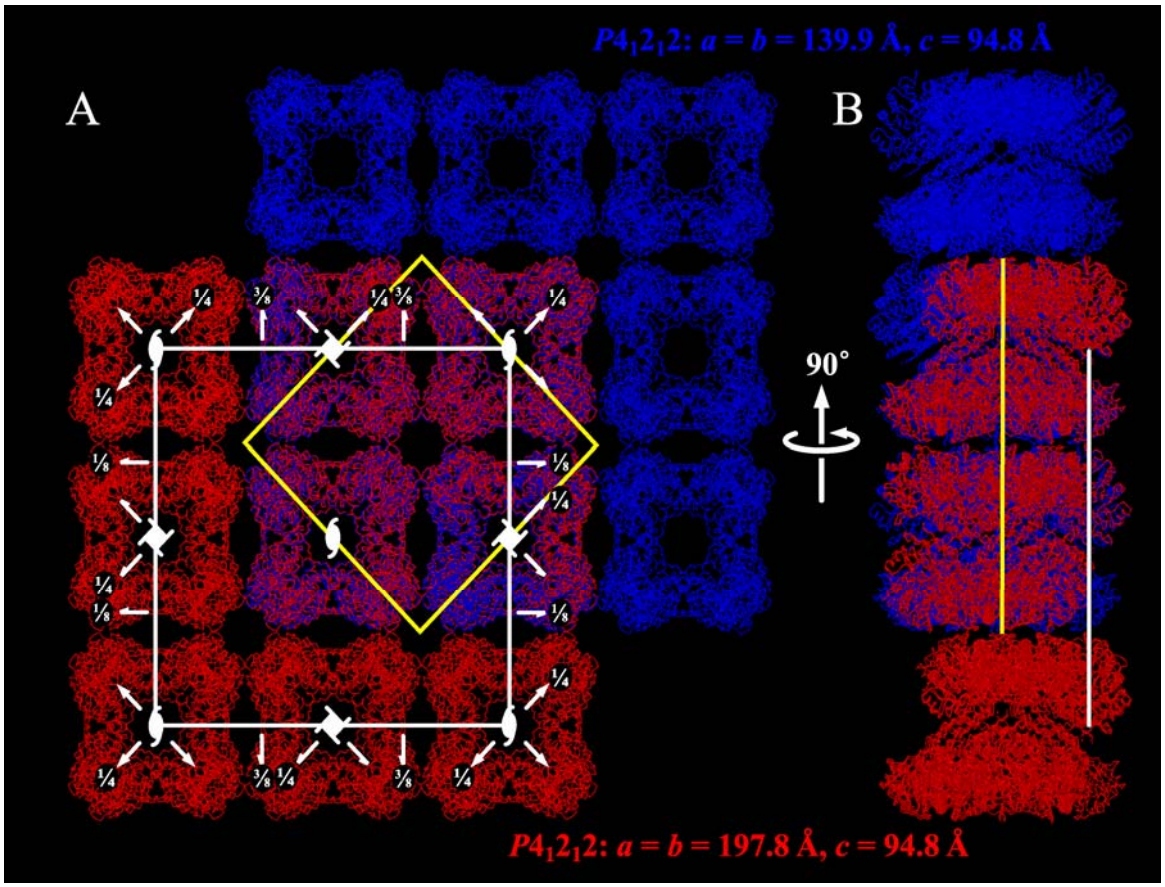

Figure 4.7: An overlay of the 'right' and 'wrong' primitive tetragonal space groups of XenB viewed in the *xy*-plane. **A,** Space group $P4_12_12$ with $a = b = 197.8$ Å and $c = 94.8$ Å (*'right'* or *'large'* space group) has all molecules drawn as a C_α-trace colored in red with the unit cell drawn in white, including the symmetry elements. A total of 2¼ unit cells are shown for this space group. Space group $P4_12_12$ with $a = b = 139.9$ Å and $c = 94.8$ Å (*'wrong'* or *'small'* space group) has all molecules drawn as a C_α-trace colored in blue with the unit cell drawn in yellow. A total of 4½ unit cells are shown for this space group. **B,** A 90° rotated view of (A).

First, the smaller unit cell is 50% smaller in volume, with its asymmetric unit only containing 50% of the content of the asymmetric unit from the larger cell. Secondly, the unit cells are rotated 45° in the *xy*-plane with respect to each other (Figure 4.7). Moreover, the larger space group requires four molecules in the asymmetric unit [2] based on solvent content analysis (V_M = 3.1 Å^3 Da^{-1}, 60% solvent content), but the smaller space goup will only allow for two molcules (V_M = 3.2 Å^3 Da^{-1}, 61% solvent content). Upon examination of the asymmetric unit of the larger space group, it is evident that no non-crystallographic symmetry is present relating these four molecules to each other (Figure 4.8A). This makes it impossible for the smaller space group to accurately describe the crystal packing of these XenB crystals with just two molecules. When comparing the orientation of the molecules in the asymmetric unit of the larger cell

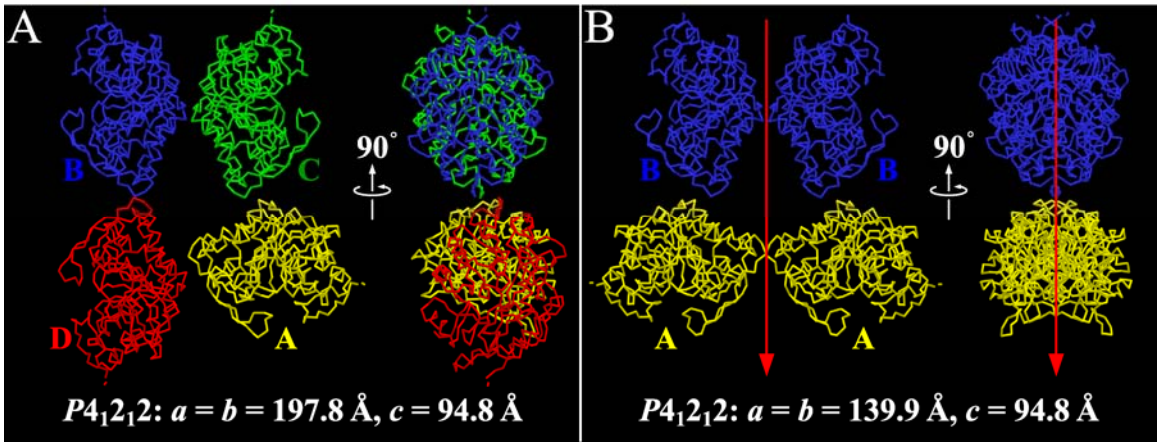

Figure 4.8: The asymmetric unit of the large and small space groups of XenB viewed in the *xy*-plane (*left*) and the *yz*-plane (*right*). **A,** The large space group has four molecules in the asymmetric unit (A = yellow, B = blue, C = green and D = red) with no non-crystallographic symmetry present to relate the four molecules in the asymmetric unit. **B,** The small space group has two molecules in the asymmetric unit (A = yellow and B = blue). The additional two molecules (*left*) stem from an adjoining asymmetric unit to reflect the asymmetric unit of the large space group. Clearly, these pairs of AB monomers can be related by two-fold symmetry (crystallographic).

with the equivalent molecules in the smaller cell, it should also be noticed that that one of the molecules in the asymmetric unit of the larger cell (D) has an orientation that disrupts regular packing in this cell. A 45° rotation in the *xy*-plane would make the packing in this asymmetric unit identical to the corresponding packing in the smaller cell and would then allow for non-crystallographic symmetry to relate A and C with B and D (Figure 4.8B). These non- crystallographic symmetry axes would then be located at special positions (¼ , *y* , ½) and (¾ , *y* , ½) and would alter the space group from this larger cell to a smaller cell that requires two molecules in the asymmetric unit.

How do these two space groups account for the observation of 'shadows' in the smaller cell? Figure 4.9 illustrates the occurrence of this observation in the smaller cell due to the space group symmetry of the larger cell. The asymmetric units of the larger (red) and smaller (blue) cells are shown in the top left of Figure 4.9. These molecules align exactly with each other with no deviation in their *z*-coordinates. Going down in Figure 4.9 represents the addition of an asymmetric unit form an adjoining small cell (green). One of these additional molecules will then reflect the difference of a 45° rotation between chain D in the larger cell and chain A in the smaller cell (Figure 4.8). This molecule now overlaps with a chain in the larger cell in an orientation identical to what is observed for chain A and its 'shadow' in the smaller cell (middle of Figure 4.9), resulting in a 'ghost' image of this chain in the smaller cell created solely by the crystal symmetry of the larger cell. Exactly the same happens with a symmetry mate (½-*y*, ½+*x*, ¼+*z*) of the asymmetric unit of the smaller cell (Figure 4.9, top right, green molecules) with a symmetry mate (½+*x*, ½-*y*, ¾-*z*) of the asymmetric unit of the larger cell (Figure 4.9, bottom right, yellow molecules). This larger cell now creates a 'ghost' on top of the

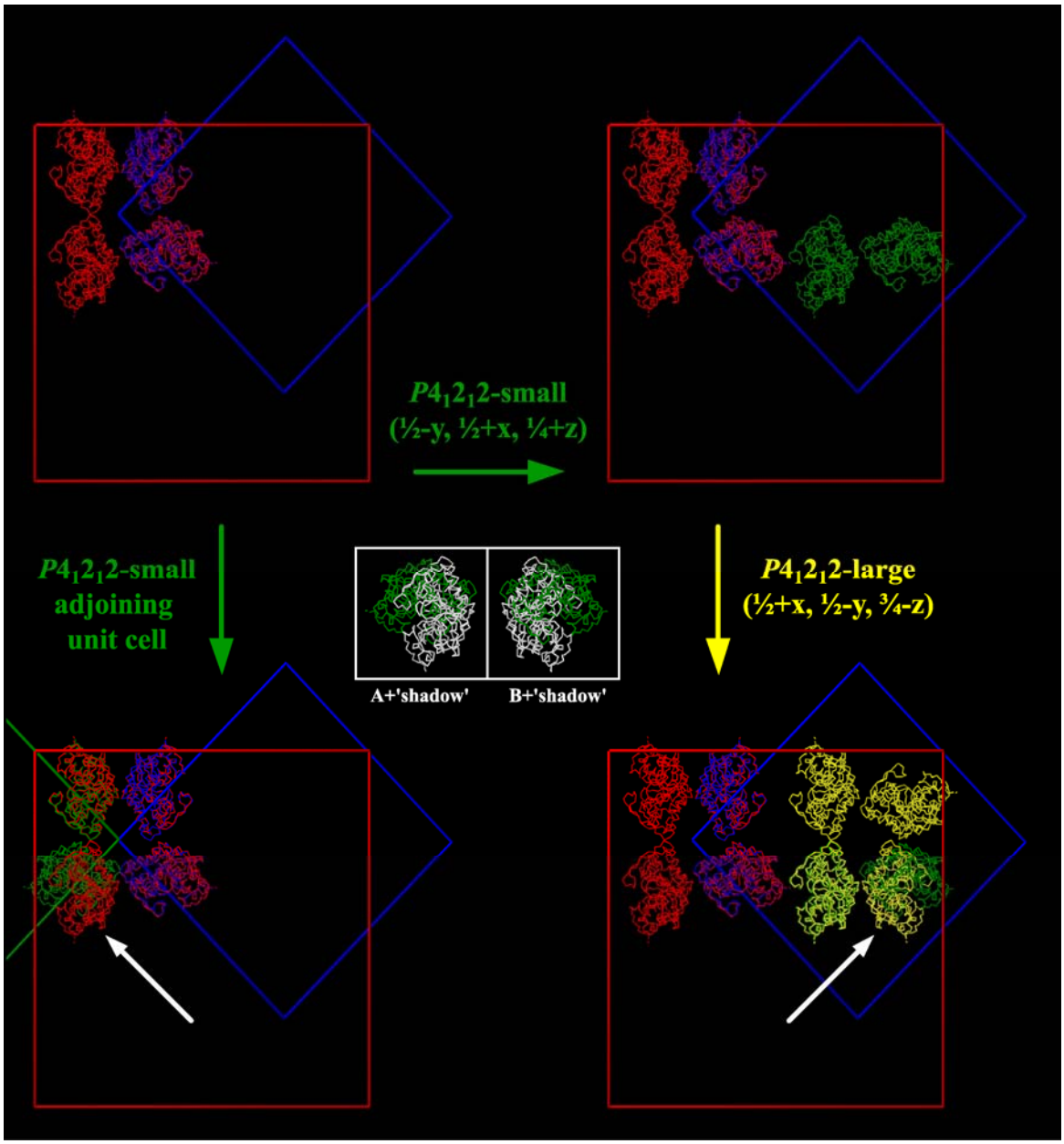

Figure 4.9: The appearance of 'shadows' in the $P4_12_12$ smaller space group of XenB as a consequence of the $P4_12_12$ symmetry of the larger cell illustrated in the *xy*-plane. Shown in red are the four molecules in the asymmetric unit of the larger cell overlayed with the asymmetric unit of the smaller cell in blue (*top left*) with their corresponding unit cells drawn as red and blue boxes, respectively. Addition of an adjoining asymmetric unit of the smaller cell (*bottom left*) and a symmetry mate (*top right*) are shown in green with the additional unit cell drawn as a green box. The addition of a symmetry mate of the larger asymmetric unit (*bottom right*) is shown in yellow. In the middle is shown the orientation of the 'shadows' [27] with respect to chain A and B (green) in the smaller cell. Sites of 'shadows' are indicated with white arrows. No difference in *z*-coordinate exist in the view of this figure. All molecules shown exist in the same section of the *xy*-plane.

B chain of the smaller cell identical to what is observed for the B chain and its 'shadow' in the smaller cell (middle of Figure 4.9).

Figure 4.10 illustrates the behavior resulting in the observation of 'shadows' for the entire cell of the larger space group. The sites of 'shadow' formation are indicated with green arrows. The view on the left represents the *xy*-plane with all molecules drawn in the same section of this plane. These molecules only represent 50% of the unit cell content. Noticably, only four occurrences of 'shadows' are observed in this smaller unit cell. This is 25% of the its entire content and explains the much lower σ-levels of the mystery density that results from this behavior.

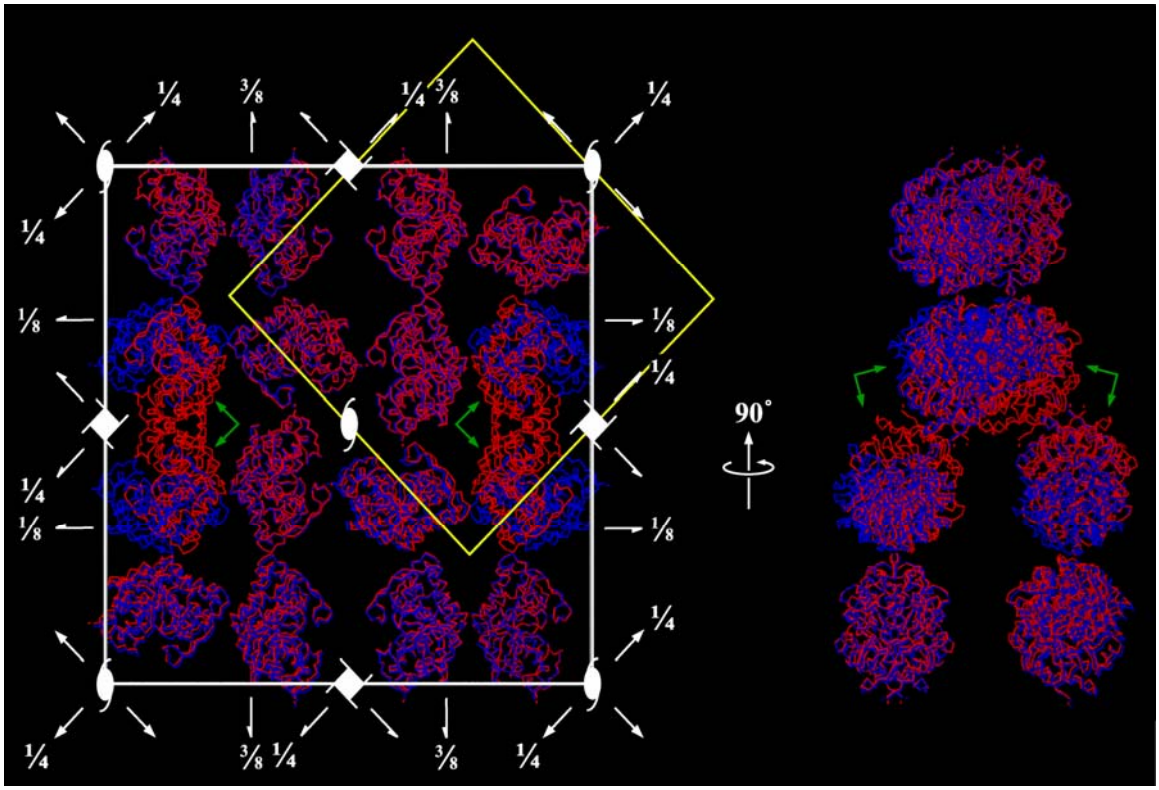

Figure 4.10: The appearance of 'shadows' (green arrows) in the smaller space group (blue molecules) illustrated for the entire cell of the larger space group (red molecules) with their unit cells drawn as yellow and white (with symmetry elements) boxes, respectively, viewed from the *xy*-plane (*left*) and *yz*-plane (*right*).

4.6. Conclusion

Although initial data analysis did result in a complete three-dimensional model for XenB, the refinements could not be completed satisfactorily. Unusual mystery density was observed in the electron density maps that appeared to be 'shadows' of additional monomers overlapping with the models already present. This behavior was the result of assignment of a wrong space group. The actual space group of XenB turned out to be 50% larger than originally anticipated, with four instead of two molecules in the asymmetric unit. Also, the unit cells were rotated with respect to each other by 45º. The crystal packing for both space groups is nearly identical with the only differences occurring in the *z*-dimension. The observation of 'shadows' in the smaller space group resulted form the space group symmetry of the actual, larger space group making this a unique example of pseudo-symmetry.

4.7. References

1. Orville, A.M., L. Manning, D.S. Blehert, B.G. Fox, and G.H. Chambliss, *Crystallization and preliminary analysis of xenobiotic reductase B from Pseudomonas fluorescens I-C.* Acta. Cryst., 2004. **D60**(Pt 7): p. 1289-1291.

2. Matthews, B.W., *Solvent content of protein crystals.* J. Mol. Biol., 1968. **33**(2): p. 491-497.

3. Kantardjieff, K.A. and B. Rupp, *Matthews coefficient probabilities: Improved estimates for unit cell contents of proteins, DNA, and protein-nucleic acid complex crystals.* Protein Sci., 2003. **12**(9): p. 1865-1871.

4. Barna, T., H.L. Messiha, C. Petosa, N.C. Bruce, N.S. Scrutton, and P.C. Moody, *Crystal structure of bacterial morphinone reductase and properties of the C191A mutant enzyme.* J. Biol. Chem., 2002. **277**(34): p. 30976-30983.

5. Brändén, C.I. and A.T. Jones, *Between objectivity and subjectivity.* Nature, 1990. **343**(6260): p. 687-689.

6. Kleywegt, G.J. and A.T. Brünger, *Checking your imagination: applications of the free R value.* Structure, 1996. **4**(8): p. 897-904.

7. Brünger, A.T., *Free R value: a novel statistical quantity for assessing the accuracy of crystal structures.* Nature, 1992. **355**(6359): p. 472-475.

8. Brünger, A.T., *Assessment of phase accuracy by cross validation: the free R value. Methods and applications.* Acta Cryst., 1993. **D49**(Pt 1): p. 24-36.

9. Brünger, A.T., *Free R value: Cross-validation in crystallography.* Methods Enzymol., 1997. **277**: p. 366-396.

10. Tickle, I.J., R.A. Laskowski, and D.S. Moss, *Rfree and the rfree ratio. I. Derivation of expected values of cross-validation residuals used in macromolecular least-squares refinement.* Acta Cryst., 1998. **54**(Pt 4): p. 547-557.

11. Yeates, T.O., *Detecting and Overcoming Crystal Twinning.* Methods Enzymol., 1997. **276**: p. 344-358.

12. Donnay, G. and J.D.H. Donnay, *Classification of Triperiodic Twins.* Can. Mineral., 1974. **12**: p. 422-425.

13. Buerger, M.J., *Crystal-Structure Analysis*. 1960, New York: John Wiley & Sons.

14. Friedel, G., *Leçons de Cristallographie*. 1926, Berger-Levrault: Paris.

15. Cahn, R.W., *Twinned Crystals.* Adv. Phys., 1954. **3**: p. 363-445.

16. Wilson, A.J.C., *The probability distribution of X-ray intensities.* Acta Cryst., 1949. **2**: p. 318-321.

17. French, S. and K. Wilson, *On the Treatment of Negative Intensity Observations.* Acta Cryst., 1978. **A34**(Pt 4): p. 517-525.

18. Merrit, E.A., *Comparing anisotropic displacement parameters in protein structures.* Acta Cryst., 1999. **D55**(Pt 12): p. 1997-2004.

19. Merrit, E.A., *Expanding the model: anisotropic displacement parameters in protein structure refinement.* Acta Cryst., 1999. **D55**(Pt 6): p. 1109-1117.

20. Collaborative Computational Project, N., *The CCP4 Suite: Programs for Protein Crystallography.* Acta Cryst., 1994. **D50**(Pt 5): p. 760-763.

21. Kleywegt, G.J. and A.T. Jones, *xdlMAPMAN and xdlDATAMAN - Programs for Reformatting, Analysis and Manipulation of Biomacromolecular Electron-Density Maps and Reflection Data Sets.* Acta Cryst., 1996. **D52**(Pt 5): p. 826-828.

22. Igartua, J.M., *Systematic search of materials with high-temperature structural phase transitions: Application to space group $P2_12_12_1$.* Phys. Rev., 1996. **54**(18): p. 12744-12752.

23. E. Kroumova, E., M.I. Aroyo, J.M. Perez Mato, A. Kirov, C. Capillas, S. Ivantchev, and H. Wondratschek, *Bilbao Crystallographic Server: useful databases and tools for phase transitions studies.* Phase Transitions, 2003. **76**(1-2): p. 155-170.

24. Ivantchev, S., E. Kroumova, G. Madariaga, P.-M.J. M., and M.I. Aroyo, *SUBGROUPGRAPH - a computer program for analysis of group-subgroup relations between space groups.* J. Appl. Cryst., 2000. **33**(Pt 4): p. 1190-1191.

25. Powell, H.R., *The Rossmann Fourier autoindexing algorithm in MOSFLM.* Acta Cryst., 1999. **D55**(Pt 10): p. 1690-1695.

26. Tronrud, D.E., *Knowledge-Based I-Factor Restraints for the Refinement of Proteins.* J. Appl. Cryst., 1996. **29**(Pt 2): p. 100-104.

27. Nelson, K.E., C. Weinel, I.T. Paulsen, R.J. Dodson, H. Hilbert, V.A. Martins dos Santos, D.E. Fouts, S.R. Gill, M. Pop, M. Holmes, L. Brinkac, M. Beanan, R.T. DeBoy, S. Daugherty, J. Kolonay, R. Madupu, W. Nelson, O. White, J. Peterson, H. Khouri, I. Hance, P. Chris Lee, E. Holtzapple, D. Scanlan, K. Tran, A. Moazzez, T. Utterback, M. Rizzo, K. Lee, D. Kosack, D. Moestl, H. Wedler, J. Lauber, D. Stjepandic, J. Hoheisel, M. Straetz, S. Heim, C. Kiewitz, J. Eisen, K.N. Timmis, A. Dusterhoft, B. Tummler, and C.M. Fraser, *Complete genome sequence and comparative analysis of the metabolically versatile Pseudomonas putida KT2440.* Environ. Microbiol., 2002. **4**(12): p. 799-808.

5. CRYSTAL STRUCTURES OF XENOBIOTIC REDUCTASES A AND B FROM *PSEUDOMONAS PUTIDA* II-B AND *PSEUDOMONAS FLUORESCENS* I-C: TWO FLAVOENZYMES THAT ELIMINATE NITRITE FROM NITROGLYCERIN

5.1 Abstract

Pseudomonas putida II-B and *Pseudomonas fluorescens* I-C were isolated from the contaminated soil at the Badger Army Ammunition Plant in Baraboo, Wisconsin, USA. The enrichment strategy selected for bacteria with an ability to obtain all nitrogen required for growth from nitroglycerin. The FMN-dependent enzymes partly responsible for the phenotype have been named xenobiotic reductase A (XenA) and xenobiotic reductase B (XenB) from *P. putida* II-B and *P. fluorescens* I-C, respectively. They both catalyze the NADPH-dependent nitrite elimination from nitroglycerin or the reduction of trinitrotoluene (TNT) to yield a variety of products. Here we report the crystal structures of XenA and XenB to 1.6 Å and 2.3 Å resolution, respectively. Both proteins fold as

---

Formatted from: **Manning, L.**, Blehert, D.S., Chambliss, G.H., Fox, B.G. & Orville, A.M. "Crystal Structures of Xenobiotic Reductases A and B from *Pseudomonas putida* II-B and *Pseudomonas fluorescens* I-C: Two Flavoenzymes that Eliminate Nitrite from Nitroglycerin Crystallization and preliminary analysis of xenobiotic reductase B and ligand complexes from *Pseudomonas fluorescens* I-C" *In preparation for Biochemistry*

$(\beta/\alpha)_8$ barrels as anticipated from previous amino acid sequence homology analysis. However, the structures show that XenA is a C-terminal, domain-swapped dimer. The point of closest contact between the two subunits in XenA occurs at the exterior face of α-helix 1 and includes residues Val39 and Ser43. The analogous XenB residues in α-helix 1 are Glu40 and Gln44, and consequently, it is a monomer. As a result of the C-terminal domain-swap in XenA, Trp357 from one subunit packs against the dimethylbenzene portion of the FMN in the other subunit. In contrast, each monomer of XenB places Phe334 and Tyr335 from the same subunit against the dimethylbenzene ring of the FMN. Comparisons of the active sites of XenA, XenB and homologs reveal a number of key differences that likely govern the regiospecific reactions of XenA and XenB with nitroglycerin and TNT. The following paper describes several crystal structures of XenA ligand complexes and docking experiments of nitroglycerin and TNT with reduced XenA and XenB that correlate well with previous functional studies [1-3].

5.2 Introduction

Nitroglycerin is currently one of the 100 most frequently prescribed drugs [4-7]. Indeed, the use of nitroglycerin for the treatment of angina pectoris was first reported in 1879 just 33 years after it was invented [8]. However, the precise mechanism of bioactivation of nitroglycerin has been difficult to define [4-7, 9-11]. It has been proposed to result from both oxidative and reductive processes. For example, enzymes such as cytochrome P450, cytochrome P450 reductase, glutathione S-transferases or xanthine oxidoreductase all yield a range of products including nitrite, 1,2- and 1,3-

dinitroglycerols, and mononitroglycerols [6, 12-22]. Mammalian transformation of nitroglycerin by vascular smooth muscle cells is known to yield 1,2-dinitroglycerol, nitrite, and eventually nitric oxide. Physiologically, nitric oxide is normally derived from arginine by nitric oxide synthase and has many important physiological functions, including vasodilation [23-26]. Chen *et al.* demonstrated in 2002 that a novel activity of mammalian mitochondrial aldehyde dehydrogenase (mt-ADH) catalyzes the regiospecific, reductive elimination of nitrite from nitroglycerin to yield 1,2-dinitroglycerol [27]. The nitrite appears to be converted into nitric oxide by other mitochondrial enzymes, which then activates guanylate cyclase-dependent signal cascades. Furthermore, Chen *et al.* suggested that bioactivation of nitroglycerin by mt-ADH i) involves active site cysteine residues to achieve catalysis, ii) may contain a covalent S-nitrosothiol as a key reaction intermediate, iii) likely forms an intramolecular disulfide bond, and iv) the reaction requires a source of two electron reducing equivalents. Thus, more than a century after the physiological effects of nitroglycerin were first observed, at least one rather detailed description for its regiospecific bioactivation has been proposed. It is the consequence of a novel activity elicited from an essential metabolic enzyme. However, most of the other proposed enzymatic transformations also yield intermediates that can generate nitric oxide. Moreover, the biotransformation of nitroglycerin also differs in dose-dependent, tissue, cell and subcellular specific manners to yield a range of products. Therefore, the biotransformation of nitroglycerin is a complex process, which has yet to be fully characterized.

Organic nitrochemicals from man-made sources have been distributed throughout the biosphere in vast excesses over naturally occurring examples. This includes many explosive compounds such as 2,4,6-trinitrotoluene (TNT) and nitroglycerin, which have no known naturally occurring analogs and are therefore considered xenobiotic. Nevertheless, microbes have been isolated from contaminated soil at munitions manufacturing sites that metabolize explosives as sources of nitrogen and/or carbon [1-3]. Xenobiotic reductase A (XenA) from *Pseudomonas putida* II-B and xenobiotic reductase B (XenB) from *Pseudomonas fluorescens* I-C were purified from bacterial strains isolated from the World War II era, Badger munitions manufacturing plant in Baraboo, WI. These strains were identified because they not only tolerate concentrations of nitroglycerin that are toxic to nearly all other organisms, but they can also obtain all their nitrogen required for growth [2]. The enzymes responsible for this process, XenA and XenB, catalyze the NADPH-dependent nitrite elimination from nitroglycerin via a ping-pong kinetic scheme. However, the organic product of the oxidative half-reaction from XenA is 1,2-dinitroglycerol, whereas from XenB it is 1,3-dinitroglycerol. Therefore, the two enzymes use the same substrates for the reductive and oxidative half-reactions (NADPH and nitroglycerin, respectively), but the latter reaction yields different products. XenA exhibits selectivity for removal of a terminal nitro group of nitroglycerin, whereas XenB is selective for an internal nitro group. XenB and XenA also reduce 2,4,6-trinitrotoluene (TNT) to yield a variety of products, although the reactivity by XenB is more robust than that of XenA [2, 3]. Metronidazole is also reduced *in vitro* and *in vivo* by XenA and XenB as evidenced by the observation that *E. coli* DH5α transformed and expressing the genes for either XenA or XenB die in the presence of metronidazole

(unpublished data). Since the *E. coli* is not normally sensitive to metronidazole, the reactivity of XenA and XenB is probably analogous to that of pathogens that are susceptible to this class of pro-drug [28-30].

Amino acid sequence analysis of XenA and XenB indicate that they are both very likely members of the class I $(\beta/\alpha)_8$ barrel family of FMN-containing flavoenzymes [1, 2, 31]. The prototypical member of the family is old yellow enzyme (OYE) [32, 33]. Other structurally characterized members include pentaerythritol tetranitrate reductase (PETNR) [34], morphinone reductase (MorR) [35], 12-oxophytodienoate reductase isoforms 1 (OPR-1) [36] and 3 [37] (OPR-3), 2,4-dienoyl-CoA reductase (DCR) [38], the isoforms of trimethylamine dehydrogenase (TMADH) [2, 3, 39, 40] and YqjM, an OYE homolog from *Bacillus subtilis* [41, 42]. With the exception of TMADH, all these homologs use a ping-pong kinetic mechanism and NAD(P)H in the reductive half-reaction. The reduced enzymes are typically relatively stable under aerobic conditions, but as a group they exhibit remarkable substrate diversity in the oxidative half-reactions. Therefore, on the one hand, this family of enzymes binds identical substrates during the reductive half reactions, but on the other hand, they discriminate between diverse substrate molecules to complete the oxidative half-reactions. Moreover, XenA and XenB are unique among the family, since they also yield different reaction products in their oxidative half-reactions from identical substrates. Here we report the crystal structures of XenA and XenB from *Pseudomonas putida* II-B and *Pseudomonas fluorescens* I-C. Theses structures reveal active site binding sites of similar size, but with different distributions of hydrogen bond donors and acceptors, and different electrostatic surface features. An important feature is the observation that XenA is a functional dimer with a

domain-swapped C-terminal region that comprises a portion of the active site. In contrast, XenB is a functional monomer with similar, but distinctly different interactions within the active site compared to XenA.

5.3 Material and Methods

5.3.1. Protein Expression and Purification

XenA from *Pseudomonas putida* II-B and XenB from *Pseudomonas fluorescens* I-C were purified and crystallized as previously reported [1, 2, 43, 44].

5.3.2. Crystal Structure Determination

The structure of oxidized XenA was solved with MAD phasing techniques with Se-Met enriched crystals as previously described and briefly summarized here [43]. The space group is $P2_12_12$ with a = 84 Å, b = 157 Å, c = 57 Å. Nine selenium sites were located with *SOLVE* [45] using diffraction data from four X-ray wavelengths with data between 2.5 and 30 Å resolution collected at 100 K. The sites were refined to convergence in *SHARP* [46] (Table 5.1). The Se-Met experimental phases between 30 and 2.5 Å resolution were appended to a 1.65 Å resolution dataset for oxidized XenA collected at 283 K. Phase extension and solvent flattening to 1.65 Å was performed with the *CCP4* suite of programs [47].

The refined crystal structure for XenB is in space group $P4_12_12$ with unit cell dimensions of $a = b$ = 198 Å and c = 95 Å and four XenB molecules in the asymmetric unit. This assignment differs from our previous characterization [44] of the space group

as $P4_12_12$, with unit-cell parameters $a = b = 140$ Å, $c = 95.6$ Å because this smaller unit cell, which contained two XenB molecules per asymmetric unit, did not refine to an acceptable *R*-free value. The structure of native XenB was solved by molecular replacement in *MOLREP* [47] using a search model derived from native morphinone reductase (PDB code 1gwj [35]). All the solvent molecules and the FMN were removed, the B-factors were set to the Wilson B (typically about 28 $Å^2$) and all non-identical residues were either truncated to alanines or deleted from the search model.

Table 5.1: Data Collection and Phasing Statistics for native XenA and XenB

	Native XenA	SeMet-enriched oxidized XenA				Native XenB
		Inflection (f')	Peak (f'')	Low-energy remote	High-energy remote	
Temperature (K)	283	100	100	100	100	100
Wavelength (Å)	0.98	0.979764	0.979609	1.06883	0.925256	0.9778
Resolution range (Å)	35 – 1.65	33 – 2.5	35 – 2.5	37 – 2.5	31 – 3.0	31 – 2.3
Total Obs. / Unique Obs.	312545 / 94132	171180 / 24191	208107 / 24297	194077 / 23455	88225 / 13929	226336 / 36997
R_{sym} [a,b]	0.051 (0.39)	0.128 (0.497)	0.121 (0.442)	0.105 (0.369)	0.173 (0.478)	0.098 (0.339)
I/σ(I) [c]	17.5 (4.5)	5.4 (1.5)	5.7 (1.7)	6.5 (2.0)	4.1 (1.6)	5.9 (2.2)
Compl. (%) [a]	98.9 (98.6)	91.1 (92.0)	91.5 (93.2)	88.4 67.8)	89.8 (92.4)	43.6 (27.0)
R_{cullis} centric (iso) [d]	---	0.50	0.47	---	0.90	---
R_{cullis} acentric (iso/ano) [d]	---	0.50 / 0.94	0.49 / 0.87	---	0.89 / 0.94	---
Phasing Power, centric (iso) [d]	---	2.34	2.30	0	0.03	---
Phasing Power, acentric (iso/ano) [d]	---	2.86 / 1.11	2.78 / 1.51	0 / 0.86	0.02 / 1.27	---
Figure of Merit [d]	---	0.471[e]	0.493[f]	0.808[g]	0.902[h]	---

[a] Numbers in parenthesis are for the highest resolution shell. [b] The average agreement between the independently measured intensities. [c] The root-mean-squared value of the intensity measurements divided by their estimated standard deviation. [d] Compiled from *SHARP* [46]. [e] 2437 centric reflections. [f] 22091 acentric reflections. [g] After solvent flattening, 22966 reflections. [h] After phase extensions to 1.65 Å and solvent flattening. Isomorphous (iso) and anomalous (ano) parameters are indicated.

Model building for both structures was carried out with the program *O* [48] and refinements were with *CNS* [49, 50] and/or *REFMAC5* [51]. Cross-validated, σ_A weighted $2mF_o - DF_c$ and $mF_o - DF_c$ maps [47] were used to evaluate the model and correct errors. Water molecules were placed in the final stages of refinement with *ARP/Waters* and refined with *REFMAC5*. Refinement statistics for all datasets are presented in table 5.2. Validation of the models and Ramachandran analysis were done using *SFCHECK* [52] and *PROCHECK* [53]. Secondary structure assignments were made using *KSDSSP* [54]. The r.m.s.d. between models was calculated with *CCP4*, *Swiss-PDBViewer* (v3.7) [55] or with Q-score analysis by the protein structure comparison service SSM at the European Bioinformatics Institute (http://www.ebi.ac.uk/msd-srv/ssm) [56]. Structure figures were prepared using *CCP4mg* [57, 58], *Swiss-PDBViewer* (v3.7) [55] and *PovRay* (v3.6). A preliminary report describing some of these results has appeared in the Proceedings for the 15th International Symposium on Flavins and Flavoproteins, which was held from April 17-22, 2005 at the Shonan Village Center, Hayama, Japan [59].

5.4 Results

5.4.1. Overall Description of the Structures

The crystal structures for both XenA and XenB are well refined and were repeated with at least two independent data sets obtained from two or more crystals of each enzyme. Table 5.1 summarizes the data collection and phasing statistics for XenA at 283K and XenB at 100K, whereas Table 5.2 presents the refinement statistics for each

structure. The final model for native XenA had an *R*-factor of 15.5% and an *R*-free of 18.2% with data between 35 – 1.65 Å resolution. The final model for native XenB had an *R*-factor of 18.4% and an *R*-free of 27.1% with data between 31 – 2.3 Å resolution. However, the native data set collected for XenA is of higher intensity and quality than the data set collected for XenB.

Table 5.2: Model Refinement Statistics for Oxidized XenA and XenB

	Native XenA	Native XenB
Temperature	283 K	100 K
Resolution range (Å)	35.6 - 1.65	31.3 – 2.3
No. of reflections	84621	33153
R-factor / *R*-free[a] (%)	15.5 / 18.2	18.4 / 27.1
No. of non-H protein atoms	6270	11603
No. of residues fit	722	1392
No. of disordered residues	2	0
No. of water molecules	598	879
No. of FMN molecules	2	4
Ligand molecules	2 Chloride ions / 2 Sulfate ions	4 Sulfate ions / 4 Magnesium
RMS deviations form ideal		
Bond lengths (Å)	0.008	0.019
Bond angles (°)	1.1	1.9
Mean B, protein atoms (Å^2)	16.6	10.1
Mean B, water molecules (Å^2)	35.6	10.5
Mean B, FMN molecules (Å^2)	11.8	8.2
Mean B, ligand molecules (Å^2)	24.5/74.7	8.4 / 10.3
Ramachandran analysis		
Most favored regions (%)	89.6	86.8
Additional allowed regions (%)	9.8	11.2
Generously allowed regions (%)	0.7	1.3
Disallowed regions (%)	0.0	0.8
PDB Code	To be determined	To be determined

[a] Calculated with 10% of the data.

Ribbon diagrams of the functional dimer of XenA and the monomer of XenB are shown in Figure 5.1A and 5.1B, whereas an overlay of a monomer from each enzyme is shown in Figure 5.1C. Each monomer of XenA and XenB adopts a $(\beta/\alpha)_8$ barrel motif,

with a non-covalently bound flavin mononucleotide (FMN) at the C-terminal of the barrel. Therefore, they are both members of the class I $(\beta/\alpha)_8$ barrel family of FMN-containing flavoenzymes [31]. The asymmetric unit for the XenA crystals contains two 363 residue enzymes. Although non-crystallographic symmetry restraints were not applied during the refinement process, the structures for each chain of XenA in the asymmetric unit are nevertheless, very similar to each other (r.m.s. deviation of 0.23 Å over 361 C_α atoms). The crystals of XenB contain four 348 residue enzymes per asymmetric unit. Since the completeness in the highest resolution shells of data was lower than for the XenA data sets, non-crystallographic symmetry restraints and averaging were used for the refinement of the XenB structure. Each monomer of XenB in the asymmetric unit is independent of the other protein chains, suggesting that the enzyme is a functional monomer.

The secondary structure assignments and topology diagrams of the XenA and XenB are shown in Figures 5.2 and 5.3. The classic $(\beta/\alpha)_8$ barrel structure contains eight β/α motifs that form the eight-stranded parallel β-barrel, which is surrounded by eight α-helices [31]. The XenB structure is an example of the classic barrel motif (Figure 5.1B). In contrast, although the two XenA monomers within the asymmetric unit do form a nearly classical $(\beta/\alpha)_8$ barrel motifs, each chain diverges from the classical topology after β-stand eight (Figures 5.1A, 5.2A and 5.3A). Thus the C-terminal region of each chain does not fold back upon the original barrel motif. Instead, after β -strand 8, the main chain crosses the asymmetric unit boundary and forms several important interactions with an adjacent monomer (Figures 5.2A and 5.4). As a consequence, the XenA dimer is

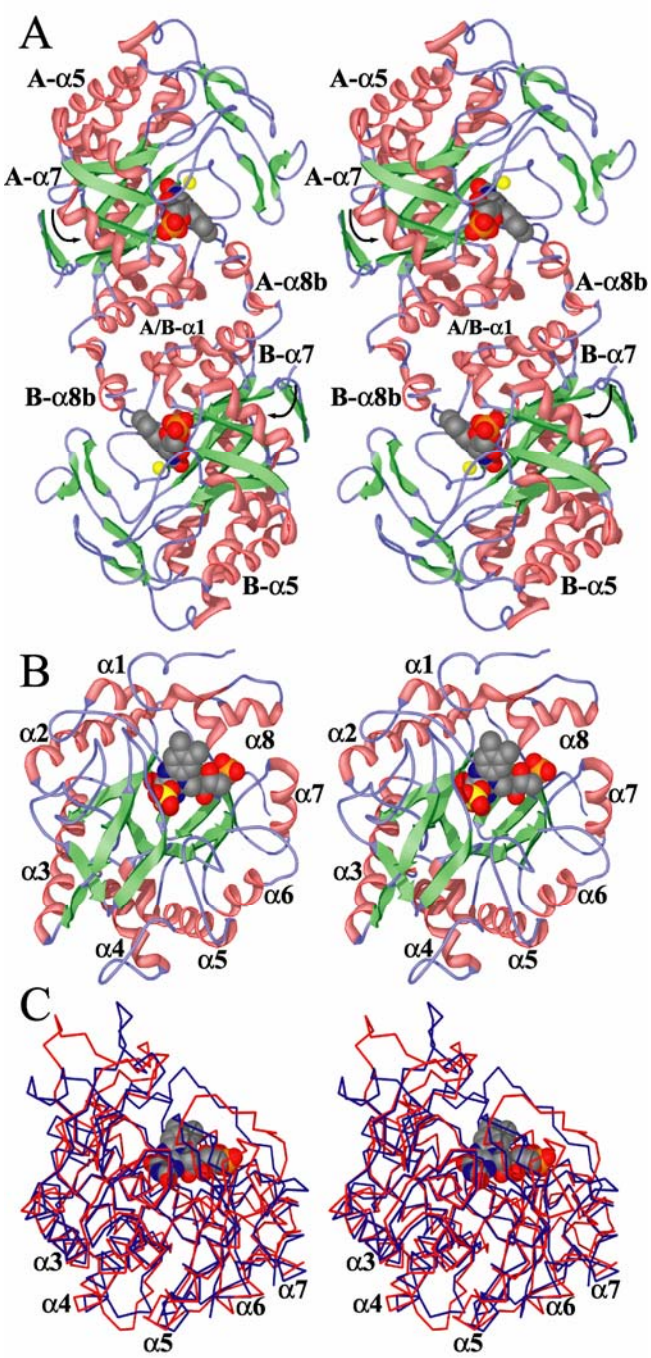

Figure 5.1: Divergent stereo images of the XenA domain-swapped dimer (A) and the XenB monomer (B). The subunits are colored according to secondary structure assignments (α-helix, red; β-strand, green; coil, purple). The FMN, Cl^- (yellow sphere) and SO_4^{2-} in each subunit are shown as CPK atoms with C, N, O, S and P atoms colored grey, blue, red, yellow and magenta, respectively. **C**, Divergent stereo image of the overlayed C_α-trace of XenA and XenB in red and blue respectively. The view in (A) is rotated ~90º around *y* (in the plane of the paper) to obtain (B), which is rotated ~90º around *x* (in the plane of the a paper) to obtain (C).

formed by monomers from adjacent asymmetric units, rather than the two chains within the asymmetric unit. In the normal topology, as illustrated with the structure of XenB, the α-helix 8 folds back onto the original subunit to complete the barrel motif (Figure 5.4A).

The XenA dimer is stabilized by the domain-swapped C-terminal regions and by interactions between α-helix 1 in adjacent subunits (Figures 5.3A, 5.5A and 5.5C). Analysis of the structure shows that 1540 $Å^2$ per monomer (11% of the monomer surface area) is buried at the dimer interface. In contrast, crystal packing of the XenB monomers only buries an average of 1094 $Å^2$ (8.5%) of each subunit. The subunit interface in XenA at α-helix 1 is stabilized by a combination of electrostatic, hydrogen bonding, and van der Waals interactions, particularly involving residues Trp36, Val39, Ser43 and Arg46, among others. For example, the closest contact at the dimer interface occurs at Ser43 in both chains (Figure 5.5A). They are separated by 2.8 Å and hydrogen bond with each other, which may contribute between -0.5 – -1.5 kcal/mol of stabilization [60]. Hydrophobic interactions between Val39 in one subunit and Ser43 and Arg46 in the other subunit flank the inter-subunit, Ser-43-Ser43 hydrogen bond. Finally two inter-subunit cation-π interactions occur between Arg46 and Trp36, which are separated by ~4.4 Å. The average contribution to stability of cation-π interactions involving an arginine residue is -2.9 kcal/mol [61]. Moreover, the terminal nitrogen atoms of the Arg46 sidechain also form hydrogen bonds with to the carbonyl-oxygen atoms of Asp35 and Trp36 of the other subunit. In contrast to XenA, none of these interactions are possible in XenB (Figure 5.5). For example, the structural equivalents of XenA-Trp36, Val39 and Ser43 are XenB-Leu37, Glu40 and Gln44, respectively. Consequently, the bulkier residues in XenB prevent it from forming a similar domain-swapped dimer as observed in

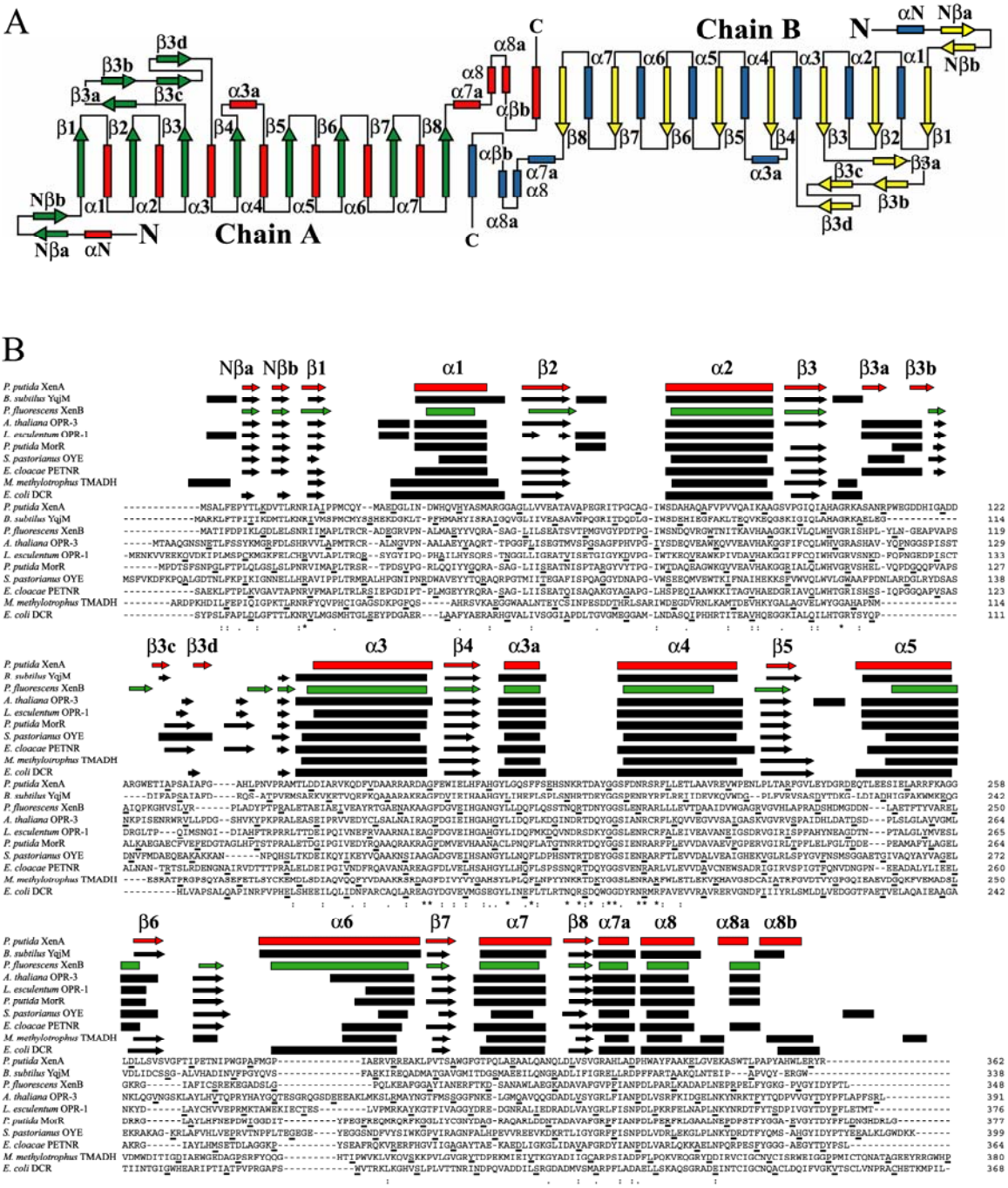

Figure 5.2: Topology diagram and amino acid sequence alignments for XenA, XenB and selected homologs. **A**, The C-terminal, domain-swapped dimer topology of XenA. Alpha helices are illustrated as red and blue boxes for chain A and B, respectively. Beta strands are indicated as green and yellow arrows for chain A and B, respectively. **B**, The amino acid sequence alignment from CLUSTALW for the homologs. The secondary structure labels are as defined for XenA. Structural elements for XenB that do not align with XenA are indicated in green adjacent to that element. Every tenth residue is underlined.

the XenA structure.

The backbone traces for XenA and XenB are very similar to each other as evidenced by the overlay of 278 C_α atoms between XenA-Ala2 to Lys339 and XenB-Thr2 to Ala322 with a r.m.s.d. of 1.3 Å (Figure 5.1C). The similarity between the two structures diverges at XenA-Glu340 and XenB-Asp323, where the C-terminal domain swap starts in XenA. Two sulfate anions are present in the dimer structure of XenA, which stabilize the interaction between helices α8a and α8b at residues Ala346, Ser347 and Arg360 (Figure 5.4A). Helix α8b is the domain-swapped, C-terminal helix in XenA that packs against the active site FMN. This helix is structurally analogous to helix α8a of XenB, despite the fact that the two helices travel in opposite directions. The two alanine residues in the $A_{337}A_{338}K_{339}E_{340}$ sequence at the end of α-helix 8 in XenA correspond to the leucine and lysine residues from the spatially analogous $L_{320}K_{321}A_{322}D_{323}$ sequence in XenB. The two smaller residues in XenA allow for the domain crossover of the backbone trace, whereas the larger residues in XenB do not. Indeed, the side chain of XenA-Ala338 forms hydrophobic interactions with Val343, Ala346 and Thr349. The corresponding residues in XenB are Leu326, Pro329 and Glu332, of which XenB-Glu332 occupies a similar three-dimensional space as the domain-swapped XenA-His356b. Moreover, the next residue is XenA-Trp357b (Trp357b in Figure 5.6A and Figure 5.7A), which packs against the dimethylbenzene ring of the FMN in subunit A. This interaction increases the solvent excluded area of the FMN cofactor in the active site by 12% (72 $Å^2$). Consequently, one portion of the active site in XenA is comprised of the domain swapped C-terminal region. In contrast, the analogous FMN solvent excluded region in XenB

derives from Phe334 and Tyr335, both of which are donated from the same subunit (Figure 5.4, Table 5.3).

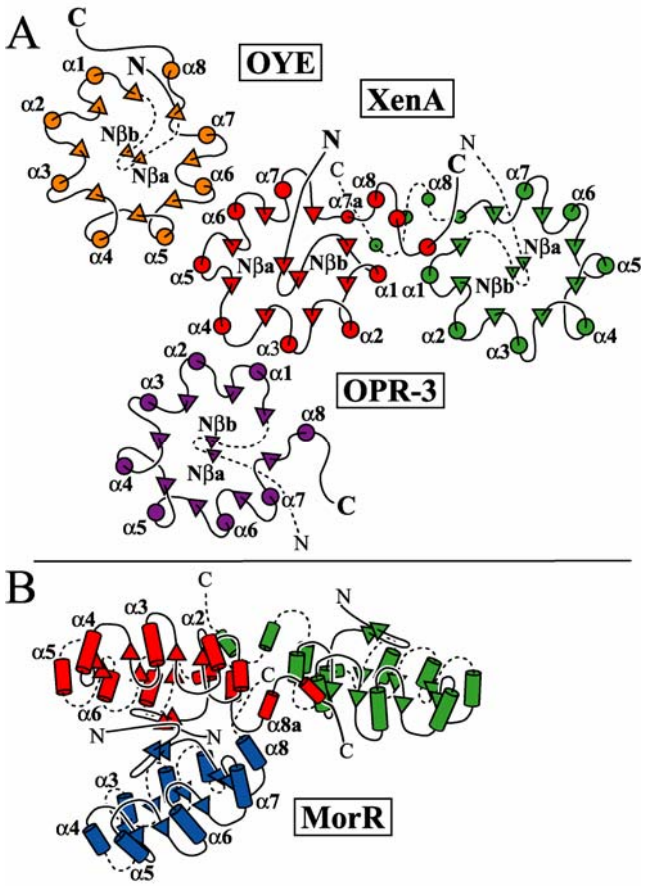

Figure 5.3: Overview of the dimer interfaces formed by homologous to XenA that are known to form dimers. **A,** The domain swapped dimer formed by XenA is shown in red for monomer A and green for monomer B. Helices are indicated as circles and sheets are indicated as triangles. Connectivity is represented by black lines. Dimers as formed by OYE (orange) and OPR-3 (purple) were overlayed with chain A of XenA. Only their dimer partners were consequently drawn in this figure. **B,** The dimer as formed by MorR (blue) was overlayed with XenA and consequently only its dimer partner is shown.

5.4.2 Active Site Structure of XenA and XenB.

Figure 5.6A shows the 1.65 Å resolution $2mF_o - DF_c$ electron density map superimposed with the refined coordinates for the FMN and some of the active site end

Table 5.3: Similarity Between XenA, XenB and Selected Proteins.

Three-Dimensional Superposition of XenA, XenB and Selected Homologs[a]											
	Protein	XenA[b]	XenB[c]	YqjM[d]	OPR-3[e]	OPR-1[f]	MorR[g]	OYE[h]	PETNR[i]	TMADH[j]	DCR[k]
	PDB code	??	??	1z41	1q45	1icq	1gwj	1oyb	1h61	2tmd	1ps9
XenA	% identity[l]	100	31	42	31	27	32	26	30	30	27
	Q-score[m]	---	0.54	0.79	0.51	0.52	0.49	0.44	0.51	0.25	0.31
	r.m.s.d. (Å)[n]	---	1.50	0.96	1.51	1.54	1.52	1.64	1.54	1.78	1.50
	N_{align}[o]	---	291	325	290	289	288	286	292	298	308
XenB	% identity[l]	31	100	32	44	42	52	39	49	24	29
	Q-score[m]	0.54	---	0.59	0.8	0.8	0.8	0.62	0.78	0.25	0.29
	r.m.s.d. (Å)[n]	1.5	---	1.57	1.13	1.15	1.13	1.33	1.08	1.91	1.81
	N_{align}[o]	291	---	296	341	336	337	322	334	297	304

Structurally Equivalent Active Site Residues													
XenA	C24	Y26	A56	I65	T66	Q98	A100	H177	H180	Y182	R230	R325	W357b
YqjM	C26	Y28	A60	I69	T70	Q102	A104	H164	H167	Y169	R215	R308	R366b
XenB	T24	C26	A55	G64	Y65	Q97	W99	H172	N175	Y177	H224	R286	F334, Y335
OPR-3	T33	C35	G64	G73	F74	Q106	W108	H186	H189	Y191	R238	R344	F370, Y371
OPR-1	T37	Q39	A68	G77	Y78	Q110	W112	H187	H190	Y192	R239	R331	F357, Y358
MorR	T32	S34	A62	G71	Y72	Q104	W106	H186	N189	C191	R238	R329	F355, Y356
OYE	T37	M39	G72	G81	Y82	Q114	W116	H191	N194	Y196	R243	R348	F374, Y375
PETNR	T26	L28	A58	G67	Y68	Q100	W102	H181	H184	Y186	R233	R324	F350, Y351
TMADH	C30	G32	Y60	D69	T70	E103	W105	Y169	H172	Y174	R222	R322	I352, W355
DCR	H26	G28	G58	G67	M68	Q100	L102	M161	E164	Y166	R214	R311	C341, L342, I345

[a]Based upon overlays of the given PDB entries and amino acid sequence alignments by the *Protein structure comparison service SSM at European Bioinformatics Institute,* http://www.ebi.ac.uk/msd-srv/ssm [56]. [b]*P. putida* II-B xenobiotic reductase A reported here. [c]*P. fluorescens* I-C xenobiotic reductase B reported here. [d]*B. subtilus* probable NADH-dependent flavin oxidoreductase YqjM. [e]*Arabidopsis thaliana* 12-oxophytodienoate reductase isoform 3. [f]*L. esculentum* 12-oxophytodienoate reductase isoform 1. [g]*P. putida* morphinone reductase. [h]*S. Carlsbergensis* old yellow enzyme. [i]*E. cloacae* pentaerythritol tetranitrate reductase. [j]TIM barrel domain (residues 1-380) of methylotrophic bacterium trimethylamine dehydrogenase. [k]TIM barrel domain (residues 1-368) of *E. coli* 2,4-dienoyl-CoA-reductase. [l]Sequence identity percentile, a quality characteristic of C_α alignment calculated by % sequence = (N_{idet} /N_{align}) , where N_{ident} is the number of identical residues and N_{align} is the number of matched residues in the alignment. [m]Quality function of C_α alignment, $Q = N_{align} * N_{align} / (1 + (\text{r.ms.d.} / R_0)^2 * N_{res1} * N_{res2})$, where N_{align} is the number of matched residues in the alignment, N_{res1} and N_{res2} are the number of residues in the structures aligned and R_0 is an empirical parameter set to 3Å. [n]Root mean square deviation calculated between C_α atoms of matched residues in the best 3D superposition of structures. [o]The number of matched residues in the alignment.

residues of XenA. Figure 5.6B shows a similar region of XenB with electron density maps calculated to 2.3 Å resolution. The majority of the protein-FMN interactions for each enzyme are shown schematically in Figure 5.7. The FMN is located at the C-terminal of the barrel in each structure. The electron density for each cofactor is very well defined, and the average temperature factor for the FMN is 11.8 $Å^2$ for XenA and 20.2 $Å^2$ for XenB. Thus, the cofactor in each active site forms extensive interactions with the surrounding protein residues. Indeed, the average temperature factors for all the atoms located with 5 Å of the FMN in XenA are 13.6 $Å^2$ and 21.6 $Å^2$ in XenB. The FMN *re*-face is excluded from bulk solvent by Pro22 and Met23 in XenA, and Pro22 and Leu23 in XenB. In contrast, the substrate binding cavity is above the FMN *si*-face and the residues that establish the cavity borders are also well defined. The FMN *si*-face solvent accessible cavity in XenA is 1314 $Å^3$ and for XenB is 647 $Å^3$, which are both large enough to bind substrate molecules for both the reductive and oxidative half-reactions.

Oxidized XenA, XenB, and indeed many OYE family members, have an affinity for small anions. The type of anion observed in the structures typically reflects the crystallization conditions. For example, analysis of XenA revealed electron density above the pyrimidine ring of the FMN that was identified through a series of refinement models as a chloride anion. Similarly, XenB binds a sulfate ion in an analogous site. The chloride molecule in XenA interacts with His177 and His180, whereas the sulfate ion in XenB hydrogen bonds with His172, Asn175, Tyr177 and the N3 atom of the FMN.

The structures of XenA and XenB suggest that substrates bind at the FMN *si*-face, where several profound differences and some similarities are apparent (Figures 5.6, 5.7 and Table 5.3). Perhaps the most dramatic difference occurs where the dimethylbenzene

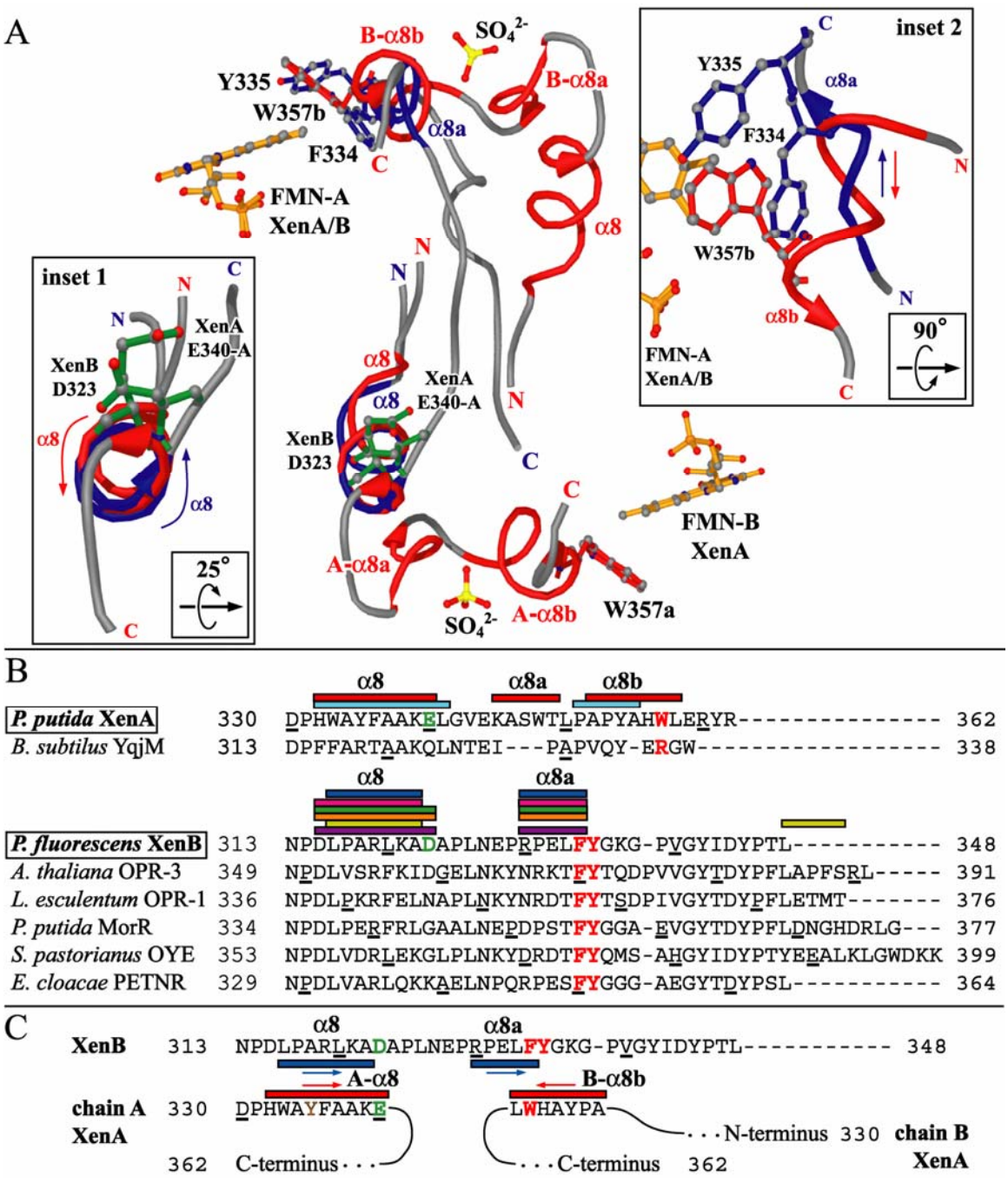

Figure 5.4: Structural analysis of the C-terminal domains of XenA and XenB. **A**, The structural alignment of the C–terminal domains of XenB and XenA rendered as ribbons colored in red and blue respectively. The FMN of XenA and XenB are shown as orange ball and stick. Residues in the C-terminal domains that interact with the dimethylbenzene ring of the FMN are represented in ball and stick and colored the same as the rest of the protein. Inset 1 shows a rotated view of the structurally equivalent α8 helices of XenA (D330-V343) and XenB (A312-L326) with the residues at which the structures diverge (XenA-E340, XenB-D323) in green ball and stick. Inset 2 shows a rotated and enlarged view of the structurally equivalent helices α8b of XenA (P351-E359) and α8a of XenB

(P329-Y335) with their directionality indicated by arrows colored the same as the protein. **B**, Amino acid sequence alignment covering the C-terminal domains of XenA and YqjM with α-helices indicated in red for XenA and cyan for YqjM and the amino acid sequence alignment covering the C-terminal domains of XenB, OPR-3, OPR-1, MorR, OYE and PETNR with α-helices indicated in blue for XenB, magenta for OPR-3, green for OPR-1, orange for MorR, yellow for OYE and purple for PETNR **C**, Structural alignment covering the C-terminal domains of both chains of XenA and XenB with α-helices indicated in red and blue respectively.

ring in XenA interacts with Trp357b from the domain-swapped region. The analogous region in XenB contains Phe334 and Tyr335, which establish a comparable hydrophobic environment for the dimethylbenzene ring. Another dramatic difference is apparent at XenA-Arg230 and XenB-His224. The former residue interacts with the FMN ribityl chain and the N1 atom of the isoalloxazine ring. In contrast, the smaller XenB-His224 residue allows a solvent to occupy the analogous position as the guanidino group of XenA-Arg230. This difference will likely influence the electrostatic environment and reduction potentials of the FMN in both enzymes. For example, reduction of XenA likely yields the $FMNH^-$ anionic species, whereas reduced XenB likely contains a neutral $FMNH_2$ species. The possibility for a $FMNH^-$ anionic species in XenA is supported by the observation of a λ_{max} at approximately 340 nm in the optical spectra of NADPH reduced XenA [2] and is indicative of an anionic reduced FMN [62]. A third region of significant differences occurs around XenA-Ala100 and XenB-Trp99, which also extends to XenA-Ile65, Thr66 and Tyr26 as well as XenB-Gly64, Tyr65 and Cys26. Together, these differences result in a set of complementary large to small substitutions and *vice versa* located above the FMN pyrimidine ring in each enzyme. The most structurally analogous active site residues are: a) XenA-Cys24 -*vs*- XenB-Thr24, b) XenA-Ala56 -*vs*- XenB-Ala55, c) XenA-Gln98 -*vs*- XenB-Gln97, d) XenA-His177 -*vs*- XenB-His172, e)

XenA-His180 -*vs*- XenB-Asn175 and f) XenA-Tyr182 -*vs*- XenB-Tyr177. This region of similarity is clustered around the FMN pyrimidine ring. Together, the results of the similarities and differences between the two enzymes yield active site cavities of similar sizes, but with a rather different distribution of hydrogen bond donors and acceptors, different solvent accessible surface topology, and different electrostatic surface characteristics (Figure 5.6D and E).

5.5 Discussion

5.5.1. Dimerization in Class I ($\beta/\alpha)_8$ Barrel Family of FMN-Containing Flavoenzymes

A number of homologs to XenA are known to exist as dimers, including OYE, MorR and OPR-3 [32, 33]. However, the structure of XenA exhibits a unique C-terminal domain swapped topology resulting in a dimer interface that is completely different than reported for OYE, MorR and OPR-3 (Figure 5.2A and 5.3A). XenA forms a C-terminal domain-swapped homodimer where the A and B subunits are crystallographic two-fold symmetry mates, rather than from within the same asymmetric unit. The subunits in the C-terminal domain-swapped dimer in XenA are arranged in such a way that their active sites are exposed on opposite sides of the dimer. Extensive interactions between α-helix 1 in each monomer include a hydrogen bond between Ser43a and Ser43b and two cation-π interactions at either end of the α -helices 1. These two α -helices are positioned around the two-fold symmetry axis in a nearly perfect antiparallel orientation with respect to the two $(\beta/\alpha)_8$ barrel normals. Interactions between the C-terminal domains of the monomers contribute additional binding energy by providing numerous van der Waals contacts

between the monomers, including Trp357(a/b) that protrudes into the adjacent active site of a neighboring subunit and forms part of the substrate binding pocket by packing against the dimethylbenzene portion of the FMN isoalloxazine ring.

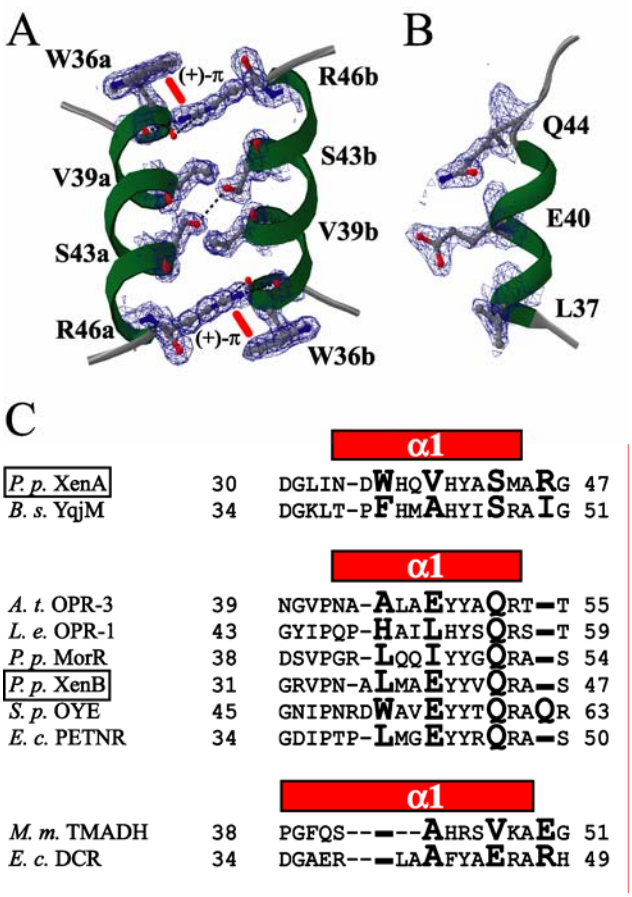

Figure 5.5: Comparison of the dimer interface in XenA with the analogous region in XenB. **A,** The backbone ribbon trace of α-helix 1 with the side chains of XenA drawn as ball and stick and the $2mF_o - DF_c$ electron density superimposed with residues at the interface (2σ contours, 36 –1.65 Å resolution). The hydrogen bond between Ser43a and Ser43b are drawn as dotted lines and the cation-π interactions are labeled. **B,** The α-helix 1 in XenB and the $2mF_o - DF_c$ electron density associated with Glu42 and Gln46 (2σ contours, 31 –2.3 Å resolution). **C,** The sequence alignment shows the structural elements of the proteins. The residues of XenA and their analogs in the homologous are depicted in bold.

The C-terminal domain swap observed in XenA has also very recently been reported for YqjM from *Bacillus subtilis* [41, 42]. However, the structure of YqjM is a dimer of dimers where two C-terminal domain swapped dimers form a weakly interacting tetramer. An analogous tetramer is observed in the crystal packing of the orthorhombic unit cell for XenA, however, no biochemical data supports a biologically active tetramer.A sequence alignment between XenA and YqjM (Figure 5.5C) shows that YqjM-Ser47 is analogous to XenA-Ser43. However, YqjM-Ser47 is in a conformation that will not allow for hydrogen formation with the other monomer. Moreover, the cation-π interaction observed in XenA is not possible in YqjM. Although YqjM does possess a phenylalanine residue (Phe40) at the position analogous to XenA-Trp36, the analog to XenA-Arg46 is YqjM-Ile50. Moreover, the domain-swapped dimers of XenA and YqjM are unique among all class I $(\beta/\alpha)_8$ barrel family members characterized to date, since their primary sequences and structures differentiate them from the other members. Indeed, XenB is a monomer due to the differences particularly at α-helix 1 (Figure 5.5C). Nevertheless, several TIM-barrel proteins, which are not strictly identified as class I $(\beta/\alpha)_8$ barrel family members, do exhibit domain-swapping and can be divided into two categories. Two monomers of the phosphoenolpyruvate mutase/isocitrate lyase-like family [63-67] and HpcH/HpaI aldolase family [68, 69] are domain-swapped at helix α8. However, there is no effect on catalytic activity since the residues involved do not contribute to the active site. Secondly, a number of proteins such as α-isopropylmalate synthase from *M. tuberculosis*, cytosine deaminase from *E. coli*, alanine racemace from *S. lavendulae* and sialic acid synthase NeuB from *N. meningitidis* are domain-swapped, but utilize linker regions [70-73]. In theses cases, the additional linker domain of one

monomer contributes to the active site of another monomer and consequently impacts function.

Some of the other class I $(\beta/\alpha)_8$ barrel family members do form dimers; however, the dimers of OYE, MorR and OPR-3 are very different from XenA. For example, the dimer observed in XenA profoundly impacts active site with a portion of the domain-swapped chain. In contrast, the active sites in OYE, MorR and OPR-3 are independent of dimer formation. Moreover, these latter three enzymes must form different dimers because their primary sequences yield different topologies, which do not allow for domain-swapping, despite similar secondary structures as observed in the C-terminal region of XenA. In addition, the equivalent residue to XenA-Ser43 is a glutamine residue in all other family members including XenB (Figure 5.5C). These bulkier sidechains clearly prevent close association of the first α-helices as observed in XenA. Consequently, the dimer observed in OYE, MorR and OPR-3 is formed through entirely different interfaces (Figure 5.3A and B). For example, in OYE, the dimer interface involves α-helices 4, 5 and 6 of the $(\beta/\alpha)_8$ barrel, but in OPR-3, the interfaces is less extensive and involves α-helices 1 and 2 of one monomer with α-helices 3 and 4 of the other (Figure 5.3A). The dimer of MorR differs from OYE and OPR-3 since it does not only occur through interactions between α- helices 2 and 8, but also through interactions between the N-terminal β-sheet (Nβ1 and Nβ2) that extends over the active sites (Figure 5.3B). This also considerably alters the conformation of both monomers with respect to each other when compared to the dimers for OYE and OPR-3.

5.5.2. Comparison of XenA and XenB to Other Family Members

XenA and XenB are new homologs in the rather large family of class I $(\beta/\alpha)_8$ barrel flavoproteins [31]. The magnitude of their sequence and structural similarity is presented in Table 5.3. XenA and XenB share 31% sequence identity to each other and can be superimposed using 278 C_α atoms resulting in an r.m.s.d. of 1.3 Å. The structure of XenA more closely resembles that of YqjM [41, 42] (42 % sequence identity) where 322 C_α atoms of one monomer overlay with an r.m.s.d. of 0.85 Å. The structure of XenB most closely resembles that of MorR [35] (52 % sequence identity, r.m.s.d. of 0.71 Å over 325 C_α atoms) and PETNR [34] (49 % sequence identity, r.m.s.d. of 0.95 Å over 322 C_α atoms). XenA superimposed with MorR (32 % sequence identity) and PETNR (30 % sequence identy) resulted in an r.m.s.d. of 1.23 Å for MorR when using 266 C_α atoms, and an r.m.s.d. of 1.20 Å for PETNR when using 269 C_α atoms. Not surprisingly, the largest differences between family members occur in the loops observed at the C-terminal end of the $(\beta/\alpha)_8$-barrel. In XenA these loops are much longer than the other homologs and consequently, yield a more buried active site in XenA. Moreover, differences in these loop regions between XenA, XenB and other homologs, is at least partially responsible for the different magnitudes of solvent exposure in the active sites of the different family members. Indeed, XenB has a more exposed FMN cofactor than XenA, and the active site electrostatic surface features of these two proteins also differ.

Another structural difference between XenA, XenB and the homologs occurs at an insert of four β-strands in XenA (β3a, β3b, β3c and β3d in Figure 5.2). These form a β-sheet comprised of antiparallel and parallel strands between β-sheet 3 and α-helix 3. The antiparallel portion of the β-sheets are typically formed by β3b and β3c strands in all

homologs with the exception of XenA, where it is formed by β3a and β3b. The parallel portion of the β-sheet is typically formed by stands β3a and β3d, but in XenA they are formed the by β3c and β3d strands. Considerable diversity is observed for strands β3a and β3b among the family members, which serve to partially define the entrance to the active site in each homolog. In XenB, MorR, PETNR and OPR-3 these two β-strands have conformations that point away from the FMN, whereas in XenA the analogous β-strands protrude into the active site. Consequently, they provide additional shielding of the FMN from bulk solvent.

The C-terminal end of the barrel connecting β6 and α6 is another site of differences between XenA and the other family members. MorR, PETNR and OYE show two loops that connect β5 with α5 and β6 with α6, which both protrude toward the active site channel. In contrast, XenA contains one larger loop that connects β6 with α6 and extends approximately over the analogous space, but yields an active site entrance channel in a more open conformation. To accommodate the larger loop in XenA, the loop connection β5 with α5 points away from the active site and consequently also requires the β6 - α6 loop to partially shield the active site form the solvent. The analogous β6 - α6 loop region in XenB is shorter than in MorR, PETNR or OYE, and consequently yields an active site that is more exposed than XenA or the other homologs.

5.5.3. Active Site Comparison of XenA and XenB

Figure 5.6 shows an overview of the active sites of XenA and XenB. The differences and similarities between the active sites of XenA and XenB yield active sites

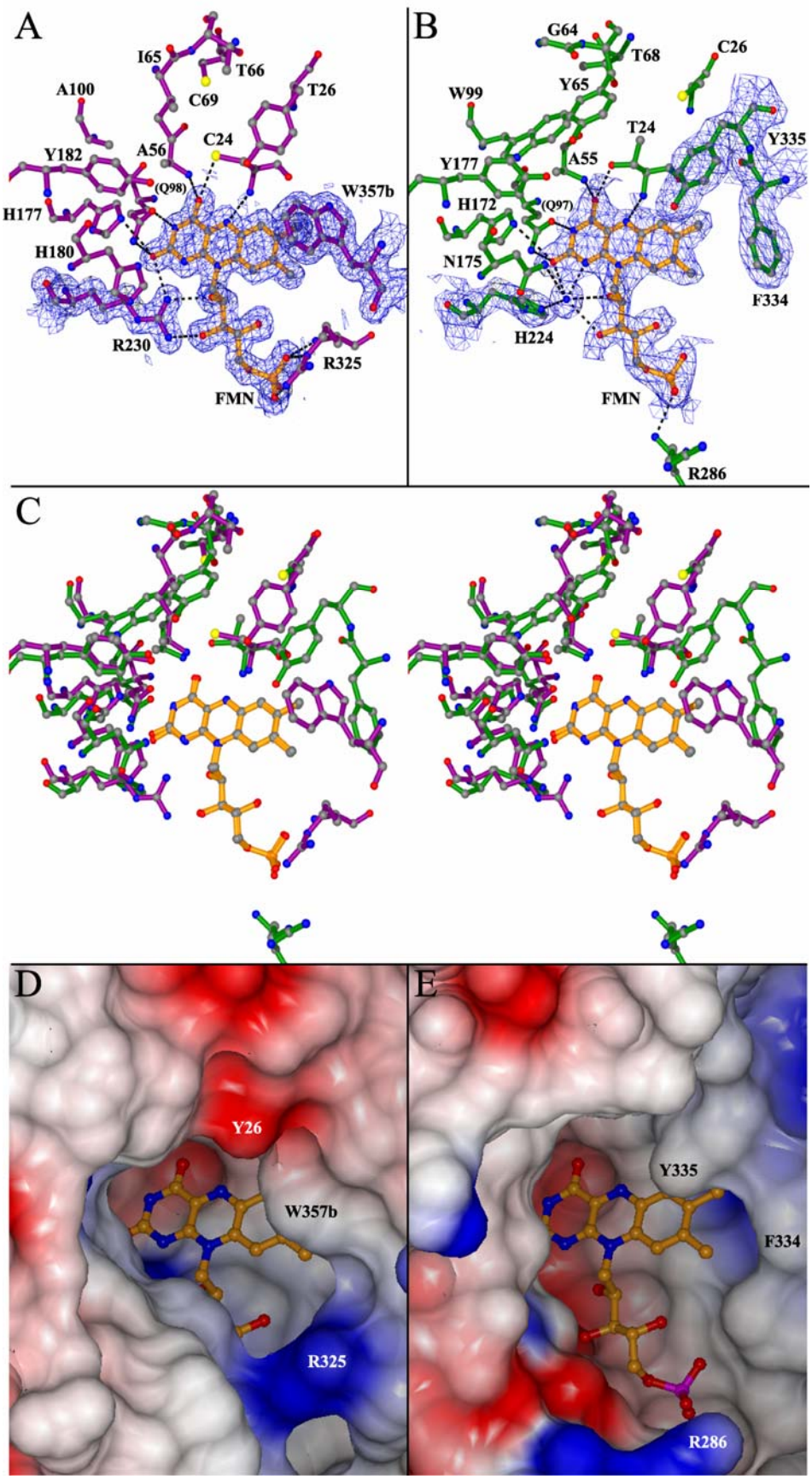
A
I65
T66
A100
C69
T26
C24
A56
Y182
(Q98)
W357b
H177
H180
R230
R325
FMN
B
G64
T68
C26
W99
Y65
T24
Y335
A55
Y177
H172
(Q97)
N175
F334
H224
FMN
R286
C
D
Y26
W357b
R325
E
Y335
F334
R286

Figure 5.6: Comparison of the active site differences and similarities of XenA and XenB. The active site residues of XenA (A), XenB (B) and their FMNs drawn in purple, green and orange ball and stick respectively with superimposed $2mF_o - DF_c$ electron density associated with FMN, Trp357b and Arg230 (1σ contours, 36 –1.65 Å resolution) for XenA and FMN, His224, Phe334 and Tyr335 (1 σ contours, 31 –2.3 Å resolution) for XenB. Hydrogen bonds are shown in dotted black lines. **C,** Divergent stereo image of the active site residues and FMNs of XenA and XenB colored as in (A) and (B) respectively. The electrostatic potential mapped onto the solvent exposed surface of XenA (D) and XenB (E) with a 1.4 Å probe radius and colored according to Poisson-Boltzmann electrostatic potentials from red (-0.5) to blue (0.5).

that are similar in size, but are rather different in their distribution of hydrogen bond donors and acceptors, solvent accessible and electrostatic surface features (Figure 5.6A and B and Figure 5.7). A striking difference between XenA and YqjM with the rest of the homologs is the presence of a cysteine residue (XenA-Cys24, YqjM-Cys26) whereas all other family members have a threonine residue. The thiol group of XenA-Cys24 can hydrogen bond with FMN-O4 and is in close proximity to FMN-N5. However, the other homologs contain a threonine residue in the analogous position. Thus the difference between an R-OH and an R-SH hydrogen bond may impact the reduction potential of the FMN in the different family members. The presence XenA-Cys69, a residue near the active site and Cys24, is unique to XenA among all family members. However, the electron density maps, the distance between the thiol groups of Cys24 and Cys69, and their relative conformations suggest that a disulfide bond is not present and would require additional conformational changes before such a disulfide pair would form. Therefore, despite the presence of two active site cysteine residues in XenA, it is not likely that they function analogously to those found in mitochondrial aldehyde dehydrogenase described by Chen et al. [74]. This will be explored further in the next paper in this series [75].

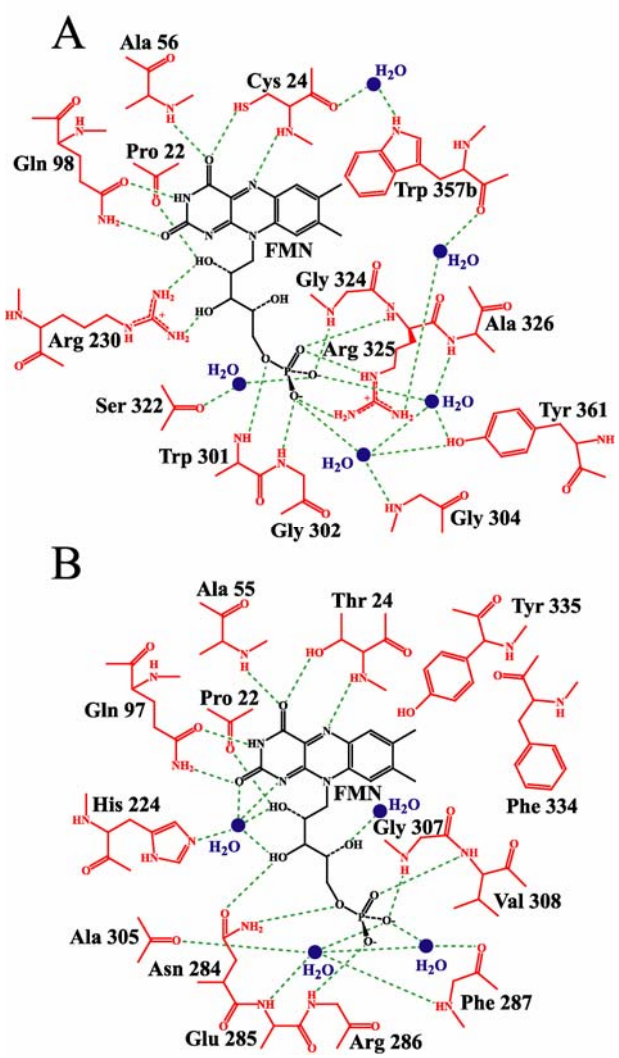

Figure 5.7: The flavin hydrogen bonding environment for XenA and XenB. The FMN molecule and the protein amino acids interacting with it are shown in black and red respectively. Hydrogen bonds are shown in dotted green lines. Water molecules interacting with the flavin are shown as blue spheres. **A,** The flavin hydrogen bonding environment for XenA where the FMN is in close contact with the protein along the phosphate tail and the pyrimidine ring, however, the more hydrophobic end of the flavin ring has no direct interactions with the protein except for a van der Waals contact with Trp357b, which is included in this figure as well. **B,** The flavin hydrogen bonding environment for XenB where the FMN is in close contact with the protein along the phosphate tail and the pyrimidine ring. The structurally equivalent residues to XenA-Trp357b are F334 and Y335.

Comparison of the electrostatic and solvent exposed surface area features for the active sites of XenA and XenB show rather dramatic differences (Figure 5.6D and E). For

example, the FMN in XenB is more exposed than XenA. Indeed, XenA has approximately 5% (~30 $Å^2$) of the surface area of the FMN exposed to bulk solvent. In contrast, approximately 13% (80 $Å^2$) in XenB is exposed. Consequently, XenB should bind bulky substrate molecules more readily than XenA. This is consistent with the observation that XenB preferentially removes the C2 nitro group from nitroglycerin and transforms TNT to a greater extent than XenA [2, 3]. Moreover, the narrow and more sequestered active site of XenA results in a preference for elimination of a terminal nitro group in nitroglycerin and lower affinity for TNT.

Some of the largest differences in the electrostatic surface features of XenA and XenB result from: a) XenA-Arg230, which is structurally analogous to XenB-His224, b) XenA-Arg325 versus XenB-Arg286, and c) XenA-Gly302 versus XenB-Arg286 (Table 5.3). The presence of XenA-Arg230 likely stabilizes the anionic $FMNH^-$ species in reduced enzyme. In contrast, it is anticipated that the reduced FMN in XenB will be neutral since XenB-His224 is located too far away from FMN-N1 to stabilize an anionic species at FMN-N1. In most other homologs, the analog to XenA-Arg230 is typically an arginine residue as well (Figure 5.2, Table 5.3). The residues XenA-Arg325 and XenB-Arg286 are each located such that they serve as a counter ion for the FMN phosphate in their respective enzymes. However, they are donated from different positions in the three dimensional structures and consequently, they have different impacts on the electrostatic surface features of each active site.

Similarities between XenA and XenB active sites occur predominantly near the pyrimidine ring of the FMN molecule. For instance, XenA-Tyr182 and XenB-Tyr177 are equivalent to OYE-Tyr196. Previous results from OYE suggest that OYE-Tyr196 is

important in the oxidative half reaction and is the proton donor [76]. Thus the analogous tyrosine residues in XenA and XenB are very likely to influence ligand positioning, especially for the oxidative half-reaction. Further similarities are noted between residues XenA-His177 and XenA-His180, which are equivalent to XenB-His172 and XenB-Asn175. By analogy to previous results from studies of OYE [77], these residues are also likely to be important in substrate binding. Finally, XenA-Gln98 and XenB-Gln97 each hydrogen bond with the FMN in an analogous manner as OYE-Gln119 [78], which suggest similar roles in stabilizing the FMN binding site and modest influences to both reductive and oxidative half-reactions.

XenA-Ala100 is the structurally equivalent to XenB-Trp99. The tryptophan residue in XenB protrudes much further into the active site cavity and will very likely influence ligand binding. However, XenA-Ile65 is donated from a different position, but occupies an analogous region as XenB-Trp99 and consequently yields similar hydrophobic active site surfaces. Moreover, XenB-Gly64 is analogous to XenA-Ile65, which illustrates a pair of compensatory large to small and *vice versa* substitutions in these two active site cavities. These types of alterations extend further around the active site to include XenA-Thr66, which is analogous to XenB-Tyr65. The latter residue projects a hydrogen bond donor/acceptor hydroxyl group further into the active site above the FMN compared to the former. Consequently, the hydroxyl group of XenA-Thr66 is located deeper into the active site cavity than the hydroxyl group of XenB-Tyr65. In addition, XenA-Tyr26 is structurally equivalent to XenB-Cys26. Although XenA-Try26 does provide likely substrate interactions, XenB-Cys26 is most likely too far away contribute substrate binding interactions. On the other hand, XenB-Tyr335 and XenB-

Phe334 line the active site cavity, which is analogous to the domain-swapped XenA-Trp357b. However, the location of XenB-Tyr335 and XenB-Phe334 are offset with respect to XenA-Trp357b and XenA-Tyr26. Taken together, many of the similarities and differences outlined here will very likely form binding pockets for nitro groups that are different for each active site. Consequently, the structures of the two enzymes suggest a structural basis for substrate specificity, which is further addressed in the following paper. Those results present several crystal structures of ligand complexes and molecular dynamics simulations, that show how each active site does indeed bind identical substrates for the oxidative half-reactions in quite different manners. Moreover, the observed differences correlate well to the different product distributions observed during turnover.

5.6. Acknowledgements

This work was supported in part by the Georgia Tech Research Corporation and the Office of the Vice Provost for Research, Georgia Institute of Technology, an American Chemical Society Petroleum Research Fund type G grant (40310-G4) and an American Heart Association Grant in Aid (0555286B) to A.M.O. and with a grant from the National Science Foundation (MCB-9733734) to B.G.F. Portions of this research were carried out at the Stanford Synchrotron Radiation Laboratory (SSRL), operated by the US Department of Energy, Office of Basic Energy Sciences. The SSRL Structural Molecular Biology Program is supported by the Department of Energy, Office of Biological and Environmental Research an by the National Institutes of Health, National

Center for Research Resources, Biomedical Technology Program and the National Institute of General Medical Sciences. Portions of this work were also carried out at beamline 22-ID in the SER-CAT facilities at the Advanced Photon Source (APS). The use of APS is supported by the US Department of Energy, Basic Energy Sciences, Office of Science under Contract No. W-31-109-Eng-38.

The atomic coordinates and structure factors have been deposited to the Protein Data Bank with the corresponding file names (to be determined).

5.7. References

1. Blehert, D.S., B.G. Fox, and G.H. Chambliss, *Cloning and sequence analysis of two Pseudomonas flavoprotein xenobiotic reductases.* J. Bacteriol., 1999. **181**(20): p. 6254-6263.

2. Blehert, D.S., K.L. Knoke, B.G. Fox, and G.H. Chambliss, *Regioselectivity of nitroglycerin denitration by flavoprotein nitroester reductases purified from two Pseudomonas species.* J. Bacteriol., 1997. **179**(22): p. 6912-6920.

3. Pak, J.W., K.L. Knoke, D.R. Noguera, B.G. Fox, and G.H. Chambliss, *Transformation of 2,4,6-trinitrotoluene by purified xenobiotic reductase B from Pseudomonas fluorescens I-C.* Appl. Environ. Microbiol., 2000. **66**(11): p. 4742-4750.

4. Tassorelli, C., S.A. Joseph, M.G. Buzzi, and G. Nappi, *The effects on the central nervous system of nitroglycerin--putative mechanisms and mediators.* Prog. Neurobiol., 1999. **57**(6): p. 607-24.

5. Fung, H.L., *Clinical pharmacology of organic nitrates.* Am. J. Cardiol., 1993. **72**(8): p. 9C-13C; discussion 14C-15C.

6. Fung, H.L., *Biochemical mechanism of nitroglycerin action and tolerance: is this old mystery solved?* Annu. Rev. Pharmacol. Toxicol., 2004. **44**: p. 67-85.

7. Ahlner, J., R.G. Andersson, K. Torfgard, and K.L. Axelsson, *Organic nitrate esters: clinical use and mechanisms of actions.* Pharmacol. Rev., 1991. **43**(3): p. 351-423.

8. Murrell, W., *Nitroglycerin as a remedy for angina pectoris.* Lancet, 1879. **1**: p. 80-81.

9. Gori, T. and J.D. Parker, *Nitrate tolerance: a unifying hypothesis.* Circulation, 2002. **106**(19): p. 2510-3.

10. Gori, T., P. Harvey, J.S. Floras, and J.D. Parker, *Continuous therapy with nitroglycerin impairs endothelium-dependent vasodilation but does not cause tolerance in conductance arteries: a human in vivo study.* J. Cardiovasc. Pharmacol., 2004. **44**(5): p. 601-6.

11. Parker, J.D. and J.O. Parker, *Nitrate therapy for stable angina pectoris.* N. Engl. J. Med., 1998. **338**(8): p. 520-31.

12. Tsuchida, S., T. Maki, and K. Sato, *Purification and characterization of glutathione transferases with an activity toward nitroglycerin from human aorta and heart. Multiplicity of the human class Mu forms.* J. Biol. Chem., 1990. **265**(13): p. 7150-7.

13. Yeates, R.A., H. Laufen, and M. Leitold, *The reaction between organic nitrates and sulfhydryl compounds. A possible model system for the activation of organic nitrates.* Mol. Pharmacol., 1985. **28**(6): p. 555-9.

14. Yeates, R.A., M. Schmid, and M. Leitold, *Antagonism of glycerol trinitrate activity by an inhibitor of glutathione S-transferase.* Biochem. Pharmacol., 1989. **38**(11): p. 1749-53.

15. Millar, T.M., C.R. Stevens, N. Benjamin, R. Eisenthal, R. Harrison, and D.R. Blake, *Xanthine oxidoreductase catalyses the reduction of nitrates and nitrite to nitric oxide under hypoxic conditions.* FEBS Lett., 1998. **427**(2): p. 225-8.

16. Millar, T.M., *Peroxynitrite formation from the simultaneous reduction of nitrite and oxygen by xanthine oxidase.* FEBS Lett., 2004. **562**(1-3): p. 129-33.

17. Millar, T.M., J.M. Kanczler, T. Bodamyali, D.R. Blake, and C.R. Stevens, *Xanthine oxidase is a peroxynitrite synthase: newly identified roles for a very old enzyme.* Redox. Rep., 2002. **7**(2): p. 65-70.

18. McDonald, B.J. and B.M. Bennett, *Biotransformation of glyceryl trinitrate by rat aortic cytochrome P450.* Biochem. Pharmacol., 1993. **45**(1): p. 268-70.

19. Bennett, B.M., B.J. McDonald, R. Nigam, and W.C. Simon, *Biotransformation of organic nitrates and vascular smooth muscle cell function.* Trends. Pharmacol. Sci., 1994. **15**(7): p. 245-9.

20. McGuire, J.J., D.J. Anderson, B.J. McDonald, R. Narayanasami, and B.M. Bennett, *Inhibition of NADPH-cytochrome P450 reductase and glyceryl trinitrate biotransformation by diphenyleneiodonium sulfate.* Biochem. Pharmacol., 1998. **56**(7): p. 881-93.

21. Seth, P. and H.L. Fung, *Biochemical characterization of a membrane-bound enzyme responsible for generating nitric oxide from nitroglycerin in vascular smooth muscle cells.* Biochem. Pharmacol., 1993. **46**(8): p. 1481-6.

22. Bauer, J.A. and H.L. Fung, *Specific binding of nitroglycerin to coronary artery microsomes. Evidence of a vascular nitrate binding site.* Biochem. Pharmacol., 1996. **52**(4): p. 619-25.

23. Nathan, C. and M.U. Shiloh, *Reactive oxygen and nitrogen intermediates in the relationship between mammalian hosts and microbial pathogens.* Proc. Natl. Acad. Sci. U. S. A., 2000. **97**(16): p. 8841-8.

24. Bogdan, C., *Nitric oxide and the immune response.* Nat. Immunol., 2001. **2**(10): p. 907-16.

25. MacMicking, J., Q.W. Xie, and C. Nathan, *Nitric oxide and macrophage function.* Annu. Rev. Immunol., 1997. **15**: p. 323-50.

26. Xu, W.M. and L.Z. Liu, *Nitric oxide: from a mysterious labile factor to the molecule of the Nobel Prize. Recent progress in nitric oxide research.* Cell Res., 1998. **8**(4): p. 251-8.

27. Chen, Z., J. Zhang, and J.S. Stamler, *Identification of the enzymatic mechanism of nitroglycerin bioactivation.* Proc. Natl. Acad. Sci. U. S. A., 2002. **99**(12): p. 8306-11.

28. Sisson, G., J.Y. Jeong, A. Goodwin, L. Bryden, N. Rossler, S. Lim-Morrison, A. Raudonikiene, D.E. Berg, and P.S. Hoffman, *Metronidazole activation is mutagenic and causes DNA fragmentation in Helicobacter pylori and in Escherichia coli containing a cloned H. pylori rdxA^{+} (Nitroreductase) gene.* J. Bacteriol., 2000. **182**(18): p. 5091-5096.

29. Sisson, G., A. Goodwin, A. Raudonikiene, N.J. Hughes, A.K. Mukhopadhyay, D.E. Berg, and P.S. Hoffman, *Enzymes associated with reductive activation and action of nitazoxanide, nitrofurans, and metronidazole in Helicobacter pylori.* Antimicrob. Agents Chemother., 2002. **46**(7): p. 2116-2123.

30. Trinh, S. and G. Reysset, *Mutagenic action of 5-nitroimidazoles: in vivo induction of GC --> CG transversion in two Bacteroides fragilis reporter genes.* Mutat. Res., 1998. **398**(1-2): p. 55-65.

31. Nagano, N., C.A. Orengo, and J.M. Thornton, *One fold with many functions: the evolutionary relationships between TIM barrel families based on their sequences, structures and functions.* J. Mol. Biol., 2002. **321**(5): p. 741-765.

32. Fox, K.M. and P.A. Karplus, *Old yellow enzyme at 2 Å resolution: overall structure, ligand binding, and comparison with related flavoproteins.* Structure, 1994. **2**(11): p. 1089-1105.

33. Karplus, P.A., K.M. Fox, and V. Massey, *Flavoprotein structure and mechanism. 8. Structure-function relations for old yellow enzyme.* FASEB J., 1995. **9**(15): p. 1518-1526.

34. Barna, T.M., H. Khan, N.C. Bruce, I. Barsukov, N.S. Scrutton, and P.C. Moody, *Crystal structure of pentaerythritol tetranitrate reductase: "flipped" binding geometries for steroid substrates in different redox states of the enzyme.* J. Mol. Biol., 2001. **310**(2): p. 433-447.

35. Barna, T., H.L. Messiha, C. Petosa, N.C. Bruce, N.S. Scrutton, and P.C. Moody, *Crystal structure of bacterial morphinone reductase and properties of the C191A mutant enzyme.* J. Biol. Chem., 2002. **277**(34): p. 30976-30983.

36. Breithaupt, C., J. Strassner, U. Breitinger, R. Huber, P. Macheroux, A. Schaller, and T. Clausen, *X-ray structure of 12-oxophytodienoate reductase 1 provides structural insight into substrate binding and specificity within the family of OYE.* Structure (Camb), 2001. **9**(5): p. 419-429.

37. Malone, T.E., S.E. Madson, R.L. Wrobel, W.B. Jeon, N.S. Rosenberg, K.A. Johnson, C.A. Bingman, D.W. Smith, G.N. Phillips, Jr., J.L. Markley, and B.G. Fox, *X-ray structure of Arabidopsis At2g06050, 12-oxophytodienoate reductase isoform 3.* Proteins, 2005. **58**(1): p. 243-245.

38. Hubbard, P.A., X. Liang, H. Schulz, and J.J. Kim, *The crystal structure and reaction mechanism of Escherichia coli 2,4-dienoyl-CoA reductase.* J. Biol. Chem., 2003. **278**(39): p. 37553-37560.

39. Barber, M.J. and P.J. Neame *Correlation of x-ray deduced and experimental amino acid sequences of trimethylamine dehydrogenase.* J. Biol. Chem., 1992. **267**(10): p. 6611-6619.

40. Trickey, P., J. Basran, L. Lian, Z. Chen, J.D. Barton, M.J. Sutcliffe, N.S. Scrutton, and F.S. Mathews, *Structural and biochemical characterization of recombinant wild type and a C30A mutant of trimethylamine dehydrogenase from Methylophilus methylotrophus (sp. W_3A_1).* Biochemistry, 2000. **39**(26): p. 7678-7688.

41. Fitzpatrick, T.B., N. Amrhein, and P. Macheroux, *Characterization of YqjM, an Old Yellow Enzyme homolog from Bacillus subtilis involved in the oxidative stress response.* J. Biol. Chem., 2003. **278**(22): p. 19891-19897.

42. Kitzing, K., T.B. Fitzpatrick, C. Wilken, J. Sawa, G.P. Bourenkov, P. Macheroux, and T. Clausen, *The 1.3 Å crystal structure of the flavoprotein YqjM reveals a novel class of Old Yellow Enzymes.* J. Biol. Chem., 2005. **280**(30): p. 27904-27913.

43. Orville, A.M., L. Manning, D.S. Blehert, J.M. Studts, B.G. Fox, and G.H. Chambliss, *Crystallization and preliminary analysis of xenobiotic reductase A and ligand complexes from Pseudomonas putida II-B.* Acta Cryst., 2004. **D60**(Pt 5): p. 957-961.

44. Orville, A.M., L. Manning, D.S. Blehert, B.G. Fox, and G.H. Chambliss, *Crystallization and preliminary analysis of xenobiotic reductase B from Pseudomonas fluorescens I-C.* Acta Cryst., 2004. **D60**(Pt 7): p. 1289-1291.

45. Terwilliger, T.C. and J. Berendzen, *Automated MAD and MIR structure solution.* Acta Cryst., 1999. **D55**(Pt 4): p. 849-861.

46. La Fortelle, E.d. and G. Bricogne, *Maximum-likelihood heavy-atom parameter refinement for multiple isomorphous replacement and multiwavelength anomalous diffraction methods.* Methods Enzymol., 1997. **276**(Pt A): p. 472-494.

47. Collaborative Computational Project, N., *The CCP4 Suite: Programs for Protein Crystallography.* Acta Cryst., 1994. **D50**(Pt 5): p. 760-763.

48. Brünger, A.T., P.D. Adams, G.M. Clore, W.L. DeLano, P. Gros, R.W. Grosse-Kunstleve, J.S. Jiang, J. Kuszewski, M. Nilges, N.S. Pannu, R.J. Read, L.M. Rice, T. Simonson, and G.L. Warren, *Crystallography & NMR system: A new software suite for macromolecular structure determination.* Acta Cryst., 1998. **D54**(Pt 5): p. 905-921.

49. Murshudov, G.N., A.A. Vagin, A. Lebedev, K.S. Wilson, and E.J. Dodson, *Efficient anisotropic refinement of macromolecular structures using FFT.* Acta Cryst., 1999. **D55**(Pt 1): p. 247-255.

50. Pannu, N.S., G.N. Murshudov, E.J. Dodson, and R.J. Read, *Incorporation of prior phase information strengthens maximum-likelihood structure refinement.* Acta Cryst., 1998. **D54**(Pt 6, no. 2): p. 1285-1294.

51. Read, R.J., *Model phases: Probabilities and bias.* Methods Enzymol., 1997. **277**(Pt B): p. 110-128.

52. Vaguine, A.A., J. Richelle, and S.J. Wodak, *SFCHECK: a unified set of procedure for evaluating the quality of macromolecular structure-factor data and their agreement with atomic model.* Acta Cryst., 1999. **D55**(Pt 1): p. 191-205.

53. Laskowski, R.A., M.W. MacArthur, D.S. Moss, and J.M. Thornton, *Computer Programs.* J. Appl. Cryst., 1993. **26**(2): p. 283-291.

54. Kabsch, W. and C. Sander, *Dictionary of protein secondary structure: Pattern recognition of hydrogen-bonded and geometrical features.* Biopolymers, 1983. **22**(12): p. 2577-2637.

55. Guex, N. and M.C. Peitsch, *SWISS-MODEL and the Swiss-PdbViewer: An environment for comparative protein modeling.* Electrophoresis, 1997. **18**(15): p. 2714-2723.

56. Krissinel, E. and K. Henrick, *Secondary-structure matching (SSM), a new tool for fast protein structure alignment in three dimensions.* Acta Cryst., 2004. **D60**(Pt 12, Pt 1): p. 2256-2268.

57. Potterton, L., S. McNicholas, E. Krissinel, J. Gruber, K. Cowtan, P. Emsley, G.N. Murshudov, S. Cohen, A. Perrakis, and M. Noble, *Developments in the CCP4 molecular-graphics project.* Acta Cryst., 2004. **D60**(Pt 12 Pt 1): p. 2288-2294.

58. Potterton, E., S. McNicholas, E. Krissinel, K. Cowtan, and M. Noble, *The CCP4 molecular-graphics project.* Acta Cryst., 2002. **D58**(Pt 11): p. 1955-1957.

59. Orville, A.M., A. Nagpal, L. Manning, D.S. Blehert, M.P. Valley, G.H. Chambliss, B.G. Fox, and P.F. Fitzpatrick, *A structural perspective on nitrite elimination of organic nitrochemicals by flavoenzymes.* Proceedings of the 15th International Symposium on Flavins and Flavoproteins, Shonan Village Center, Japan, 2005.

60. Williams, D.H., M.S. Searle, J.P. Mackay, U. Gerhard, and R.A. Maplestone, *Toward an estimation of binding constants in aqueous solution: studies of associations of vancomycin group antibiotics.* Proc. Natl. Acad. Sci. USA, 1993. **90**(4): p. 1172-1178.

61. Gallivan, J.P. and D.A. Dougherty, *Cation-π interactions in structural biology.* Proc. Natl. Acad. Sci. USA, 1999. **96**(17): p. 9459-9464.

62. Ghisla, S., V. Massey, J.M. Lhoste, and S.G. Mayhew, *Fluorescence and optical characteristics of reduced flavines and flavoproteins.* Biochemistry, 1974. **13**(3): p. 589-597.

63. Huang, K., Z. Li, Y. Jia, D. Dunaway-Mariano, and O. Herzberg, *Helix swapping between two α/β barrels: crystal structure of phosphoenolpyruvate mutase with bound Mg^{2+}–oxalate.* Structure Fold Des., 1999. **7**(5): p. 539-548.

64. Grimm, C., A. Evers, M. Brock, C. Maerker, G. Klebe, W. Buckel, and K. Reuter, *Crystal Structure of 2-Methylisocitrate Lyase (PrpB) from Escherichia coli and Modelling of its Ligand Bound Active Centre.* J. Mol. Biol., 2003. **328**(3): p. 609-621.

65. Britton, K.L., S.J. Langridge, P.J. Baker, K. Weeradechapon, S.E. Sedelnikova, J.R. De Lucas, D.W. Rice, and G. Turner, *The crystal structure and active site location of isocitrate lyase from the fungus Aspergillus nidulans.* Structure Fold Des., 2000. **8**(4): p. 349-362.

66. Sharma, V., S. Sharma, K. Hoener zu Bentrup, J.D. McKinney, D.G. Russell, W.R. Jacobs Jr., and J.C. Sacchettini, *Structure of isocitrate lyase, a persistence factor of Mycobacterium tuberculosis.* Nat. Struc. Biol., 2000. **7**(8): p. 663-668.

67. Britton, K.L., I.S.B. Abeysinghe, P.J. Baker, V. Barynin, P. Diehl, S.J. Langridge, B.A. McFadden, S.E. Sedelnikova, T.J. Stillman, K. Weeradechapon, and D.W. Rice, *The structure and domain organization of Escherichia coli isocitrate lyase.* Acta Cryst., 2001. **D57**(Pt 9): p. 1209-1218.

68. Ose, T., K. Watanabe, T. Mie, M. Honma, H. Watanabe, M. Yao, H. Oikawa, and I. Tanake, *Insight into a natural Diels–Alder reaction from the structure of macrophomate synthase.* Nature, 2003. **422**(6928): p. 185-189.

69. Izard, T. and N.C. Blackwell, *Crystal structures of the metal-dependent 2-dehydro-3-deoxy-galactarate aldolase suggests a novel reaction mechanism.* EMBO J., 2000. **19**(15): p. 3849-3856.

70. Koon, N., C.J. Squire, and E.N. Baker, *Crystal structure of LeuA from Mycobacterium tuberculosis, a key enzyme in leucine biosynthesis.* Proc. Natl. Acad. Sci. USA, 2004. **101**(22): p. 8295-8300.

71. Ireton, G.C., G. McDermott, M.E. Black, and B.L. Stoddard, *The Structure of Escherichia coli Cytosine Deaminase.* J. Mol. Biol., 2002. **315**(4): p. 687-697.

72. Noda, M., Y. Matoba, T. Kumagai, and M. Sugiyama, *Structural evidence that alanine racemase from a D-cycloserine-producing microorganism exhibits resistance to its own product.* J. Biol. Chem., 2004. **279**(44): p. 46153-46161.

73. Gunawan, J., D. Simard, M. Gilbert, A.L. Lovering, W.W. Wakarchuk, M.E. Tanner, and N.C. Strynadka, *Structural and Mechanistic Analysis of Sialic Acid Synthase NeuB from Neisseria meningitidis in Complex with Mn^{2+}, phosphoenolpyruvate, and N-acetylmannosaminitol.* J. Biol. Chem., 2005. **280**(5): p. 3555-3563.

74. Chen, Z., J. Zhang, and J.S. Stamler, *Identification of the enzymatic mechanism of nitroglycerin bioactivation.* Proc. Natl. Acad. Sci. U. S. A., 2002. **99**(12): p. 8306-8311.

75. Manning, L., D.S. Blehert, G.H. Chambliss, B.G. Fox, and A.M. Orville, *Structural Insight into Regiospecific Reactions with Nitrocompounds by Xenobiotic Reductases A and B.* In preparation for Biochemistry.

76. Kohli, R.M. and V. Massey, *The oxidative half-reaction of Old Yellow Enzyme. The role of tyrosine 196.* J. Biol. Chem., 1998. **273**(49): p. 32763-32770.

77. Brown, B.J., Z. Deng, P.A. Karplus, and V. Massey, *On the active site of Old Yellow Enzyme. Role of histidine 191 and asparagine 194.* J. Biol. Chem., 1998. **273**(49): p. 32753-32762.

78. Brown, B.J., J.W. Hyun, S. Duvvuri, P.A. Karplus, and V. Massey, *The role of glutamine 114 in old yellow enzyme.* J. Biol. Chem., 2002. **277**(3): p. 2138-2145.

6. STRUCTURAL INSIGHT INTO REGIOSPECIFIC REACTIONS WITH NITROCOMPOUNDS BY XENOBIOTIC REDUCTASE A AND B

6.1 Abstract

Xenobiotic reductases A and B (XenA from, *Pseudomonas putida* II-B; XenB from *Pseudomonas fluorescens* I-C) catalyze the regiospecific, NADPH-dependent, nitrite elimination from nitroglycerin, or the reduction of aromatic nitrocompounds or nitroaliphatics. In the previous paper we described the crystal structures for the resting state of each enzyme [1]. Here we report the crystal structures of oxidized XenA, co-crystallized with 1.6 m*M* metronidazole, or aerobically reduced with NADPH, as well as molecular dynamics simulations of substrate binding to reduced XenA and XenB. The structures, typically to between 1.9 Å and 1.5 Å resolution at 100 K, of oxidized and reduced XenA reveal that spermine binds at the *si*-face of the FMN, which is replaced by metronidazole in the oxidized enzyme. In contrast, nitroglycerin and TNT are not observed in the oxidized enyme active site despite several attempts by either co-crystallization or soaking into preformed crystals of XenA. Rather, spermine, which was necessary for crystallization, excludes nitroglycerin and TNT from binding.

Formatted from: **Manning, L.**, Blehert, D.S., Chambliss, G.H., Fox, B.G. & Orville, A.M. "Structural Insight into Regiospecific Reactions with Nitrocompounds by Xenobiotic Reductases A and B" *In preparation for Biochemistry*

The molecular dynamics binding analysis shows that the complexes formed with either nitroglycerin, 1,2- and 1-3dintroglycerin isomers, TNT, or metronidazole are consistent with kinetic and product analysis determined previously for these enzymes [2-4].

6.2 Introduction

Microbial life started evolving on Earth about four billion years ago [5, 6]. But because life is limited to "mild" reaction conditions, the mechanistic strategies utilized in the biosphere are also consequently "limited". Moreover, competition between organisms for natural resources has been an important factor for much of evolutionary time. Thus microbes have evolved to the point where they are now responsible for most of the transformations and flux of the chemical cycles in the biosphere [7]. The success and ubiquity of microbes arises from their ability to metabolize diverse compounds in response to changes in environmental conditions [8] and exploit chemicals introduced by recent human activities [9]. Xenobiotic reductases A (XenA) from *Pseudomonas putida* II-B and B (XenB) from *Pseudomonas fluorescens* I-C were originally purified from bacterial strains isolated from the contaminated, World War II era, Badger munitions manufacturing plant in Baraboo, WI. These strains were identified because they not only tolerate high concentrations of nitroglycerin that are toxic to nearly all other organisms, but they can also obtain all their nitrogen for growth from the xenobiotic compound [2]. The enzymes responsible for this process, XenA and XenB, catalyze NADPH-dependent reductive elimination of nitrite from nitroglycerin (TNG), resulting in the main product, 1,2-dinitroglycerol for XenA and 1,3-dinitroglyerol for XenB (Scheme 1). Subsequent

turnover of these dinitroglycerols by either enzyme results in 2-mononitroglycerol and 1-mononitroglycerol, respectively, which are not transformed further. Consequently, neither *P. putida* II-B nor *P. fluorescens* I-C are capable of utilizing TNG as a source of carbon. The nitrite eliminated by either XenA or XenB provides an adequate nitrogen source to support growth. XenA and XenB also show differences in their NADPH-coupled reactions with 2,4,6-trinitrotoluene (TNT). XenB exhibits five times higher specific activity with TNT than XenA. Approximately 50% of the reducing equivalents yield nitro group reduction and the other half yields aromatic ring reduction. Aromatic ring reduction by two and four electrons yields the colored hydride-Meisenheimer (H-TNT, λ_{max} = 477 nm) and tautomers of the dihydride-Meisenheimer complex (2H-TNT, λ_{max} = 449 - 492 nm) products, respectively [4]. Thus XenB yields more ring reduction of TNT than XenA or any of the other characterized homologs. The nitroaliphatic, metronidazole, also transformed *in vitro* by XenA and XenB, yields the toxic nitroso- and hydroxylamino-derivatives. Moreover, cultures of *E. coli* DH5α die in the presence of metronidazole when they express either XenA or XenB, suggesting that XenA and XenB generate these toxic metabolites *in vivo* as well (B. G. Fox, personal communication). This reactivity is similar to that of pathogens that are susceptible to this class of pro-drug [10-12].

XenA and XenB both belong to the class I $(\beta/\alpha)_8$ barrel family of FMN-containing flavoenzymes. However, XenA is a C-terminal domain-swapped dimer, whereas XenB is a monomer. They each show close sequence homology to the prototypical member, old yellow enzyme (OYE) [13, 14], as well as to pentaerythritol tetranitrate reductase (PETNR) [15], morphinone reductase (MorR) [16], 1,2-

oxophytodienoate reductase isoform 1 (OPR-1) [17] and 3 (OPR-3) [18], 2,4-dienoyl-CoA reductase (DCR) [19] and the isoforms of trimethylamine dehydrogenase (TMADH) [20]. These enzymes typically proceeds via a ping-pong kinetic mechanism with an NADPH-dependent reductive half-reaction, but a variety of substrates are able to participate in the oxidative half-reaction.

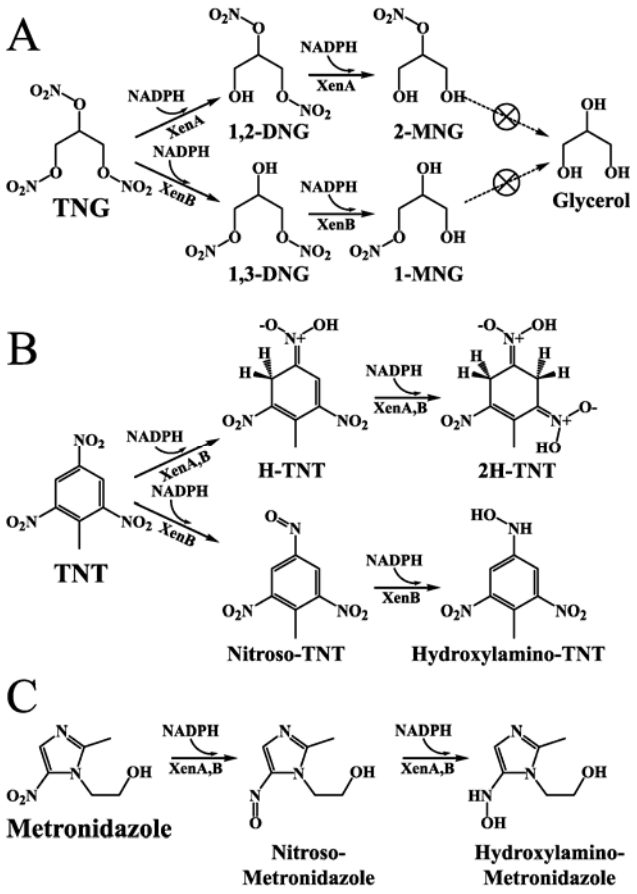

Scheme 6.1: Overview of reactivity of XenA and XenB. (A), XenA and XenB exhibit regiospecific reactions with nitroglycerin, which yield different product distributions. (B) XenA and XenB both reduce TNT to yield nitro group or aromatic ring reduction. (C) XenA and XenB reduce metronidazole to yield the nitroso- and hydroxylamino intermediates.

Here we report the crystal structures, typically to higher than 1.9 Å resolution, of oxidized and reduced XenA from *Pseudomonas putida* II-B and several ligand complexes formed with oxidized enzyme, along with ligand complexes of reduced XenA and XenB determined by molecular dynamics calculations. The crystal structures demonstrate that ligands bind to the *si*-face of the FMN and that the isoalloxazine ring experiences significant deviations from planarity upon reduction. The active site of XenA contains two cysteine residues, one of which (Cys24) hydrogen bonds with the N5 and O4 positions of the FMN. The structural analysis indicates that this residue also forms a sulfenic acid (Cys-SOH), presumably in a H_2O_2 dependent manner. The molecular dynamics models were calculated because no diffraction grade crystals could be obtained for XenA and XenB containing ligand molecules. These calculated models are in agreement with kinetic and product analysis determined previously for these enzymes [2-4].

6.3 Materials and Methods

6.3.1. Protein Expression and Purification

Single crystals were obtained for XenA from *Pseudomonas putida* II-B or from the *Escherichia coli* expression host and was isolated as previously described [21]. Optical spectra were collected at room temperature with an Agilent Technologies (Wilmington, DE) 8453 diode array spectrometer.

6.3.2. Crystallization and X-ray Diffraction Data Collection

All XenA crystals were grown in the presence of 20 m*M* spermine tetrahydrochloride. Oxidized XenA crystals were rapidly transferred to Paratone N and flash frozen with liquid N_2. Crystals of reduced XenA were obtained by aerobic reduction of XenA by placing single crystals into mother-liquor containing 117 m*M* NADPH. The yellow color of the crystals bleached within a few minutes after addition of NADPH, equilibrated for approximately 60 minutes, rapidly transferred to Paratone N and flash frozen with liquid N_2. Single crystals of SeMet-enriched XenA [21] with nitroglycerin, TNT and metronidazole were grown via co-crystallization with 1.1 m*M* nitroglycerin, 1.1 m*M* TNT and 1.6 m*M* metronidazole respectively as previously described [22]. Data collection statistics are presented in Table 6.1 and as previously reported [22].

Table 6.1: Data Collection Statistics.

Crystal		Oxidized XenA	Reduced XenA	Oxidized XenA
Ligand		---	NADPH (117 m*M*)	Metronidazole (1.6 m*M*)
X-ray source (beamline)		SSRL (7-1)	APS (22ID)	APS (22ID)
Wavelength (Å)		1.08	1.00	1.00
Temperature (K)		100	100	100
Unit Cell (Å):	*a*	83.6	83.8	84.3
	b	157.1	155.5	158.2
	c	56.6	56.9	57.2
Resolution Range (Å)		46.9-1.92	45.9-1.51	27.1-1.73
High resolution (Å)		1.97-1.92	1.56-1.5	1.82-1.73
Total Observations		204523	2809833	477818
Unique Observations		56646	119625	71741
R_{sym} (%)[a,b]		0.062 (0.296)	0.072 (0.402)	0.082 (0.506)
$I/\sigma(I)$[a,c]		9.8 (2.4)	10.5 (2.4)	7.2 (1.5)
Completeness (%)[a]		98.4 (82.3)	86.7 (61.8)	88.2 (85.4)
Multiplicity[a]		3.7 (2.8)	5.1 (2.9)	6.7 (4.4)

[a] Numbers in parenthesis are for the highest resolution shell. [b] The average agreement between the independently measured intensities. [c] The root-mean-squared value of the intensity measurements divided by their estimated standard deviation.

All the diffraction data sets were collected at beamline 22ID of the SER-CAT facility at APS, except for oxidized XenA, which was collected at beamline 7-1 of SSRL.

Table 6.2: Model refinement statistics

Crystal	Oxidized XenA[a]	Reduced XenA 117 m*M* NADPH[a]	Oxidized XenA with 1.6 m*M* Metronidazole[a]
Temperature	100 K	100 K	100 K
Resolution range (Å)	46.9 - 1.92	45.9 - 1.51	27.1 - 1.73
No. of reflections	50901	90272	64381
R-factor	17.3	17.6	17.8
R-free[b]	23.1	21.0	22.6
No. of non-H protein atoms	6423	6508	6636
No. of residues fit	722	722	722
No. of disordered residues	2	2	2
No. of water molecules	681	744	948
No. of FMN molecules	2	2	2
Ligand molecules	2 Chloride 5 Spermine	6 Spermine	1 Metronidazole 2 Chloride
RMS deviations form ideal			
Bond lengths (Å)	0.013	0.010	0.012
Bond angles (°)	1.347	1.313	1.295
Mean B, protein atoms (Å^2)	23.3	22.6	17.5
Mean B, water molecules (Å^2)	34.7	39.4	31.3
Mean B, FMN molecules (Å^2)	23.5	21.0	17.5
Mean B, ligand molecules (Å^2)	40.7 / 48.9	45.8	37.7 / 29.8
Ramachandran analysis			
Most favored regions (%)	88.9	89.2	88.4
Additional allowed regions (%)	10.4	10.0	10.9
Generously allowed regions (%)	0.7	0.7	0.7
Disallowed regions (%)	0.0	0.2	0.0
PDB Code	To be determined	To be determined	To be determined

[a] 20m*M* Spermine tetrahydrochloride was present during crystallization. [b] Calculated with 10% of the data.

6.3.3. Crystal Structure Determination

All datasets were solved by molecular replacement in *MOLREP* [23] using oxidized XenA [1] as the search model from which the solvent molecules and FMN were removed and the *B*-factors were set to the Wilson *B* (typically about 28 Å^2). The space group is $P2_12_12$ with a = 84 ± 0.3 Å, b = 157 ± 1.0 Å, c = 57 ± 0.2 Å. Model building

was carried out with the program O [24] and refinements were with *CNS* [25-27] and/or *REFMAC5* [28]. Cross-validated, σ_A weighted $2mF_o$ - DF_c and mF_o - DF_c maps [23] were used to evaluate the model and correct errors. Water molecules were placed in the final stages of refinement with *ARP/Waters* and refined with *REFMAC5*. All other datasets were also solved by molecular replacement in *MOLREP* using the same search model. Data collection, phasing and refinement statistics for all datasets are presented in Table 6.1 and 2. Validation of the models and Ramachandran analysis were done using *SFCHECK* [29] and *PROCHECK* [30]. Secondary structure assignments were made using *KSDSSP* [31]. The RMS difference between models was calculated with CCP4 [23] or *Swiss-PDBViewer* (v3.7) [32]. Structure figures were prepared using *Swiss-PDBViewer* (v3.7), *PovRay* (v3.6), *CCP4mg* (v0.9) [33, 34] and *PyMOL* (v0.98).

6.3.4. Calculation of Theoretical Models

Docking of ligand molecules into the binding pockets of XenA and XenB was done using the *Affinity*® module of the *InsightII* (Accelrys, San Diego, California) software family. Reduced XenA and XenB structures were used for the docking experiments with either nitroglycerin, TNT, picric acid or metronidazole as ligand molecules. The crystal structure of reduced XenA reported here was used where full length chain A was supplemented with residues B355-B361 to account for a complete domain-swapped active site of XenA [1]. The crystal structure of oxidized XenB was modified by replacing the oxidized FMN with reduced FMN from XenA. Typically two or three ligand orientations within the active site were used to initiate the docking experiments, including superimposing the nitro groups of the ligand molecules with the

nitro groups of either TNT or picric acid in the active site of PETNR (1vyr [35] and 1gvr [36]).

Hydrogen atoms were added to the protein residues using a pH of 7.5 for XenA and XenB. All crystallographic waters were removed from the coordinate file; however, the protein was bathed *in silico* in a 4 Å (XenA) or 5 Å (XenB) layer of water during the ligand docking simulations. Hydrogen bond donor and acceptor atoms were defined for both the ligand and the atoms within 7 Å of the placed ligand molecule. Torsion angles for the ligand molecules for which rotations were allowed were manually defined. A Metropolis Monte Carlo simulation (MMC) [37] was performed first using the cvff force field (Consistent Valence Force Field) [38] and allowing for conformational flexibility of both the ligand molecule and the amino acid side chains within 7 Å of the ligand molecule, keeping the FMN rigid in the active site during the docking calculations. Possible binding modes of the ligand molecule were generated by energy minimization using the conjugate gradient method with non-bonding interactions calculated using a repulsive bounded quartic potential for van der Waals interactions with coulombic interactions set to zero, followed by random translation and rotation to generate a new random ligand placement. The Boltzmann factor was used as the criteria for structure acceptance [37] and was calculated using equation 1,

$$B = \exp\left[\frac{-\left(V_{new}\left(r^N\right) - V_{old}\left(r^N\right)\right)}{k_B T}\right] \qquad (1)$$

where $V(r^N)$ is the potential energy (V) of each position (r^N) for N particles in the system, k_B is the Boltzmann constant and T is the temperature. Up to twenty accepted structures were generated and the best ten were kept. Following the Metropolis Monte Carlo simulation, simulated annealing (SA) was used to refine each of the best structures. The

electrostatic interactions in the SA were calculated using the cell multipole method [39]. Finally, the ligand-receptor interaction energies for each accepted and minimized structure were calculated. In particular, the total energy of the protein-ligand complex, the energies of the protein and the ligand individually and the interaction energy between the protein and the ligand were calculated. The protein-ligand interaction energy was separated into the van der Waals and electrostatic contributions. These energies can be used to compare the docked structures to each other. However, the force field does not include desolvation terms. Affinity® also does not allow for any global conformational changes. These deficiencies must be considered when comparing energies between different ligand-receptor pairs.

6.4 Results

6.4.1. Crystal Structure of Oxidized XenA at 100 K

The structure of XenA at cryogenic conditions was determined to support direct comparisons with structures determined at 283 K, and cryogenic structures of the enzyme-metronidazole complex or NADPH reduced enzyme. The final model for oxidized XenA had an *R*-factor of 17.3% and an *R*-free of 23.1% with data between 47 – 1.92 Å resolution (Table 6.2). The typical electron density at an FMN is shown in Figure 6.1A. The 100 K and 283 K structures of XenA overlay with a r.m.s.d. of 0.22 Å using all residues in each protein (361 C_α). The largest difference between the two structures is the observation of five spermine molecules in the low temperature structure. Spermine tetrahydrachloride (20 m*M*) was present in the crystallization conditions for the structure

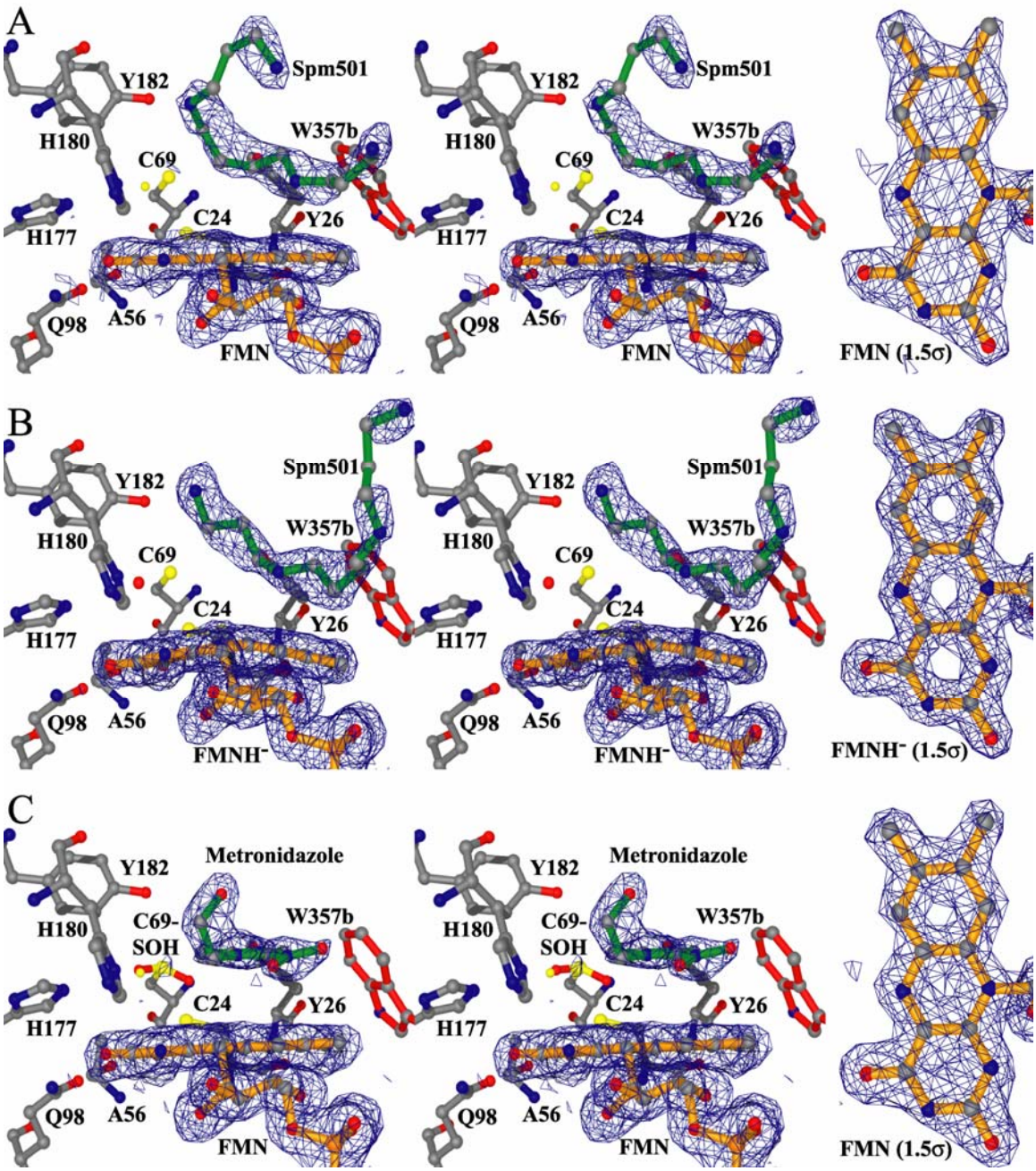

Figure 6.1: Overview of the active sites for the three crystal structures of XenA reported here. The protein residues are shown as ball and stick drawings colored by atom type, where carbon, nitrogen and oxygen are grey, blue and red, respectively. The bonds for the FMN, Trp357b, ligand molecules, spermine molecules are colored in orange, red and green, respectively. The divergent stereo drawings show 1σ contours for the $2mF_o$ - DF_c electron density maps around the flavin and ligand molecules. The stereo portion of the figure is parallel to the isoalloxazine ring. The insets show the 1.5σ contours for the $2mF_o$ - DF_c electron density maps around the flavin. (A) Oxidized XenA determined to 1.92 Å resolution at 100 K. (B), Reduced XenA at 1.51 Å resolution. (C) The XenA-metronidazole complex at 1.73 Å resolution.

determined at 283 K as well, but they were not observed in the electron density maps, presumably due to disorder at high temperature. In contrast, at low temperature the five spermine molecules fit the observed electron density with an average thermal factor of approximately 49 $Å^2$. Each active site of the XenA dimer contains an ordered spermine molecule (Spm501 and Spm502) and a chloride ion (Cl1 and Cl2). The chloride ion is located above the pyrimidine ring on the FMN *si*-face. Spermine501 and 502 are in U-shape configurations with the central portion located above the FMN dimethylbenzene rings (Figure 6.1A). They also make van der Waals contacts with Lys105, His180, Tyr182, Phe268, Trp277, Trp301, Arg325, and Trp357a/b (the domain-swapped residue in the active site). The three other spermine molecules are observed at the domain-swapped interface (Figure 6.2A and 6.2B). Spermine504 is located in a cleft created by the loop between helices α8a and α8b of chain B, with the C-terminal part of α-helix 1 of chain B, and the N-terminal part of α-helix 1 of chain A (Figure 6.2B). The cleft provides several van der Waals contacts with Arg46b, Asn34a Trp36a, Met27a, Pro351b, Pro353b, Ala90b and Ala91b. Spm504 forms hydrogen bonds with several waters molecules, but not with protein residues. The spermine 505 molecule binds to the opposite chain in the symmetry related position of Spm504. One spermine molecule, Spm503, is located at special position (½, y, ¾) where the crystallographic symmetry axis relates chain A to chain B of the domain-swapped dimer. This ligand forms three hydrogen bonds with solvent molecules and one hydrogen bond with Ala326-O. It also makes van der Waals contacts with Trp333, Phe336, Ala326 and Ala329 (Figure 6.2C). Moreover, four nearby anionic groups, two from each subunit, establish a complementary electrostatic environment to the Spm503 polyvalent cation (Figure 6.2D). The sidechains of

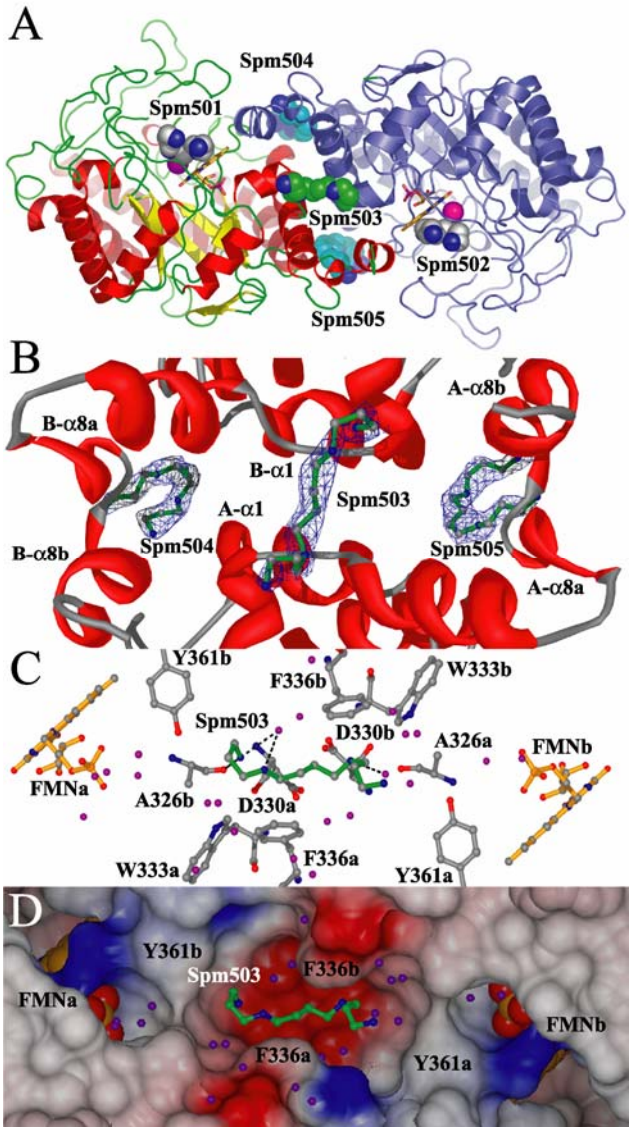

Figure 6.2: Five spermine molecules are observed in the structure of XenA at 100 K. (A) A ribbon drawing of the XenA dimer with FMN, Cl^- and spermine molecule shown. Subunit A is colored by secondary structure and subunit B is colored blue. The FMN has orange bonds, the Cl^- ions are magneta spheres, the active site spermine molecules (Spm501 and 502) are colored with grey carbon atoms, whereas the spermine ligands associated with the two-fold symmetry are colored with carbon atoms as either green (Spm503) or cyan (Spm504 & Spm505). (B) A ribbon drawing of the domain-swapped interface of XenA with the α-helices colored in red showing the spermine molecules (Spm503, 504 and 505) in green ball and stick overlayed with their 1σ contours for the $2mF_o$ - DF_c electron density maps. (C) All protein residues are represented by ball and stick and are colored by atom type. The spermine molecule is colored green and the flavin is colored orange. (D), The same view as in (C) using the same color scheme but with the FMNs drawn as spheres. All protein residues are represented by their electrostatic potential surfaces and colored with -0.5, 0, 0.5 as red, white and blue respectively.

Asp330a/b are within van der Waals contact with the Spm530-N5 and Spm503-N10 atoms, however, the FMN phosphate groups in each subunit are further away. Therefore,ionic interactions with this spermine molecule probably help stabilize the domain-swapped dimer in XenA.

6.4.2. Crystal Structure of Reduced XenA at 100 K

The atomic model of reduced XenA was refined to a final *R*-factor of 17.6 and an *R*-free of 21.0 % (Table 6.2). Figure 6.1B shows a representation of the active site σ_A weighted $2mF_o$ - DF_c density for the reduced FMN at 1.51 Å resolution. The structures of oxidized and reduced XenA overlay with a r.m.s.d. of 0.23 Å using 361 C_α. The most notable difference between the two structures is the conformation of the FMN. Whereas oxidized FMN contains a planar isoalloxazine ring, the two-electron reduced FMN shows an approximate 16º bend along the FMN N5-N10 axis. The structure accommodates the alternative FMN conformation by allowing the movement of the dimethylbenzene portion of FMN. The electron density maps indicate that the chloride ion in the oxidized structure has been replaced by a water molecule in the reduced FMN structure. This water molecule forms hydrogen bonds to His177, His180 and the N1 and N3 atoms of the FMN. There are no qualitative changes in the hydrogen bonding interactions between protein and FMN.

The active sites of the two subunits in the asymmetric unit are not identical to each other. For example, the electron density maps for subunit A of reduced XenA suggest that both Cys24 and Cys69 are oxidized to cysteine sulfenic acids (Cys-SOH). The temperature factors for the hydroxyl oxygen atoms are 33 and 31 $Å^2$ with

occupancies of 0.5 for both Cys24-SOH and Cys69-SOH, respectively (Figure 6.3A). In contrast, the electron density for subunit B suggest that Cys69 is a thiol and that Cys24 is in two conformations (Figure 6.3B). In the first conformation, the Cys24 thiol group hydrogen bonds with the O4 atom of the FMN. This contrasts with the hydrogen bonding pattern in subunit A, in which the amide nitrogen of Cys24-SOH interacts with FMN O4. Indeed, the conformation of the Cys24-SOH side chain in subunit A does not allow hydrogen bonding with the FMN-O4 atom. In the second conformation, the Cys24-SH group points toward the sulfhydryl group of Cys69; however, the 3.8 Å distance between them does not allow for a disulfide bond. Instead, Cys24-SH hydrogen bonds to the backbone nitrogen of Tyr26. Conformation one and two are modeled with occupancies of 0.6 and 0.4, respectively, and both have temperature factors of approximately 18 $Å^2$ for the side chain atoms.

Neither NADPH nor $NADP^+$ is observed in either active site of reduced XenA, but instead a spermine molecule in a U-shape configurations with the central portion located above the FMN dimethylbenzene rings is observed in both active sites (Figure 6.1B) in addition to spermine molecules located in the domain-swapped interface. The presence of spermine does not prevent soaking of NADPH into the active site to produce a reduced FMN, but no product ($NADP^+$) remains, most likely due to the low affinity of reduced FMN for $NADP^+$.

6.4.3. Crystal Structure of the Oxidized XenA-Metronidazole Complex at 100 K

Oxidized XenA was co-crystallized with 1.6 m*M* metronidazole that yielded a dataset to 1.73 Å resolution. The atomic model was refined to a final *R*-factor of 17.8%

and an *R*-free of 22.6% (Table 6.2). The structures of oxidized XenA and oxidized XenA-Metronidazole overlay with a r.m.s.d. of 0.23 Å using 361 C_α atoms. Surprisingly, spermine molecules are not observed in the structure. Figure 6.1C shows an example of the σ_A weighted $2mF_o$ - DF_c electron density for the FMN and the metronidazole in subunit A. However, differences between the active sites of the two subunits in the asymmetric unit are observed. For example, in subunit A, the metronidazole is bound parallel to the FMN *si*-face and modeled with an occupancy of 0.5. In addition, a full-occupancy chloride is located above the FMN pyrimidine ring. The nitro group from metronidazole is not positioned above the FMN N5 atom, suggesting a non-catalytic orientation. Rather the nitro group is approximately 6 Å from the FMN-N5 atom and positioned above the dimethylbenzene ring. In addition, electron density for Cys69 suggests that it is oxidized to Cys-SOH, but in two distinct conformations with occupancies of 0.5 for each. Both conformations have temperature factors of ~19 $Å^2$. In contrast, Cys24 is present in its thiol form and hydrogen bonds to the O4-FMN (Figure 6.3C).

In contrast to subunit A, neither a metronidazole ligand nor a chloride ion is observed in the active site of subunit B. Instead, the 16º bend observed in the isoalloxazine ring suggests that the FMN has been photo-reduced by the synchrotron x-ray irradiation. In addition, both Cys24 and Cys69 have been oxidized to Cys-SOH. The Cys24-SOH hydroxyl group is oriented so that it can hydrogen bond with both the N5 and O4 atoms of the FMN. This is supported by $2mF_o$-DF_c electron density connecting the Cys24-SOH with the N5 of FMN (Figure 6.3D). The temperature factor for Cys24-SOH is ~ 18 $Å^2$. Similar to that observed in NADPH reduced XenA, the Cys69-SOH

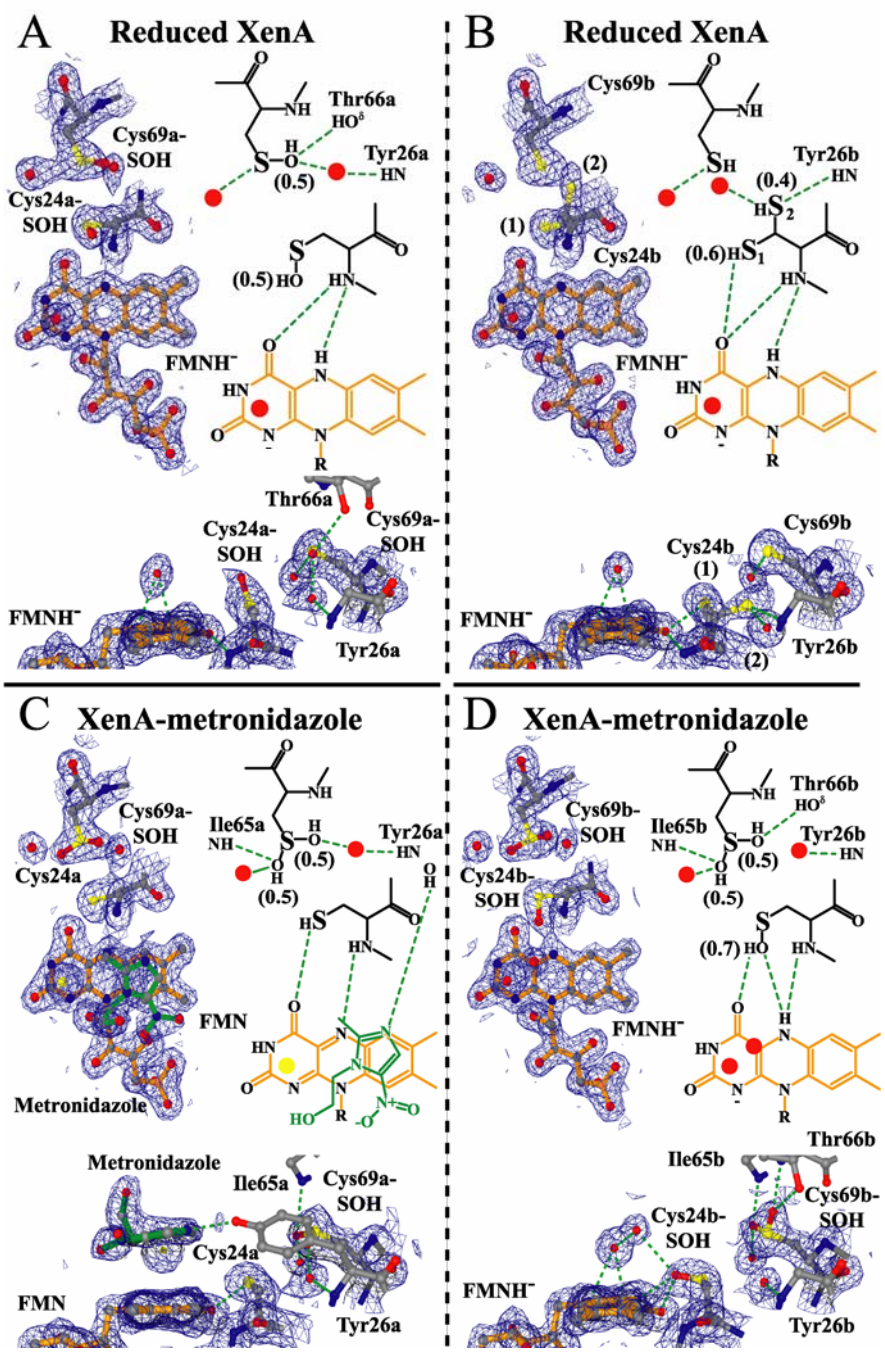

Figure 6.3: Overview of the differences occurring between the active sites cysteines of different subunits. (A), The active site cysteines of reduced XenA showing subunit A with an oxidized Cysteine-sulfenic acid (Cys69) and (B), subunit B with Cys24 portraying two distinct conformational sites. (C), The active site cysteines of native XenA complexed with metronidazole showing subunit A with an oxidized Cysteine-sulfenic acid (Cys69) in two conformations and (D), subunit B with oxidized Cysteine-sulfenic acid for Cys24 and Cys69 (two conformations).

occurs in two conformations with occupancies of 0.5 each and temperature factors of approximately 15 $Å^2$. A second dataset was collected from another oxidized XenA co-crystal with metronidazole to 1.49 Å resolution. The atomic model was refined to a final *R*-factor of 19.2% and an *R*-free of 23.4% (Supplementary Information (§6.8), Table 6.S1). However, no metronidazole was observed in either active site. Rather, the active site in subunit A is consistent with reduced FMN as can be judged from the characteristic ~ 16º bend along the FMN N5-N10 axis, accompanied by a water molecule above the pyrimidine ring (Supplementary Information (§6.8), Figure 6.S1C), while the active site in subunit B contains an oxidized FMN accompanied with a chloride ion (Supplementary Information (§6.8), Figure 6.S1D). In both active sites, Cys24 is present in its thiol form in two different conformations with partial occupancies of ~ 0.6 and ~ 0.4, while Cys69 occur as a Cys-SOH in two conformations with partial occupancies of ~ 0.5 for both conformations. Their *B*-factors are ~ 22 and ~ 24 $Å^2$ and are similar to those discussed above. In the second dataset for the XenA metronidazole complex, four spermine molecules could be placed, however, not in the active sites. They are in similar orientations as previously discussed.

6.4.4. Oxidized XenA with Nitroglycerin or TNT

Several additional ligand complexes were studied through co-crystallization of oxidized XenA, including nitroglycerin and TNT. The best dataset for XenA with 1.1 m*M* nitroglycerin diffracted to 1.8 Å resolution. The final model for this dataset refined to an *R*-factor of 19.1% and an *R*-free of 23.6% (Supplementary Information (§6.8), Table 6.S1). However, nitroglycerin was not observed in either active site. Instead, a well

defined spermine molecule (B-factors of approximately 49 $Å^2$) bind in the entrance to both active sites (Supplementary Information (§6.8), Figure 6.S1A). The best dataset for a co-crystal of oxidized XenA with 1.1 m*M* TNT diffracted to 2.1 Å resolution. The final model refined to an *R*-factor of 19.8% and an *R*-free of 25.1% (Supplementary Information (§6.8), Table 6.S1). TNT was not observed in either active site; however, the electron density maps indicated that spermine molecules occupied the active sites (Supplementary Information (§6.8), Figure 6.S1B). Consequently, in oxidized XenA crystals the 1.1 m*M* nitroglycerin and TNT ligands do not displace spermine, which is present at 20 m*M* in the crystals. Unfortunately, attempts to reduce the spermine or increase the nitroglycerin concentration in the crystallization conditions did not yield crystals suitable for high resolution diffraction studies. Oxidized XenB also failed to yield useful crystals by either co-crystallization or by soaking nitroglycerin or TNT ligands into preformed crystals. Therefore, crystal structures of nitroglycerin or TNT complexes of either XenA or XenB, albeit in the incorrect oxidation state, are not available at this time.

6.4.5. Molecular Dynamics R-NO_2 Ligand Docking to Reduced XenA and XenB

To better understand the regiospecific oxidative half-reactions of XenA and XenB, molecular dynamics ligand-docking calculations were obtained for reduced XenA and XenB with nitroglycerin, TNT, picric acid and metronidazole ligands. For XenA, the starting coordinates were based upon the crystal structures of reduced XenA and/or the oxidized XenA-metronidazole complex reported here. We also used the reduced FMN from the NADPH-reduced XenA structure to estimate a structure of reduced XenB based

on the assumption that no qualitative changes occur upon reduction of the FMN in XenB in hydrogen bonding interactions between protein and FMN or protein sidechain positions and conformations. This assumption is supported by the observation that this is indeed the case for reduction of XenA [1], OYE [13] and PETNR [15]. For these proteins, the only notable differences upon reduction are the replacement of an anion above the pyrimidine ring in the oxidized active site with a water molecule in the reduced active site and the increased butterfly bending of the isoalloxazine ring around the N5-N10 axis in the reduced form which primarily involves movement of the dimethylbenzene portion of the FMN. The electrostatic potential surface features for the FMN in oxidized XenA, reduced XenA ($FMNH^-$) and reduced XenB ($FMNH_2$) are shown in Figure 6.4. The presumed $FMNH^-$ or $FMNH_2$ species are based on the observation that XenA-Arg230 will likely stabilize the reduced anionic species, whereas XenB-His224 does not. In addition, the possibility for a $FMNH^-$ anionic species in XenA is supported by the observation of a λ_{max} at approximately 340 nm in the optical spectra of NADPH reduced XenA [2] and is indicative of an anionic reduced FMN [40]. To reduce potential bias, a number of starting R-NO_2 ligand orientations were explored, as discussed in the methods section above. The binding pocket was defined as comprised of all atoms within 7 Å of the ligand complex and was allowed to vary during the molecular dynamics simulations. A Monte Carlo simulation was performed first, from which at most ten structures were subjected to simulated annealing. The family of protein-ligand structures were ranked by relative total energy among the family members to yield the best docked conformations. Figure 6.5 show the best model obtained for 1,2,3-trinitroglycerin (TNG) and the other nitroester isomers in the active sites of XenA and

XenB. Ligand complexes for reduced XenA and XenB with TNT, picric acid and metronidazole are shown in Figure 6.6. Several overlays of the two enzyme-ligand complexes are shown in Figure 6.7, which permit direct comparisons of the results.

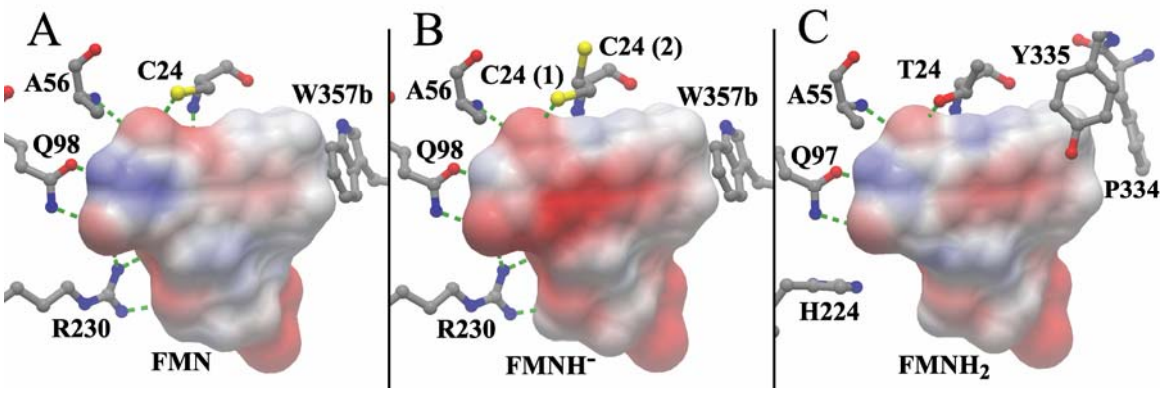

Figure 6.4: The electrostatic potential mapped onto the solvent exposed surfaces of FMN in oxidized XenA (A), $FMNH^-$ in reduced XenA (B) and $FMNH_2$ in oxidized XenB (C). The solvent exposed surface was determined with a 1.4 A probe radius and colored according to Poisson-Boltzmann electrostatic potential from red (-0.5) to blue (0.5). The protein residues are shown as ball and stick with C, N, O and S colored grey, blue, red and yellow respectively. Hydrogen bonds are drawn as green dotted lines.

TNG bound to reduced XenA and XenB occurs above the *si*-face of the FMN, and is stabilized by numerous protein-ligand hydrogen bonds in each case (Figure 6.5A and 6.5D). For example, XenA binds TNG in the active site so that a terminal nitro group is approximately 3.2 Å from the FMN-N5 atom. This conformation is stabilized by hydrogen bonds between every nitro group and several active site residues. Consequently, one of the terminal nitro groups is ideally positioned for elimination. In contrast, reduced XenB binds TNG with the C2 nitro group located nearest the C4a of the flavin, and only 3.5 Å separation between the ligand and the isoalloxazine ring. Therefore, the ligand orientation in XenB appears ideal for elimination of the internal

nitro group from TNG. Thus the predicted models correlate perfectly with the kinetic preferences observed by steady-state turnover of TNG by each enzyme.

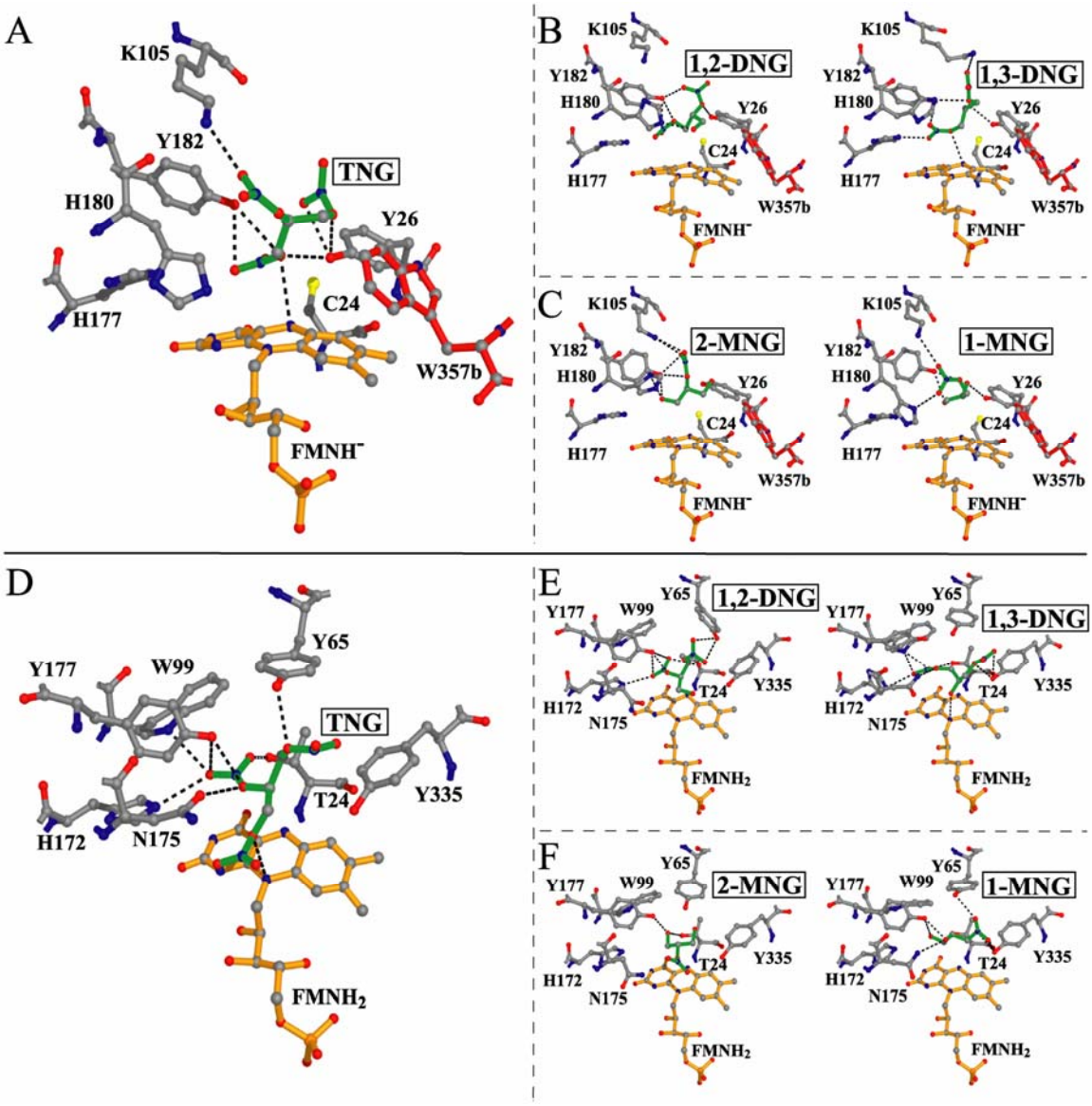

Figure 6.5: Overview of the active sites of calculated structures for reduced XenA and XenB with nitroglycerin isomers. All protein residues are shown as ball and stick drawings colored by atom type. The FMN, Trp357b and nitroglycerin are colored in orange, red and green, respectively. Hydrogen bonds between ligand and protein are indicated as dotted black lines. (A) Reduced XenA with TNG; (B) reduced XenA with 1,2-DNG and 1,3-DNG; (C) reduced XenA with 1-MNG and 2-MNG; (D) reduced XenB with TNG; (E) reduced XenB with 1,2-DNG and 1,3-DNG; (F) reduced XenB with 1-MNG and 2-MNG.

Theoretical models were also calculated for 1,2-dinitroglycerin (1,2-DNG), 1,3-dinitroglycerin (1,3-DNG), 1-mononitroglycerin (1-MNG) and 2-mononitroglycerin (2-MNG) with XenA (Figure 6.5B and 6.5C) or XenB (Figure 6.5E and 6.5F). These ligands represent the products of nitrite elimination from TNG by either enzyme and are also slower substrates for NADPH-dependent nitrite elimination [2]. In every case there are several protein-ligand hydrogen bonds, but most often there are fewer than predicted in the TNG complexes. The predicted models are also consistent with the observed regiospecific reactions of the two enzymes. For example, XenA is likely to bind 1,3-DNG better than 1,2-DNG as deduced by a larger number of predicted hydrogen bonds in the former than the latter complex (Figure 6.5B). The theoretical models calculated for XenA with 1-mononitroglycerin or 2-mononitroglycerin predict fewer protein-ligand hydrogen bonds, but also yield larger distances between the R-NO_2 group and the FMN N5 atom (>4Å). Moreover, the nitro group points away from the flavin, and consequently, the models suggest that the reduced enzymes will not bind the ligands to promote nitrite elimination (Figure 6.5C). Models calculated for XenB with 1,2-DNG and 1,3-DNG also yield ligand conformations that are stabilized by numerous hydrogen bonds. However, only the XenB complex with 1,2-DNG yields an orientation with the C2 nitro group above the C4a of the FMN, which suggests a reactive complex (Figure 6.5E). Finally, ligand complexes calculated for XenB with 1-MNG and 2-MNG also show the ligand molecule located greater than 4 Å above the *si*-face of the flavin ring, and the nitro group points away from the FMN-N5 atom (Figure 6.5F). Together, all the molecular dynamics binding models are remarkably consistent with the regiospecific reactions observed for each enzyme by steady state assays *in vitro*.

As shown in Figure 6.6, reduced XenB binds TNT, picric acid and metronidazole approximately parallel to the FMN to a larger degree than does XenA. For example, the XenB-TNT complex shows that every TNT ligand orientation in the active site is nearly parallel to the FMN ring (Figure 6.6B). In contrast, the XenA-TNT complexes reveal that most of the time, the TNT ligands bind almost perpendicular to the FMN. Indeed, only a minority of the XenA-TNT complexes yield a ligand more parallel to the FMN (Figure 6.6A). Moreover, each orientation of TNT in the XenB active site places a nitro group approximately 3.7 Å from the FMN-N5 atom, and approximately 3.3 Å from the nearest aromatic carbon. Consequently, XenB should reduce either the nitro group or the aromatic ring of TNT with similar capacity and much more readily than XenA. This is in fact what is observed by steady state assays *in vitro*.

Picric acid is predicted to form similar complexes as obtained with TNT for both reduced XenA and XenB (Figure 6.6C and 6.6D). This result is consistent with the observation that picric acid is a substrate for the oxidative half-reaction, but reacts at different rates with both enzymes (B. G. Fox, personal communication). These types of parallel aromatic ligand-flavin orientations also suggest that they should elicit a charge-transfer transition at long-wavelength that derives from the electron rich ligand and the oxidized isoalloxazine ring within the enzyme. The *p*-chlorophenol complex with oxidized XenA does, indeed yield such a spectrum (Figure 6.8). Thus the molecular dynamics simulations have spectroscopic support as well as nearly complete correlation with catalytic studies [2, 4].

The molecular dynamics simulations show that reduced XenA binds metronidazole approximately 4 Å above the *si*-face of the FMN and hydrogen bonds with

Lys105, Tyr26 and Tyr182. (Figure 6.6E). The lowest-energy conformation (Figure 6.7E, red) places the nitro group 5.8 Å away from the FMN-N5 atom and pointing toward the His180-C_α atom. In crystal structure for the oxidized XenA-metronidazole complex, the ligand molecule is located approximately parallel to the FMN, but is only about 3 Å away. However, the nitro group is located ~ 5.5 Å from the FMN-N5 atom suggesting it is too far away for reaction. Therefore, neither the crystal structure nor the docked conformations are likely mimics of a complex that yields R-NO_2 reduction. The predicted lowest-energy structure for the reduced XenB-metronidazole complex also places the ligand approximately 4.5 Å above the FMN, where it is predicted to hydrogen bond with the side chains of Thr24, Asn175 and Tyr335 (Figure 6.6F). The nitro group is approximately 6.5 Å away from the FMN-N5 atom, but is orientated away from the FMN (Figure 6.6F and 6.7D, blue) Consequently, this conformation is not likely to result in nitro group reduction either. However, a reasonable conformation that reflects a catalytically relevant complex for both XenA (Figure 6.7E, green) and XenB by molecular dynamics simulations is less than 5% higher in energy than the ground-state structures. These structures place the R-NO_2 moiety only 3.5 Å from the FMN-N5 atom and are stabilized by hydrogen bonding with the side chains of Cys24, Tyr182 and the His180-O and FMN-N5 atoms in XenA and the sidechains of Thr24, Asn175 and Tyr335 in XenB. Thus the second-lowest energy conformers appear to mimic complexes that could provide the sensitivity phenotype observed by *in vivo* assays with whole cells expressing either XenA or XenB (B.G. Fox, personal communication).

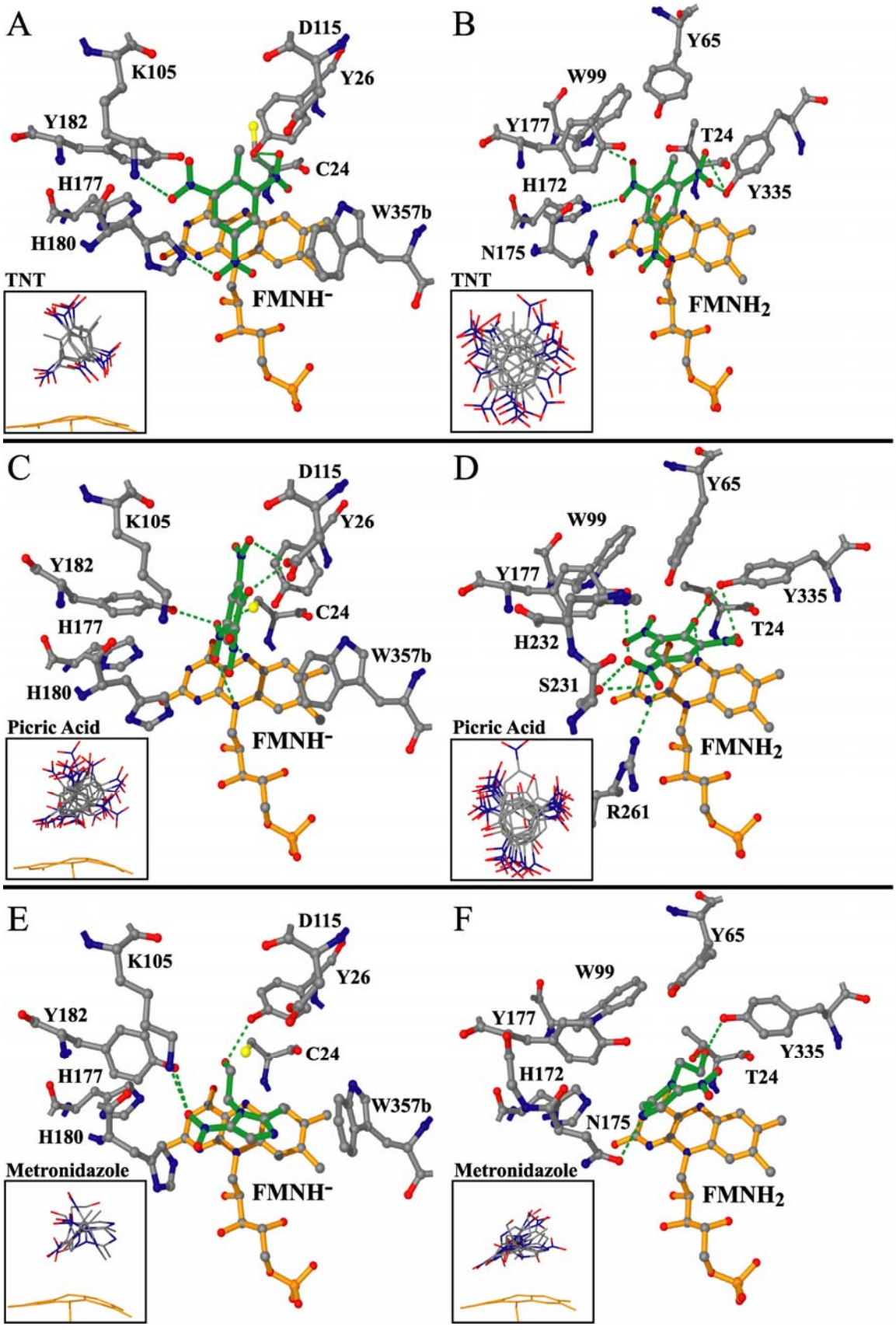
A
D115
K105
Y26
Y182
C24
H177
W357b
H180
TNT
FMNH-
B
Y65
W99
Y177
T24
H172
Y335
N175
TNT
FMNH2
C
D115
K105
Y26
Y182
C24
H177
W357b
H180
Picric Acid
FMNH-
D
Y65
W99
Y177
Y335
T24
H232
S231
Picric Acid
FMNH2
R261
E
D115
K105
Y26
Y182
C24
H177
W357b
H180
Metronidazole
FMNH-
F
Y65
W99
Y177
Y335
H172
T24
N175
Metronidazole
FMNH2

Figure 6.6: Overview of protein-ligand interactions for TNT, picric acid and metronidazole complexes with reduced XenA and XenB. All protein residues are shown as ball and stick drawings colored by atom type. The FMN and ligand molecules are colored in orange and green, respectively. Hydrogen bonds between ligand and protein are indicated as dotted green lines. The insets in each figure shows all conformations calculated for each ligand complex in a view approximately parallel to the isoalloxazine ring, with the exception of B and D, which are shown as perpendicular views. (A) Reduced XenA with TNT; (B) Reduced XenB with TNT; (C) Reduced XenA with picric acid; (D) Reduced XenB with picric acid; (E) Reduced XenA with metronidazole; (F) Reduced XenB with metronidazole.

6.5 Discussion

6.5.1. Oxidized Versus Reduced XenA and XenB

The FMN binds to the C-terminal end of the $(\beta/\alpha)_8$ barrel structural motif in both XenA and XenB. The *si*-face is exposed to bulk solvent and the electron density for the oxidized isoalloxazine ring yields a planar ring system in each case. However, after reduction, the ring system in XenA exhibits a 16º bend along the N5-N10 axis (Figure 6.1B). Similar alterations are observed for several homologs, including OYE (15º, 1oyc, [13]), PETNR (12º, 1h63, [15]) and YqjM (10º, 1z48, [41]) and most likely XenB as well. There are almost no observable hydrogen bonding differences between the oxidized and reduced structures of XenA. The guanidino group of XenA-Arg230 is only 2.9 Å from the FMN-N1 atom, where the positive charge likely stabilizes the anionic $FMNH^-$ species (Figure 6.4B). In contrast, XenB-His224, which is structurally analogous to XenA-Arg230, does not likely provide equivalent stabilization of an anion (Figure 6.4C). Consequently, a neutral $FMNH_2$ species is predicted in reduced XenB, which highlights an important difference in the active site electronic environment of the two homologs.

Small changes aroung the FMN do occur in addition to major changes such as the 16º bend along the N5-N10 axis and the replacement of a chloride ion for a water molecule. In XenA, the Cys24-SH and Ala56-NH atoms hydrogen bond to the FMN-O4 atom, whereas the Cys24-NH atom hydrogen bonds to the FMN-N5 atom. Analogous protein-FMN interactions are formed in XenB by Thr24-OH, Ala55-NH and Thr24-NH. The FMN ribityl chain in XenA is anchored by interactions with main chain atoms of Pro22 and sidechain atoms of Arg230 and Trp301. The Pro22-O atom is approximately equidistant to the FMN-N5 (3.3 Å) and FMN-N1 (3.4 Å) atoms. However, as a result of the bend along the FMN N5-N10 axis after FMN reduction, the FMN-N5 and FMN-N1 atoms are 3.7 Å and 3.3 Å from the Pro22-O atom, respectively, potentially providing additional stabilization to the reduced FMN. Similar subtle changes are anticipated in the structure of XenB.

Another striking difference between XenA and other homologous, with the exception of YqjM, is that the XenA-FMN-O4 atom does not hydrogen bond to a threonine residue, but rather to Cys24 instead. Adjacent to XenA-Cys24 is Cys69; however, the distance between the two thiol groups (4.5 - 4.7 Å in the oxidized dataset at 100 K) is too large to form a disulfide bond. In the structure of NADPH reduced XenA, the electron density for Cys24 in subunit B suggests that it adopts two conformations, each with partial occupancy of 0.5 (Figure 6.3B). The thiol group in the first conformation likely forms hydrogen bonds with the FMN-O4 atom (2.9 Å) and the FMN-N5 atom (3.6 Å). In contrast, the Cys24-SH atom in the second conformation is toward the Cys69-SH atom and the side chain of Tyr26. In all the molecular dynamics simulations, XenA-Cys24 adopts the latter conformation with the thiol group toward the

Cys69-SH atom, but the distance remains to large to form a disulfide bond. In contrast, the electron density for both these cysteine residues in subunit A is consistent with oxidation to cysteine sulfenic acids (Cys-SOH) with occupancies of 0.5. Moreover, a potential second orientation of Cys24-SOH could allow for a hydrogen bond to Cys69-SOH at a distance of apprimately 2.5 Å (data not shown). Reduced FMN is capable of reacting with molecular oxygen at the FMN-C4a atom. Typically, molecular oxygen is present in the aqueous solutions at approximately 280 μ*M*. In the absence of a suitable R-NO_2 or organic substrate molecules for the oxidative half-reaction, the reduced flavin in XenA and XenB reacts slowly with O_2 to produce hydrogen peroxide (H_2O_2) [2]. Hydrogen peroxide is a reactive oxygen intermediate and often oxidizes metal centers and/or amino acid side chain residues in many proteins [42-48]. However, the thiolate moiety from a deprotonated cysteine residue is particularly susceptible to oxidation to the sulfenic acid (Cys-SOH), cysteine-sulfenic acid (Cys-SOH) or cystein-sulfonic acid (Cys-SO_3H) states [42, 48]. Thus in several structures of XenA, Cys24 and Cys69 appear to be oxidized by H_2O_2 generated *in situ* by reaction with $FMNH^-$ generated by either incubation with NADPH or by photoreduction via X-ray irradiation.

6.5.2. Ligand Binding to Oxidized and Reduced XenA

In order to prevent turnover, oxidized XenA was co-crystallized with a variety of substrate molecules for the oxidative half-reaction. However, in all but the metronidazole complex, spermine was observed in the active site, rather than the ligand utilized for the co-crystallization. The refined XenA structures suggest a rationale for the requirement to include spermine in the crystallization buffers since it also stabilizes several crystal

contacts. Thus multiple spermine ligands are found in cryogenic crystals of XenA including oxidized and reduced XenA, and co-crystals with TNG and TNT, but not in the oxidized XenA-metronidazole co-crystal. Most often, the XenA active site entrance is almost completely blocked by spermine, which thus prevents access of most of the R-NO_2 molecules. Moreover, the active site spermine molecules (Spm501 or Spm502) bury more than 71% (~21 $Å^2$) of the FMN solvent exposed surface area compared to the ligand-free active sites. Nevertheless, metronidazole is able to bind to at least one of the oxidized active sites in XenA, despite the presence of spermine in the crystallization conditions. However, the orientation of the metronidazole R-NO_2 group with respect to the FMN-N5 atom suggests that the observed complex does not mimic a potentially reactive species. The R-NO_2 nitrogen atom is located 5.6 Å from the FMN-N5 atom and is pointing toward the FMN ribityl chain with its imidazole ring located above the dimethylbenzene ring (Figure 6.1C and 6.3C). Indeed, the molecular dynamics simulations yield several alternative orientations with reduced XenA and some of these mimic the conformation necessary to yield catalysis. For example, approximately half of the structures calculated for reduced XenA with metronidazole place the R-NO_2 group in close proximity to the FMN-N5 atom (3.5 – 3.9 Å), which would be expected to facilitate hydride transfer between the $FMNH^-$ species and the metronidazole (Figure 6.6E, inset).

6.5.3. Regiospecific Elimination of Nitrite from Nitroglycerin by XenA and XenB

To explore the structural basis of the regiospecific transformations observed for XenA and XenB with respect to nitroglycerin [2], a series of molecular dynamics models of reduced XenA or XenB with either nitroglycerin (Figure 6.5A and 6.5D), 1,2- or 1,3-

ditroglycerin (Figure 6.5B and 6.5E), and 1- or 2-nitroglycerin (Figure 6.5C and 6.5F) were evaluated. The reactive intermediate, which is intractable for crystallographic analysis, most likely facilitates reductive nitrite elimination via hydride transfer from the reduced FMN-N5 atom position to the R-NO_2 substrate. Thus we anticipate that a hydride attacks the nitrogen atom of the nitro group on the nitroester substrate (R-O-NO_2), resulting in release of nitrite, R-OH and the regeneration of the oxidized flavin. To mimic the catalytic complex therefore, these atoms must be in close proximity in one or more of the final molecular dynamics simulation models. As described in the following paragraphs, our molecular dynamics simulations suggest that structural differences between XenA and XenB influence ligand binding in the active site and correlate with the regiospecific kinetic bias exhibited by the two enzymes.

Steady-state kinetic analysis demonstrates that XenA exhibits a kinetic preference for elimination of a terminal nitro group, rather than the C2 nitro group [2]. For example, XenA produces approximately 2-fold molar excess of 1,2-DNG relative to 1,3-DNG, and nitrite elimination of 1,2-DNG shows 1.3-fold selectivity for a terminal nitro group. In the ten-best structures obtained for the reduced XenA-TNG complex, eight of them placed a terminal nitro group in an appropriate location to promote nitrite elimination. Moreover, these conformers all differed by only approximately 12% in their calculated energy. Only two of the ten structures resulted in the C2 nitro group nearest the reduced FMN-N5 atom moiety. Similar results were obtained for the two isomers of DNG bound to reduced XenA; seven out of ten structures yield a terminal nitro group above the flavin. However, neither the 1- or 2-nitroglycerol complexes resulted in a catalytically

relevant complex (Figure 6.5C), which is consistent with both isomers failing to serve as substrates for the oxidative half-reaction under steady-state conditions.

XenB exhibits selectivity for removal of C2 nitro group by 4.6- and 2.4-fold from nitroglycerin and 1,2-DNG, respectively. The structural basis for the selectivity bias is not as clearly established by the XenB molecular dynamics simulations compared to XenA. We anticipate that the more accessible active site environment of XenB and neutral $FMNH_2$ species in the reduced enzyme are at least partially responsible. The calculations for nitroglycerin complexes with XenB resulted in eight docked conformations with energies that differed by less than 19%. Three of the best eight nitroglycerin conformations place the C2 nitro group above the FMN-N5 atom (Figure 6.5D), whereas the other five conformations place a terminal nitro group in close proximity to the FMN-N5 atom. Similarly, seven conformations of 1,2-DNG bound to XenB differed by less than 7% in energy, and two of these have the C2 nitro group nearest the FMN-N5 atom (Figure 6.5E). The XenB models with 1-MNG and 2-MNG revealed both ligands in an unproductive binding mode similar to the analogous complexes with XenA (Figure 6.5F).

6.5.4. Regiospecific Reduction of TNT or Picric Acid by XenA and XenB

Reduction of the aromatic ring or one of the nitro groups of TNT, presumably by hydride transfer, yields a variety of products and has been documented by both XenA and XenB [3, 4]. For example, both enzymes will reduce the aromatic ring of TNT by two or four electrons, although XenB shows five times higher specific activity than XenA. Similarly, XenB also reduces the nitro group of TNT to a greater extent than XenA. The

molecular dynamics simulations for TNT complexes with reduced XenB resulted in nine structures with energies that differed by no more than 2%. These models show TNT bound in an orientation with the aromatic ring approximately parallel to the isoalloxazine ring. They differ by a rotation about the normal of the TNT aromatic ring with respect to the FMN isoalloxazine ring. An overlay of these structures yields an image in which a nitro group is distributed in almost every direction about the centrally-located aromatic ring (Figure 6.6B, inset). Consequently, the nine models of TNT bound to XenB all have either a nitro group or an aromatic carbon atom approximately 3 Å above the redox-active FMN-N5 atom position. Thus the molecular dynamics models illustrate XenB readily reduces both the aromatic ring and R-NO_2 groups of TNT. In addition, models calculated for XenB with picric acid show comparable results as TNT, suggesting that similar reactions should be observed with this substrate (Figure 6.6D, inset).

A very different situation is obtained for reduced XenA with TNT or picric acid, where the five best TNT structures differed by less than 4.5% in energy. In contrast to XenB, none of these models place the TNT aromatic ring parallel to the FMN isoalloxazine ring, but rather yield more perpendicular arrangements (Figure 6.6A, inset). The average distance from FMN-N5 atom to the nearest reactive atom on TNT is $\geq$ 3.6 Å, and is most often an aromatic ring carbon. The greater distance and orientation of the TNT ligand within the XenA active site rationalizes the lower activity XenA with TNT compared to XenB. Moreover, a nitro group is almost always placed in a distinct binding site in XenA with hydrogen bonds to the side chains of Lys105 and His180, and the other nitro groups frequently hydrogen bond with the side chains of Tyr26, Tyr182, Trp357b and/or the FMN-N5 atom. Indeed, as a family, the nitro groups from TNT or

nitroglycerin are always located in equivalent XenA binding sites with hydrogen bonds to one or more of these residues. However, the hydrogen bonds with Lys105 are almost always satisfied in the models. Since this residue is further from the FMN, it appears to be a major determining factor for which of the remaining nitro groups can be presented to the flavin for reaction. Moreover, hydrogen bonds with Tyr182 also position a nitro group near the FMN-N5 atom, which will enhance nitrite elimination from nitroester substrates. Models calculated for XenA with picric acid show comparable results as the XenA models with TNT.

6.5.5. Metronidazole Complexes with XenA and XenB

Molecular dynamics models calculated for reduced XenA with metronidazole resulted in the five best structures that differed by less than 5% in energy. The ligand conformation is very different in each structure (Figure 6.6E, inset), and two models place the nitro group within approximately 4 Å of the FMN-N5 atom. In almost all of the models, hydrogen bonds are suggested with the side chains of Lys105, Tyr182 and Cys24 and/or Tyr26. The simulations suggest that the lowest-energy configuration places metronidazole almost parallel with the FMN dimethylbenzene ring (Figure 6.6E) and is stabilized by several hydrogen bonds. The next model is only 0.5% higher in energy and is quite similar to the perpendicular complexes obtained with TNT and picric acid (Figure 6.7E, green). However, in the latter conformation, the metronidazole nitro group hydrogen bonds to the FMN-N5 atom as well as the Cys24-SH atom. Therefore, we anticipate that this represents the reactive complex because of the proper orientation of the FMN and nitro group. However, the lowest-energy conformation correlates

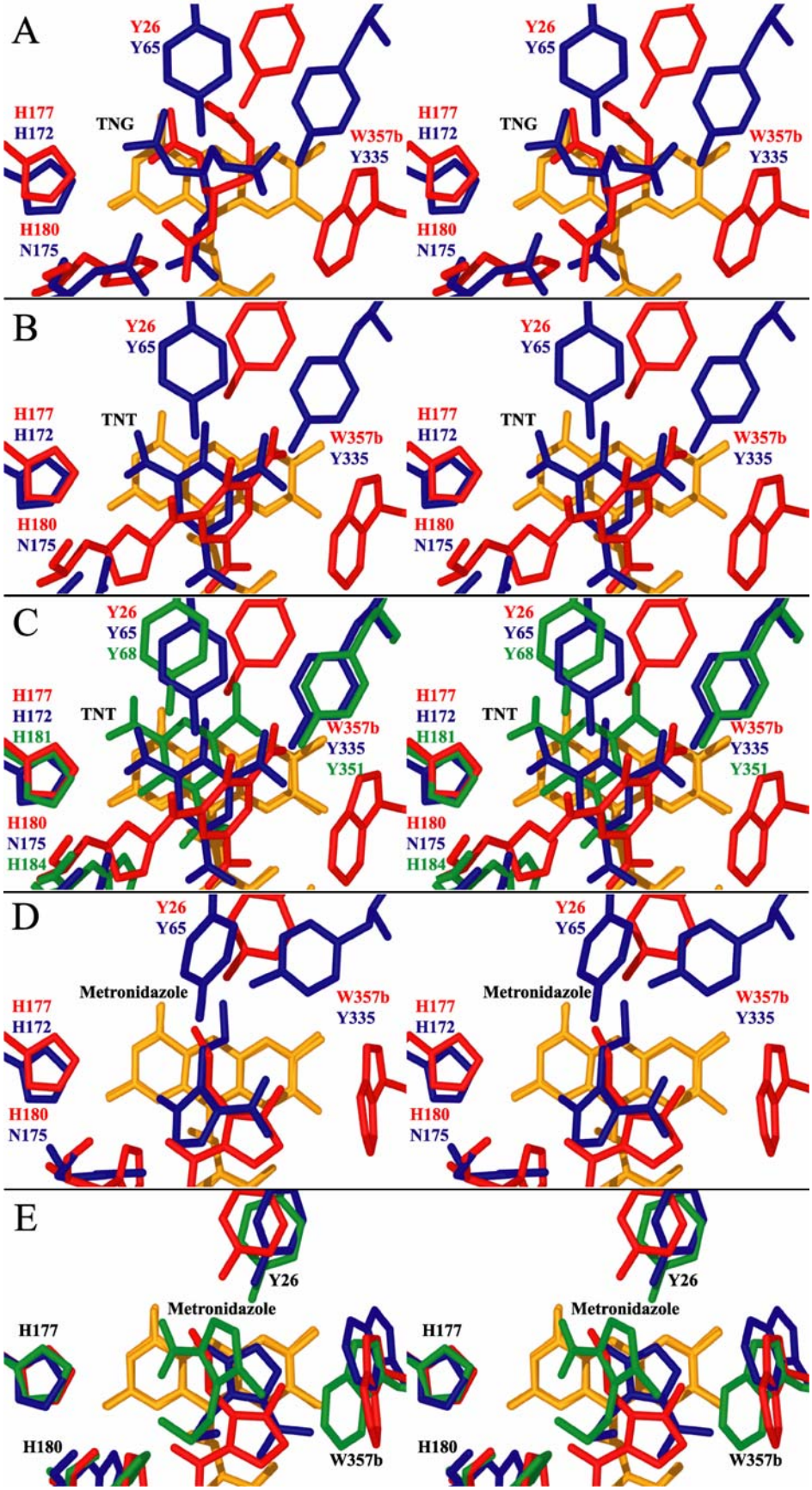
A
Y26
Y65
H177
H172
TNG
W357b
Y335
H180
N175
B
TNT
C
Y68
H181
Y351
H184
D
Metronidazole
E

Figure 6.7: Comparison of ligand conformations in calculated structures for reduced XenA and reduced XenB with nitroglycerin (A), TNT (B and C) and metronidazole (D and E). All residues, FMN molecules and ligand molecules are drawn as sticks where residues are colored red for lowest-energy calculated structures of XenA (A-E), blue for lowest-energy calculated structures of XenB (A-D) or the crystal structure of XenA•metronidazole (E) and green for the crystal structure of PETNR (C) or the second-lowest, catalytically relevant calculated structure for XenA •metronidazole (E). FMN molecules are always colored orange and the ligand molecule is colored the same as the residues. The structures shown in Figures A, B, and D are identical to Figure 6.5A&D, Figure 6.6A&B and Figure 6.6E&F for XenA and XenB respectively.

reasonably well with the crystal structure of the oxidized XenA-metronidazole complex. Consequently, we anticipate that the ground-state molecular dynamics model (Figure 6.7E, red) and the crystal structure configuration (Figure 6.7, blue) probably represent inactive complexes. On the other hand, the structures show that the smaller ring in metronidazole can adopt a nearly parallel arrangement between the ligand and the FMN.

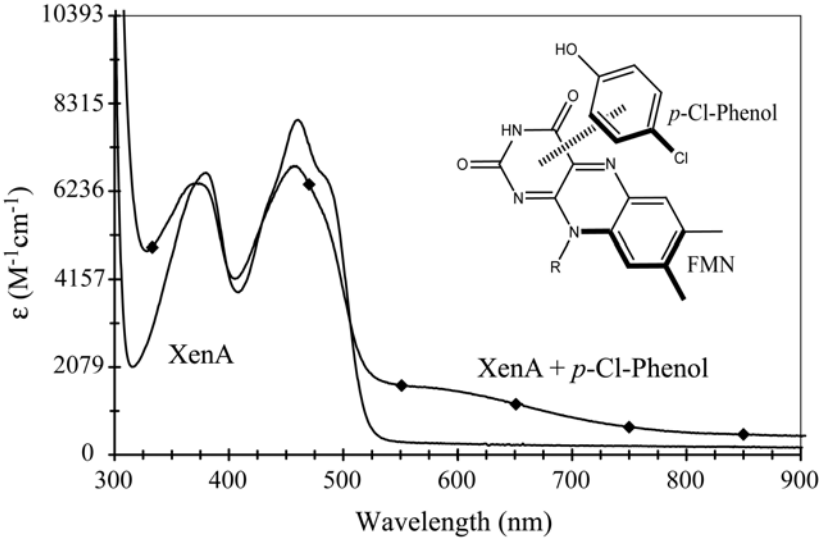

Figure 6.8: The optical spectrum of 20 μM oxidized XenA in 50 mM MOPS buffer, pH 7, and after addition of 50 mM *p*-Cl-phenol.

This correlates with the observation that ligands such as *p*-Cl- and *p*-Br-phenol do form charge-transfer complexes with XenA (Figure 6.8) and support one or more parallel ligand binding modes. Similar to the XenA results, the ten-best complexes obtained with XenB bound to metronidazole often reflect potentially inactive configurations. However, at least one places the nitro group in an active configuration, within hydrogen bonding to Thr24, Tyr335 and the FMN-N5 atom.

6.6 Conclusion

Molecular dynamics calculations were carried out for reduced XenA and XenB with a variety of ligand complexes, such as TNG, TNT, picric acid and metronidazole. The resulting energy-minimized structures for XenA and XenB with these ligand molecules show differing preferences for hydrogen bonding in the active sites of these proteins. XenA prefers to satisfy hydrogen bonds with Tyr26, Lys105 and Tyr182. These are residues located above the *si*-face of the flavin. The equivalent residues in XenB do not appear to be involved in ligand binding for XenB (Cys26, Ile104 and Tyr177). Instead, XenB prefers to satisfy hydrogen bonds with Thr24, Tyr177 and Tyr335, which are residues that can be found flanking the flavin ring. As a result, the binding conformations for ligand molecules that are catalytically relevant are different for XenA and XenB. Their differing pattern of hydrogen bonding with ligand molecules is suggestive of the formation of different binding pockets for nitro groups in XenA and XenB that would result in differing selectivities and catalysis for identical ligand molecules.

6.7 Acknowledgements

This work was supported in part by the Georgia Tech Research Corporation and the Office of the Vice Provost for Research, Georgia Institute of Technology, an American Chemical Society Petroleum Research Fund type G grant (40310-G4) and an American Heart Association Grant in Aid (0555286B) to A.M.O. and with a grant from the National Science Foundation (MCB-9733734) to B.G.F. Portions of this research were carried out at the Stanford Synchrotron Radiation Laboratory (SSRL), operated by the US Department of Energy, Office of Basic Energy Sciences. The SSRL Structural Molecular Biology Program is supported by the Department of Energy, Office of Biological and Environmental Research an by the National Institutes of Health, National Center for Research Resources, Biomedical Technology Program and the National Institute of General Medical Sciences. Portions of this work were also carried out at beamline 22-ID in the SER-CAT facilities at the Advanced Photon Source (APS). The use of APS is supported by the US Department of Energy, Basic Energy Sciences, Office of Science under Contract No. W-31-109-Eng-38.

The atomic coordinates and structure factors have been deposited to the Protein Data Bank with the corresponding file names (to be determinedill in when available).

6.8 Supplementary Information

Table 6.S1: Data Collections and Model Refinement Statistics

Data Collections Statistics			
Ligand	Oxidized XenA TNG (1.1 m*M*)	Oxidized XenA TNT (1.1 m*M*)	Oxidized XenA Metronidazole (1.6 m*M*)
X-ray source (beamline)	APS (22ID)	APS (22ID)	APS (22ID)
Wavelength (Å)	1.00	1.0332	0.99997
Temperature (K)	100	100	100
Unit Cell (Å): *a*	84.2	84.2	83.7
b	158.1	158.2	157.3
c	57.3	57.0	56.9
Resolution Range (Å)	27.7-1.8	31.1-2.1	46.1-1.5
High resolution (Å)	1.90-1.8	2.21-2.10	1.59-1.49
Total Observations	287037	254961	236178
Unique Observations	63499	43637	120908
R_{sym} (%)[a,b]	6.8 (48.2)	11.1 (49.2)	8.3 (0.45)
$I/\sigma(I)$[a,c]	6.7 (1.5)	5.6 (1.5)	8.8 (1.3)
Completeness (%)[a]	90.0 (86.8)	93.2 (69.1)	80.6 (44.4)
Multiplicity[a]	4.6 (4.1)	6.1 (3.0)	7.2 (1.5)
Model Refinement Statistics			
No. of reflections	57030	35483	91939
R-factor	19.1	19.8	19.2
R-free[b]	23.5	25.1	23.4
No. of non-H protein atoms	6355	6080	6650
No. of residues fit	722	722	722
No. of disordered residues	2	2	2
No. of water molecules	599	362	918
No. of FMN molecules	2	2	2
Ligand molecules	2 Chloride 6 Spermine	2 Chloride 3 Spermine	1 Chloride 4 Spermine
RMS deviations form ideal			
Bond lengths (Å)	0.010	0.012	0.010
Bond angles (°)	1.156	1.349	1.267
Mean B, protein atoms ($Å^2$)	20.6	21.2	22.1
Mean B, water molecules ($Å^2$)	31.3	21.9	35.8
Mean B, FMN molecules ($Å^2$)	20.0	22.3	21.6
Mean B, ligand molecules ($Å^2$)	38.7 / 46.8	38.1 / 50.4	33.6 / 53.3
Ramachandran analysis			
Most favored regions (%)	89.3	88.4	89.4
Additional allowed regions (%)	9.9	10.9	9.8
Generously allowed regions (%)	0.8	0.7	0.8
Disallowed regions (%)	0.0	0.0	0.0

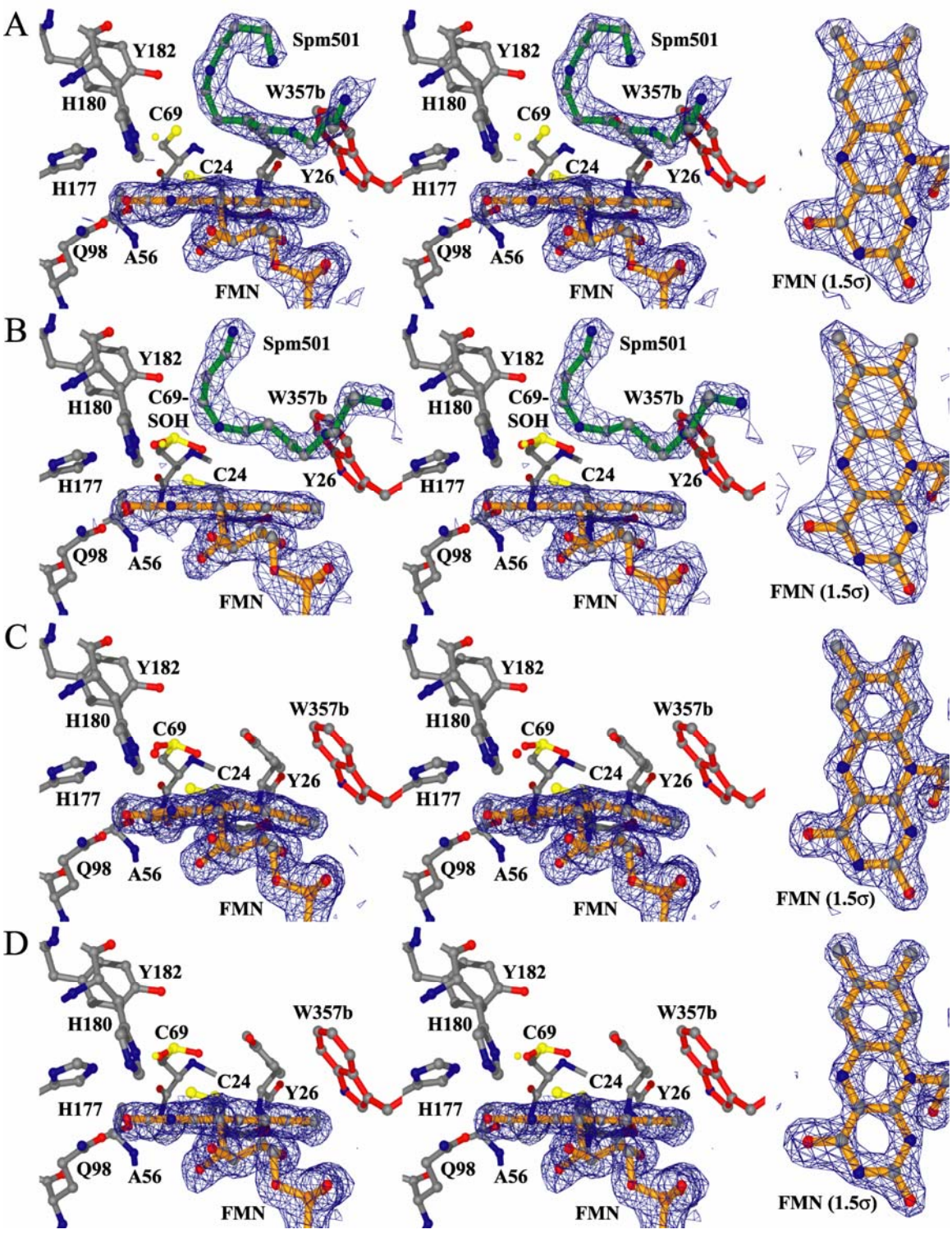

Figure 6.S1: Overview of the active sites for the two crystal structures of XenA co-crystallized with TNG, TNT and metronidazole. The protein residues are shown as ball and stick drawings colored by atom type, where carbon, nitrogen and oxygen are grey, blue and red, respectively. The bonds for the FMN, Trp357b, ligand molecules, spermine molecules is colored in orange, red and green, respectively. The divergent stereo

drawings show 1σ contours for the $2mF_o$ - DF_c electron density maps around the flavin and ligand molecules. The stereo portion of the figure is parallel to the isoalloxazine ring. The insets show the 1.5σ contours for the $2mF_o$ - DF_c electron density maps around the flavin. (A) Oxidized XenA co-crystallized with 1.1m*M* TNG determined to 1.8 Å resolution at 100 K. (B), Oxidized XenA co-crystallized with 1.1m*M* TNT determined to 2.1 Å resolution at 100 K. (C) Oxidized XenA co-crystallized with 1.6 m*M* metronidazole to 1.5 Å resolution at 100 K for active site A (C) and active site B (D) In none of these datasets was the ligand molecule observed. Instead, spermine was found in the active sites and was present at 20 m*M* in the crystallization buffer except in the case of XenA co-crystallized with metronidazole.

6.9 References

1. Manning, L., D.S. Blehert, J.M. Studts, G.H. Chambliss, B.G. Fox, and A.M. Orville, *Crystal structures of xenobiotic reductases A and B from Pseudomonas putida II-B and Pseudomonas fluorescens I-C: Two flavoenzymes that eliminate nitrite from nitroglycerin.* Biochemistry, In preparation, 2005.

2. Blehert, D.S., K.L. Knoke, B.G. Fox, and G.H. Chambliss, *Regioselectivity of nitroglycerin denitration by flavoprotein nitroester reductases purified from two Pseudomonas species.* J. Bacteriol., 1997. **179**(22): p. 6912-6920.

3. Blehert, D.S., B.G. Fox, and G.H. Chambliss, *Cloning and sequence analysis of two Pseudomonas flavoprotein xenobiotic reductases.* J. Bacteriol., 1999. **181**(20): p. 6254-6263.

4. Pak, J.W., K.L. Knoke, D.R. Noguera, B.G. Fox, and G.H. Chambliss, *Transformation of 2,4,6-trinitrotoluene by purified xenobiotic reductase B from Pseudomonas fluorescens I-C.* Appl. Environ. Microbiol., 2000. **66**(11): p. 4742-4750.

5. Nisbet, E.G. and N.H. Sleep, *The habitat and nature of early life.* Nature, 2001. **409**(6823): p. 1083-1091.

6. Mojzsis, S.J., G. Arrhenius, K.D. McKeegan, T.M. Harrison, A.P. Nutman, and C.R. Friend, *Evidence for life on Earth before 3,800 million years ago.* Nature, 1996. **384**(6604): p. 55-59.

7. Falkowski, P., R.J. Scholes, E. Boyle, J. Canadell, D. Canfield, J. Elser, N. Gruber, K. Hibbard, P. Hogberg, S. Linder, F.T. Mackenzie, B. Moore, 3rd, T. Pedersen, Y. Rosenthal, S. Seitzinger, V. Smetacek, and W. Steffen, *The global carbon cycle: a test of our knowledge of earth as a system.* Science, 2000. **290**(5490): p. 291-296.

8. Nelson, K.E., C. Weinel, I.T. Paulsen, R.J. Dodson, H. Hilbert, V.A. Martins dos Santos, D.E. Fouts, S.R. Gill, M. Pop, M. Holmes, L. Brinkac, M. Beanan, R.T. DeBoy, S. Daugherty, J. Kolonay, R. Madupu, W. Nelson, O. White, J. Peterson, H. Khouri, I. Hance, P. Chris Lee, E. Holtzapple, D. Scanlan, K. Tran, A. Moazzez, T. Utterback, M. Rizzo, K. Lee, D. Kosack, D. Moestl, H. Wedler, J. Lauber, D. Stjepandic, J. Hoheisel, M. Straetz, S. Heim, C. Kiewitz, J. Eisen, K.N. Timmis, A. Dusterhoft, B. Tummler, and C.M. Fraser, *Complete genome sequence and comparative analysis of the metabolically versatile Pseudomonas putida KT2440.* Environ. Microbiol., 2002. **4**(12): p. 799-808.

9. Seffernick, J.L. and L.P. Wackett, *Rapid evolution of bacterial catabolic enzymes: a case study with atrazine chlorohydrolase.* Biochemistry, 2001. **40**(43): p. 12747-12753.

10. Sisson, G., J.Y. Jeong, A. Goodwin, L. Bryden, N. Rossler, S. Lim-Morrison, A. Raudonikiene, D.E. Berg, and P.S. Hoffman, *Metronidazole activation is mutagenic and causes DNA fragmentation in Helicobacter pylori and in Escherichia coli containing a cloned H. pylori rdxA^{+} (Nitroreductase) gene.* J. Bacteriol., 2000. **182**(18): p. 5091-5096.

11. Sisson, G., A. Goodwin, A. Raudonikiene, N.J. Hughes, A.K. Mukhopadhyay, D.E. Berg, and P.S. Hoffman, *Enzymes associated with reductive activation and action of nitazoxanide, nitrofurans, and metronidazole in Helicobacter pylori.* Antimicrob. Agents Chemother., 2002. **46**(7): p. 2116-2123.

12. Trinh, S. and G. Reysset, *Mutagenic action of 5-nitroimidazoles: in vivo induction of GC-->CG transversion in two Bacteroides fragilis reporter genes.* Mutat. Res., 1998. **398**(1-2): p. 55-65.

13. Fox, K.M. and P.A. Karplus, *Old yellow enzyme at 2 Å resolution: overall structure, ligand binding, and comparison with related flavoproteins.* Structure, 1994. **2**(11): p. 1089-1105.

14. Karplus, P.A., K.M. Fox, and V. Massey, *Flavoprotein structure and mechanism. 8. Structure-function relations for old yellow enzyme.* FASEB J., 1995. **9**(15): p. 1518-1526.

15. Barna, T.M., H. Khan, N.C. Bruce, I. Barsukov, N.S. Scrutton, and P.C. Moody, *Crystal structure of pentaerythritol tetranitrate reductase: "flipped" binding geometries for steroid substrates in different redox states of the enzyme.* J. Mol. Biol., 2001. **310**(2): p. 433-447.

16. Barna, T., H.L. Messiha, C. Petosa, N.C. Bruce, N.S. Scrutton, and P.C. Moody, *Crystal structure of bacterial morphinone reductase and properties of the C191A mutant enzyme.* J. Biol. Chem., 2002. **277**(34): p. 30976-30983.

17. Breithaupt, C., J. Strassner, U. Breitinger, R. Huber, P. Macheroux, A. Schaller, and T. Clausen, *X-ray structure of 12-oxophytodienoate reductase 1 provides structural insight into substrate binding and specificity within the family of OYE.* Structure (Camb), 2001. **9**(5): p. 419-429.

18. Malone, T.E., S.E. Madson, R.L. Wrobel, W.B. Jeon, N.S. Rosenberg, K.A. Johnson, C.A. Bingman, D.W. Smith, G.N. Phillips, Jr., J.L. Markley, and B.G. Fox, *X-ray structure of Arabidopsis At2g06050, 12-oxophytodienoate reductase isoform 3.* Proteins, 2005. **58**(1): p. 243-245.

19. Hubbard, P.A., X. Liang, H. Schulz, and J.J. Kim, *The crystal structure and reaction mechanism of Escherichia coli 2,4-dienoyl-CoA reductase.* J. Biol. Chem., 2003. **278**(39): p. 37553-37560.

20. Barber, M.J. and P.J. Neame, *Correlation of X-ray deduced and experimental amino acid sequences of trimethylamine dehydrogenase.* J. Biol. Chem., 1992. **267**(10): p. 6611-6619.

21. Studts, J.M. and B.G. Fox, *Application of fed-batch fermentation to the preparation of isotopically labeled or selenomethionyl-labeled proteins.* Protein Expr. Purif., 1999. **16**(1): p. 109-119.

22. Orville, A.M., L. Manning, D.S. Blehert, J.M. Studts, B.G. Fox, and G.H. Chambliss, *Crystallization and preliminary analysis of xenobiotic reductase A and ligand complexes from Pseudomonas putida II-B.* Acta Cryst., 2004. **D60**(Pt 5): p. 957-961.

23. Collaborative Computational Project, N., *The CCP4 Suite: Programs for Protein Crystallography.* Acta Cryst., 1994. **D50**(5): p. 760-763.

24. Jones, T.A. and M. Kjeldgaard, *Electron-density map interpretation.* Methods Enzymol., 1997. **277**: p. 173-208.

25. Brünger, A.T., P.D. Adams, G.M. Clore, W.L. DeLano, P. Gros, R.W. Grosse-Kunstleve, J.S. Jiang, J. Kuszewski, M. Nilges, N.S. Pannu, R.J. Read, L.M. Rice, T. Simonson, and G.L. Warren, *Crystallography & NMR system: A new software suite for macromolecular structure determination.* Acta Cryst., 1998. **D54**(Pt 5): p. 905-921.

26. Murshudov, G.N., A.A. Vagin, A. Lebedev, K.S. Wilson, and E.J. Dodson, *Efficient anisotropic refinement of macromolecular structures using FFT.* Acta Cryst., 1999. **D55**: p. 247-255.

27. Pannu, N.S., G.N. Murshudov, E.J. Dodson, and R.J. Read, *Incorporation of prior phase information strengthens maximum-likelihood structure refinement.* Acta Cryst., 1998. **D54**(2): p. 1285-1294.

28. Read, R.J., *Model phases: Probabilities and bias.* Methods Enzymol., 1997. **277**(Pt B): p. 110-128.

29. Vaguine, A.A., J. Richelle, and S.J. Wodak, *SFCHECK: a unified set of procedure for evaluating the quality of macromolecular structure-factor data and their agreement with atomic model.* Acta Cryst., 1999. **D 55**(Pt 1): p. 191-205.

30. Laskowski, R.A., M.W. MacArthur, D.S. Moss, and J.M. Thornton, *Computer Programs.* J. Appl. Cryst., 1993. **26**(2): p. 283-291.

31. Kabsch, W. and C. Sander, *Dictionary of protein secondary structure: Pattern recognition of hydrogen-bonded and geometrical features.* Biopolymers, 1983. **22**(12): p. 2577-2637.

32. Guex, N. and M.C. Peitsch, *SWISS-MODEL and the Swiss-PdbViewer: An environment for comparative protein modeling.* Electrophoresis, 1997. **18**(15): p. 2714-2723.

33. Potterton, L., S. McNicholas, E. Krissinel, J. Gruber, K. Cowtan, P. Emsley, G.N. Murshudov, S. Cohen, A. Perrakis, and M. Noble, *Developments in the CCP4 molecular-graphics project.* Acta Cryst., 2004. **D60**(Pt 12 Pt 1): p. 2288-2294.

34. Potterton, E., S. McNicholas, E. Krissinel, K. Cowtan, and M. Noble, *The CCP4 molecular-graphics project.* Acta Cryst., 2002. **D58**(Pt 11): p. 1955-1957.

35. Khan, H., T. Barna, R.J. Harris, N.C. Bruce, I. Barsukov, A.W. Munro, P.C. Moody, and N.S. Scrutton, *Atomic resolution structures and solution behavior of enzyme-substrate complexes of Enterobacter cloacae PB2 pentaerythritol tetranitrate reductase. Multiple conformational states and implications for the mechanism of nitroaromatic explosive degradation.* J. Biol. Chem., 2004. **279**(29): p. 30563-30572.

36. Khan, H., R.J. Harris, T. Barna, D.H. Craig, N.C. Bruce, A.W. Munro, P.C. Moody, and N.S. Scrutton, *Kinetic and structural basis of reactivity of pentaerythritol tetranitrate reductase with NADPH, 2-cyclohexenone, nitroesters, and nitroaromatic explosives.* J. Biol. Chem., 2002. **277**(24): p. 21906-21912.

37. Metropolis, N., A.W. Rosenbluth, M.N. Rosenbluth, A.H. Teller, and E. Teller, *Equation of State Calculations by Fast Computing Machines.* J. Chem. Phys., 1953. **21**(6): p. 1087-1092.

38. Dauber-Osguthorpe, P., V.A. Roberts, D.J. Osguthorpe, J. Wolff, M. Genest, and A.T. Hagler, *Structure and energetics of ligand binding to proteins: Escherichia coli dihydrofolate reductase-trimethoprim, a drug-receptor system.* Proteins, 1988. **4**(1): p. 31-47.

39. Ding, H.Q., N. Karasawa, and W.A. Goddard III, *Atomic level simulations on a million particles: The cell multipole method for Coulomb and London nonbond interactions.* J. Chem. Phys., 1992. **97**(6): p. 4309-4315.

40. Ghisla, S., V. Massey, J.M. Lhoste, and S.G. Mayhew, *Fluorescence and optical characteristics of reduced flavines and flavoproteins.* Biochemistry, 1974. **13**(3): p. 589-597.

41. Kitzing, K., T.B. Fitzpatrick, C. Wilken, J. Sawa, G.P. Bourenkov, P. Macheroux, and T. Clausen, *The 1.3 Å crystal structure of the flavoprotein YqjM reveals a novel class of Old Yellow Enzymes.* J. Biol. Chem., 2005. **280**(30): p. 27904-27913.

42. Poole, L.B., *Bacterial defenses against oxidants: mechanistic features of cysteine-based peroxidases and their flavoprotein reductases.* Arch. Biochem. Biophys., 2005. **433**(1): p. 240-254.

43. Nathan, C. and M.U. Shiloh, *Reactive oxygen and nitrogen intermediates in the relationship between mammalian hosts and microbial pathogens.* Proc. Natl. Acad. Sci. U S A, 2000. **97**(16): p. 8841-8848.

44. Hensley, K., K.A. Robinson, S.P. Gabbita, S. Salsman, and R.A. Floyd, *Reactive oxygen species, cell signaling, and cell injury.* Free Radic. Biol. Med., 2000. **28**(10): p. 1456-1462.

45. Brennan, M.L. and S.L. Hazen, *Amino acid and protein oxidation in cardiovascular disease.* Amino Acids, 2003. **25**((3-4)): p. 365-374.

46. Carballal, S., R. Radi, M.C. Kirk, S. Barnes, B.A. Freeman, and B. Alvarez, *Sulfenic acid formation in human serum albumin by hydrogen peroxide and peroxynitrite.* Biochemistry, 2003. **42**(33): p. 9906-9914.

47. Poole, L.B., P.A. Karplus, and A. Claiborne, *Protein sulfenic acids in redox signaling.* Annu. Rev. Pharmacol. Toxicol., 2004. **44**: p. 325-347.

48. Claiborne, A., J.I. Yeh, T.C. Mallett, J. Luba, E.J.r. Crane, V. Charrier, and D. Parsonage, *Protein-sulfenic acids: diverse roles for an unlikely player in enzyme catalysis and redox regulation.* Biochemistry, 1999. **38**(47): p. 15407-15416.

Vita

Linda Manning was born on October 23rd, 1975 in Emmen, the Netherlands, where she attended the '*Katholiek Drents College, KDC'* (Atheneum) and graduated in June 1994 after successfully passing the final examinations in seven subjects (eindexamen), Dutch, French, English, Mathematics, Physics, Chemistry and Biology. From there, she enrolled at the '*Rijksuniversiteit Groningen, RUG*' (University of Groningen, the Netherlands) where she attended the '*Faculteit der Wiskunde en Natuurwetenschappen*' (Faculty of Mathematics and Sciences, Department of Chemistry). She graduated in March 2000 with a Master of Science degree in Biophysical Chemistry after successfully defending her thesis titled *'NMR Study of HPr in a Magnetically Ordered Liquid-Crystalline Medium'*. Linda pursued her graduate studies in the School of Chemistry and Biochemistry at Georgia Institute of Technology in Atlanta, Georgia, USA in the research group of Dr Allen Orville.